NEAR INFRARED VIEW OF STELLAR SURFACES AND CIRCUMSTELLAR DISKS WITH AN UPGRADED OPTICAL INTERFEROMETER

by

Xiao Che

A dissertation submitted in partial fulfillment
of the requirements for the degree of
Doctor of Philosophy
(Astronomy and Astrophysics)
in The University of Michigan
2014

Doctoral Committee:

Professor John D. Monnier, Chair
Professor Nuria P. Calvet
Professor Emeritus Charles R. Cowley
Professor Lennard A. Fisk
Professor Mario L. Mateo

To my parents and wife

ACKNOWLEDGEMENTS

Accomplishing this doctoral thesis has been one of the most challenging tasks I have ever faced. I am lucky to have many nice people around to help and support me, and make the doctoral life more enjoyable. To them I owe my deepest appreciation.

The thesis would not have been possible without the mentoring and guidance from my supervisor John Monnier, who has continuously inspired me with his wide range of knowledge and brainstorming ideas in science and technology. I want to thank him for supporting and encouraging me when the projects do not go well, and helping me overcome the problems. He is full of responsibility and always available to reply to my questions even on weekends. He is not only a great mentor but also a good friend. We talk about a lot of things in both academic and other fields, and he is patient to share his opinions and explain to me things I am not familiar.

I would also like to thank other thesis committee members Nuria Calvet, Charles Cowley, Lennard Fisk, and Mario Mateo for their time and attention during their busy schedule. Their critical suggestions and valuable inputs have greatly improved the quality of the thesis work. And their encouragement has given me the confidence to continue pursuing the doctoral degree.

I am most grateful to the CHARA team, especially Theo ten Brummelaar, Laszlo Sturmann, Judit Sturmann for helping me on some of the projects. Theo has provided a solid and reliable software environment for me to build my projects, and I have also learned a lot from him about how to write software. Laszlo and Judit have assisted in mechanical design, optics alignment, and providing on-site technical support.

I have had a beneficial half-year experience at Caltech thanks to Rafael Millan-Gabet who has not only strongly supported my fellowship applications, but also kindly shared the valuable KIN data with me. I also greatly appreciate his arrangement of

the trip to JPL which was really hard to arrange.

I want to express my gratitude to the graduate students in the department. I am grateful to Ming Zhao for sharing his opinions on the academic researches. He has been a great friend and we chat about a lot of things. I also want to thank my officemates Sander van Wassenhove and Matthew Miller for the patience to explain to me American culture and other foreign things I am not familiar with. I have enjoyed playing basketball with Joel Lamb, Alexander Muratov, Michael Anderson, and Zhaohuan Zhu.

I would like to thank other collaborators Fabien Baron, Stefan Kraus and Ettore Pedretti for their generosity, friendship and support. I have learned a lot from their expertise, which has speeded up the progress of the thesis.

Lastly, I thank my wife Zhichao Sun for the sacrifice of giving up her life at PSU and moving over to Michigan with me. She has been supportive of every decision I have made. Being a PhD candidate as well, she knows how to add joyful ingredients to make the PhD life less stressful. I have enjoyed every trip with her company, birthday presents made by her hands and tasty food she cooked from which I have gained 15 pounds.

CONTENTS

CHAPTER

LIST OF FIGURES

LIST OF TABLES

LIST OF APPENDICES

ABSTRACT

Interferometry has the advantage of overcoming the diffraction limit of individual telescopes and achieving higher angular resolution. Modern long baseline optical interferometers can reach sub-milliarcsecond angular resolution, allowing us to resolve nearby stellar systems to reveal the detailed structures of stellar surfaces as well as circumstellar disks. This thesis work includes a scientific study of two rapidly rotating stars, a Be star observed in H band by an optical interferometer (CHARA/MIRC), and instrumental developments on the interferometer.

A solid body rotation model fitting the interferometric data of the two rapid rotators β Cas and α Leo reveals close-to-breakup rotations in both cases, which result in oblate geometry of the photospheres. Consequently, the equatorial temperatures are much lower than the polar temperatures due to the gravity darkening effect. Model-independent photospheric images are constructed, confirming the geometry and temperature distribution from the model fitting. A rotational correction is proposed to more accurately estimate stellar ages and masses of rapid rotators on the traditional HR diagram. The correction takes into account the non-uniform temperature distribution and the oblate geometry, which can only be obtained through optical interferometry. The preferred non-standard gravity darkening coefficients of rapid rotators from this work agrees with previous studies, suggesting a breakdown of von Zeipel's law. One possible explanation is that the temperature and pressure difference across latitudes caused by the rotation induces meridional flow, which violates the radiative envelope assumption.

Spectroscopic and photometric observations of the high-eccentricity Be binary system δ Sco during the periastron in 2000 indicated that the secondary passage triggered the gaseous disk formation around the primary star. Our 7 nights of inter-

ferometric observations of the system right after its periastron in 2011 resolved the binary as well as the circumstellar disk around the primary. The modeling and imaging results showed a mainly symmetric disk with stable and consistent H band flux contributions from the primary disk over the 7 nights. This result suggests no significant material outflow from the primary star due to the gravitational interference from the secondary star, contrary to the results from the periastron in 2000.

In order to improve the scientific results from MIRC and the sensitivity of the CHARA array, I have participated in three instrumental projects. In the first project, I have developed the subsystem Photometric Channels for MIRC to directly measure the fluxes of the individual beams in real time to improve the calibration of the interferometric data. The Photometric Channels have not only reduced the uncertainty of the visibility measurements from 10% to 3%, but also increased the observational efficiency. In the second project, I have upgraded MIRC from a 4-beam combiner to a 6-beam combiner to exploit the full usage of the CHARA 6 telescopes. The upgrade obtains 2.5 times more of visibility measurements and recovers ~ 3 times more of phase information in a single snapshot, allowing imaging and modeling of more complex stellar systems such as circumstellar disks and spotted stars. In the third project, I have developed the Wavefront Sensor (WFS) for the CHARA Adaptive Optics upgrade. The WFS commissioning run in January 2014 has shown an improvement of sensitivity of 4 magnitudes in R band, allowing 5 times more Young Stellar Objects (YSOs) in Taurus to be observable with the CHARA array, as well as a few brightest Active Galactic Nuclei (AGN) and microquasars.

CHAPTER 1

Introduction

1.1 Principles of Optical Interferometry

1.1.1 Why Interferometry

Interferometry is a technique to combine multiple coherent electromagnetic waves, i.e. photons, and has wide applications in many different fields. In astronomy, the main benefit of interferometry is providing high angular resolution. The angular resolution of two telescopes separated by a baseline of B is equivalent to that of a single telescope with the diameter of B, but the former approach has much lower cost and is more practical. Therefore interferometry is the only method of access to high angular resolution when a single large telescope is not available.

To understand the physics behind interferometry, let's consider telescopes in one dimension, as represented by slits in Figure 1.1. For simplification, we assume the incoming beam is plane-parallel and monochromatic, and the telescopes are free of any optical aberrations. Photons can behave as a particle or wave, but it is the latter that leads to important phenomena such as diffraction and interference. The wave propagation can be described by Huygens Principle where every point on the wavefront becomes a source of spherical wave, and the sum of these secondary waves determines whether it is construction or destruction in every direction.

In the case of diffraction as shown in the left panel of Figure 1.1, the light can only go through the slit. The output electric field amplitude and intensity distributions can be computed as a function of θ:
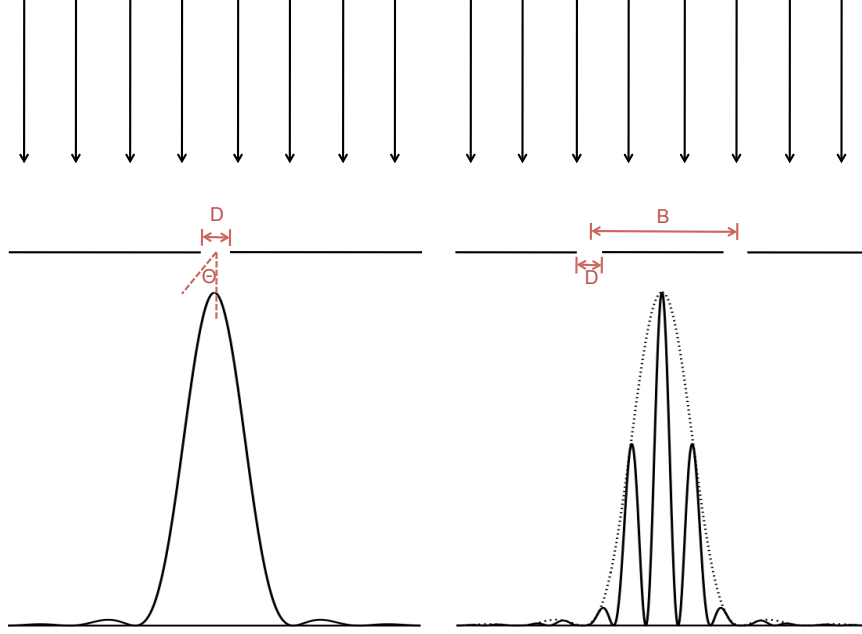
Figure 1.1. The left panel shows the intensity distribution of a diffraction pattern with one slit, and the right panel shows that of an interference pattern with two slits. The incoming light is assumed to be plane-parallel and monochromatic.

$$
\begin{aligned}
A_s(\theta) &= \int_{-D/2}^{D/2} A \exp(2\pi i x \sin\theta/\lambda) dx/D \\
&\approx \int_{-D/2}^{D/2} A \exp(2\pi i x \theta/\lambda) dx/D \\
&= A\frac{\lambda}{2\pi i \theta D}[\exp(\pi i \theta D/\lambda) - \exp(-\pi i \theta D/\lambda)] \\
&= A\frac{\sin(\pi\theta D/\lambda)}{\pi\theta D/\lambda} \\
I_s(\theta) &= A_s^2(\theta) \\
&= A^2[\frac{\sin(\pi\theta D/\lambda)}{\pi\theta D/\lambda}]^2,
\end{aligned}
\tag{1.1}
$$

where A is the amplitude of the electric field, D is the width of the slit, θ is the output direction as shown in the left panel of Figure 1.1, λ is the wavelength of the beam. Equation 1.1 is the mathematic description of diffraction where the peak and null intensity alternates, producing multiple lobes with the strongest one in the middle, and weaker ones along both sides as moving away from the middle. In two dimension space, the pattern is an Airy disk which is an analogue of images of unresolved objects

observed by a single-dish telescope under ideal conditions. The location of the first null determines the angular resolution, which in the one dimension case is

$$\theta_s = \frac{\lambda}{D}. \tag{1.2}$$

If we modify the experiment by replacing one slit with two identical slits close to each other, then the beams through the two slits will interfere with each other and produce another pattern called fringes (right panel of Figure 1.1). Using Huygens Principle again, the output electric field amplitude and intensity distributions are:

$$
\begin{aligned}
A_b(\theta) &\approx \int_{-B/2-D/2}^{-B/2+D/2} A \exp(2\pi i x \theta/\lambda) dx/D + \int_{B/2-D/2}^{B/2+D/2} A \exp(2\pi i x \theta/\lambda) dx/D \\
&= 2A \frac{\sin(\pi\theta D/\lambda)}{\pi\theta D/\lambda} \cos(\pi\theta B/\lambda) \\
&= 2A_s(\theta) \cos(\pi\theta B/\lambda), \\
I_b(\theta) &= A_b^2(\theta) \\
&= 4A_s^2(\theta) \cos^2(\pi\theta B/\lambda) \tag{1.3} \\
&= 2A_s^2(\theta)[1 + \cos(2\pi\theta B/\lambda)], \tag{1.4}
\end{aligned}
$$

where B is the baseline or distance between the two slits. The graphic result of Equation 1.4 is presented in the right panel of Figure 1.1. It could be understood as a cosine wave whose amplitudes is modulated by the diffraction pattern from either of the slit. Again the angular resolution is determined by the first null of the fringe, which is

$$\theta_b = \lambda/2B. \tag{1.5}$$

This two slit experiment is well known as Young's doublet-slit experiment, it is an analogue to two-element interferometer and demonstrates the basic principle of the interferometry. Comparison between the Equation 1.2 and 1.5 illustrates the angular resolution of an interferometer could be much higher than that of a single telescope

when the baselines of an interferometer are much larger than the telescope diameter. Modern optical interferometers have baselines from several tens to a few hundreds of meters, which provide angular resolutions one to two orders of magnitudes higher than typical optical telescopes.

1.1.2 Interferometric Measurements

Interferometry produces fringe patterns which can be characterized by their phases and contrasts. A commonly used quantity that is related to the fringe contrast is Michelson fringe visibility defined as

$$\nu = \frac{I_{max} - I_{min}}{I_{max} + I_{min}}, \tag{1.6}$$

where I_{max} and I_{min} are the maximum and minimum of the fringe intensity. Therefore the visibility ν is an dimensionless quantity in the range from 0 to 1. The phase and visibility are related to the properties of the objects, which are demonstrated in two simple cases based on the Young's doublet-slit experiment. To simplify the discussion, I ignore the diffraction effect from either of the slits.

The fringe phase can be understood as the phase offset relative to some reference position. In the case of Figure 1.2(a) where a point source is observed on axis, the fringe position is marked as reference position. If the source is observed off axis as in the Figure 1.2(b), the fringes are shifted by ϕ relative to the reference position. Therefore the fringe phase information is related to object's symmetry relative to the axis of the telescope pointing.

In the case of an unresolved object as in Figure 1.2(a) where $I_{min} = 0$, the fringe visibility $\nu = 1$. But for a resolved object as in Figure 1.2(c), ν is some value between 0 and 1. This is because a resolved object can be decomposed into many unresolved small components, and each component produces fringes with $\nu = 1$. These components have different angular offsets relative to the axis of the telescopes, and thus individual fringes are not perfectly overlapped, as shown by the orange lines in Figure 1.2(c). Therefore the sum of the fringes (black line in Figure 1.2(c)) becomes less sharp. Figure 1.3 shows visibility curves of some typical geometries.

4
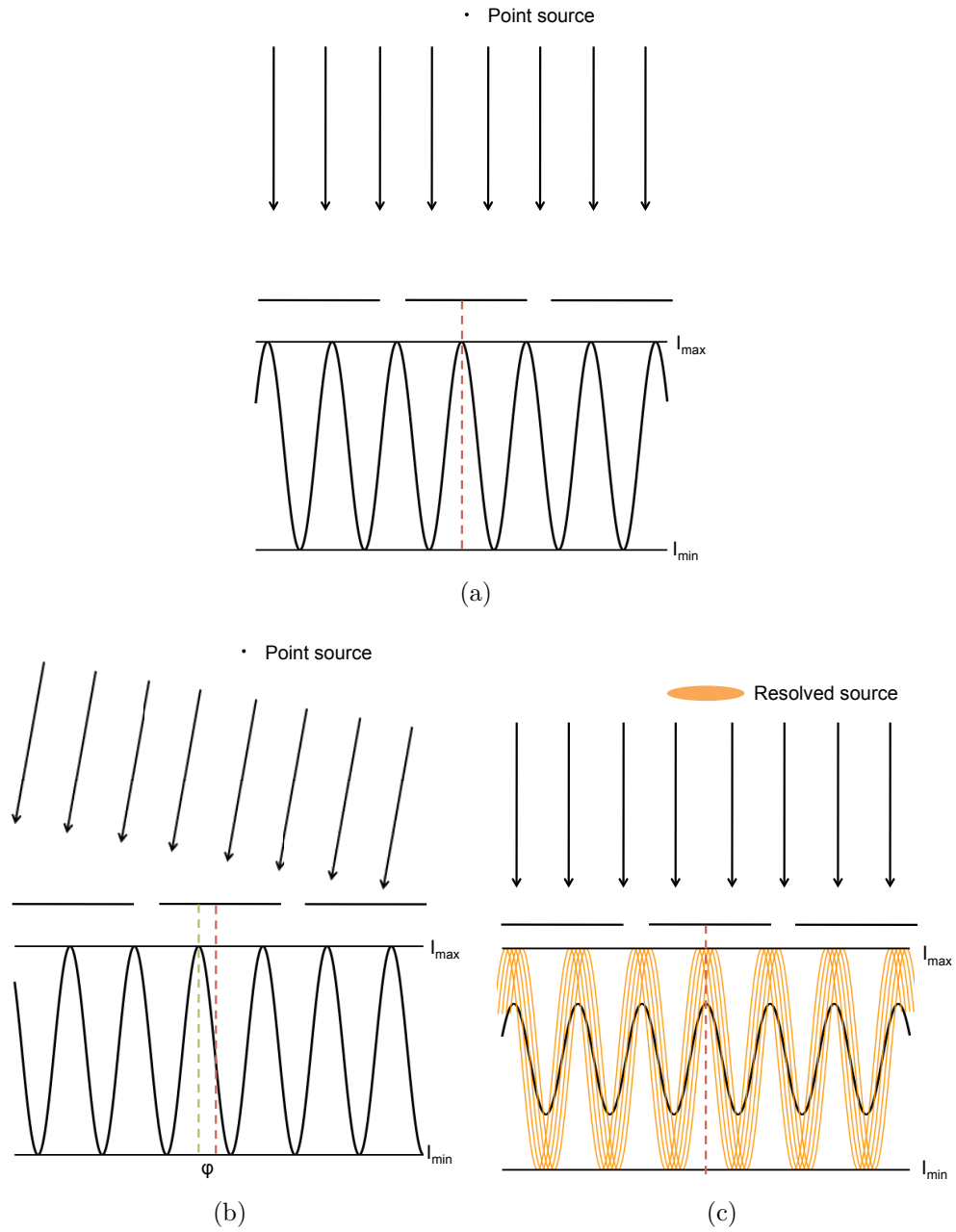
Figure 1.2. Visibility and phase of interferometric data
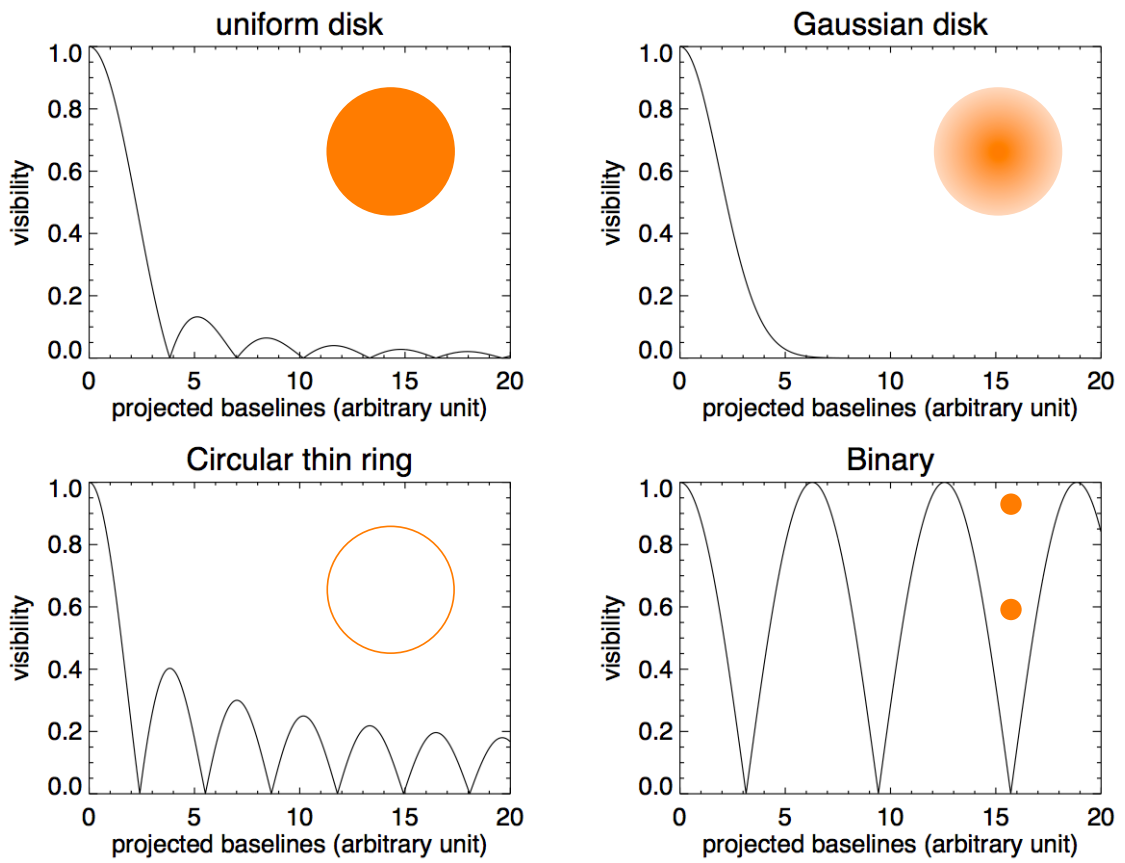
Figure 1.3. Here are a few examples of visibility curves of some typical geometries.

A visibility and phase form a complex visibility:

$$\tilde{V} = \nu e^{i\phi}. \tag{1.7}$$

The famous van Cittert-Zernike theorem (developed by van Cittert and Zernike) connects complex visibilities with the image of an object:

$$
\begin{aligned}
u &= \frac{B_x}{\lambda} \\
v &= \frac{B_y}{\lambda} \\
\tilde{V}(u,v) &= \int d\alpha d\beta F(\alpha,\beta) e^{-2\pi i(u\alpha+v\beta)}
\end{aligned}
\tag{1.8}
$$

where B_x and B_y are the projected baselines in x and y direction, λ is the observation wavelength, α and β are angular offsets relative to the optical axis of the telescopes in the x and y direction, and $F(\alpha,\beta)$ is the normalized intensity distribution of the target. The detailed derivation of Equation 1.8 can be found in e.g. Thompson et al. (2001).

Equation 1.8 shows that the complex visibility can be interpreted as the Fourier transform of the target's intensity distribution, and an interferometer samples the Fourier space (also called (u,v) space) as shown in Figure 1.4. The baseline of a pair of telescopes is projected to the (u,v) space and forms a vector from the origin. The telescope pair measures the complex visibility where the vector points. For instance, the three baselines formed by the three telescopes in 1.4 measures three corresponding complex visibilities in the (u,v) space.

In reality the complex visibilities are seriously affected by the atmospheric turbulence. Fortunately the power spectrum of the fringes $|\tilde{V}^2|$ is still recoverable. By measuring the interferogram power spectrum of a nearby unresolved star, the atmospheric effects on $|\tilde{V}^2|$ can be estimated, and then applied to the science targets.

However the phase information is contaminated by the atmospheric differential piston (zeroth order of atmospheric aberrations) and not recoverable. The effects of
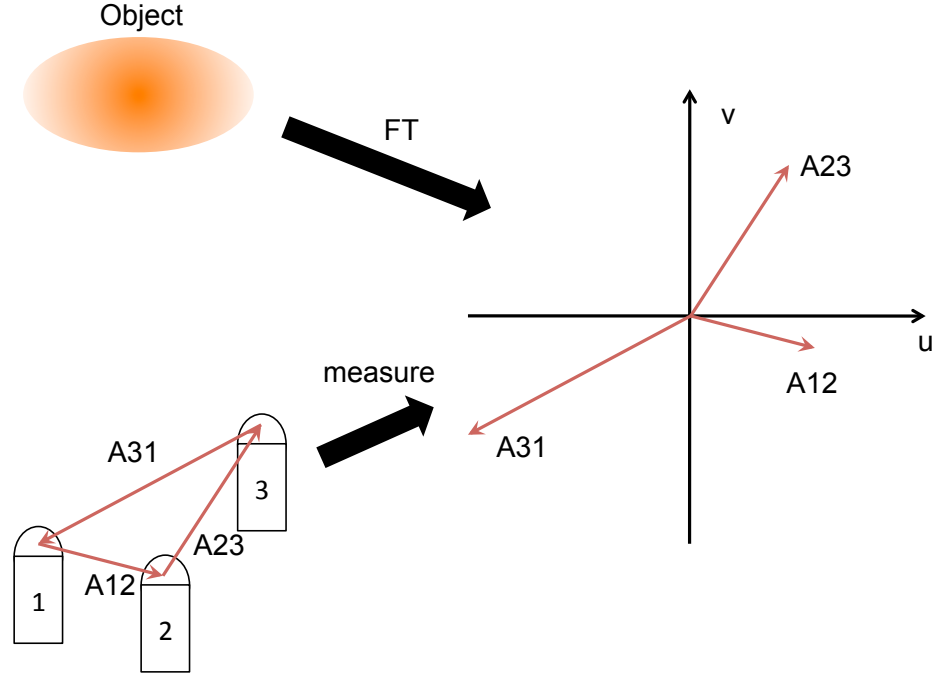
Figure 1.4. An interferometer measures the complex visibilities of an image in Fourier space

pistons on interferogram phases can be understood as adding extra phase delays to two beams. For example, suppose the atmosphere adds ϕ_1 and ϕ_2 phase delays to the beams received by telescope 1 and 2 as shown in Figure 1.5, then the measured fringe phase between these two telescopes is

$$\Phi_{12}^{measured} = \Phi_{12}^{intrinsic} + \phi_2 - \phi_1. \tag{1.9}$$

Since neither ϕ_1 nor ϕ_2 is known and both vary with time, it is impossible to calculate $\Phi^{intrinsic}$.

However the phase information can be partially retrieved by using three telescopes (Figure 1.5). Assume there is a third telescope in the telescope array, two more similar equations as Equation 1.9 can be listed for telescope pair 2 and 3, 3 and 1,

$$\Phi_{23}^{measured} = \Phi_{23}^{intrinsic} + \phi_3 - \phi_2, \tag{1.10}$$

$$\Phi_{31}^{measured} = \Phi_{31}^{intrinsic} + \phi_1 - \phi_3. \tag{1.11}$$
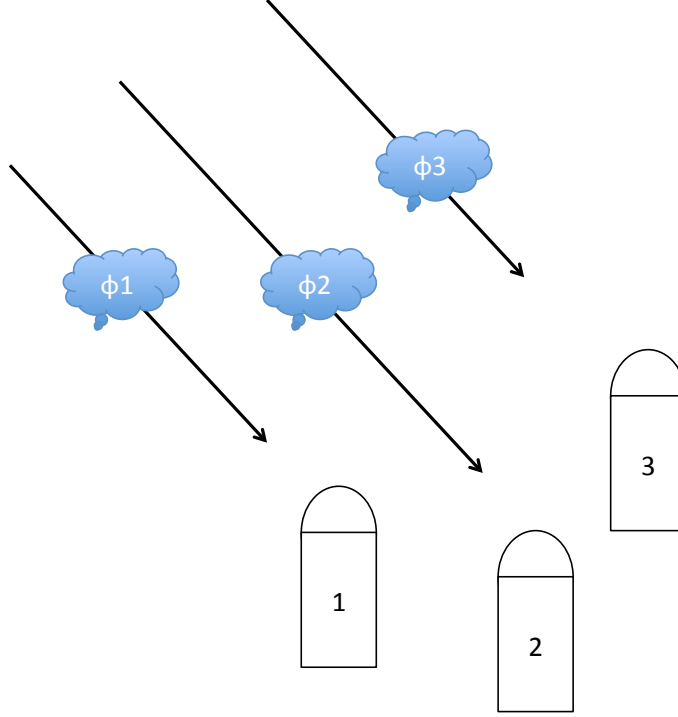
Figure 1.5. An example of closure phase

By adding Equations 1.9, 1.11 and 1.11 together, the atmospheric phase delay cancels out and the resulting equation becomes

$$\Phi_{12}^{measured} + \Phi_{23}^{measured} + \Phi_{31}^{measured} = \Phi_{12}^{intrinsic} + \Phi_{23}^{intrinsic} + \Phi_{31}^{intrinsic}. \qquad (1.12)$$

Therefore the sum of the three phases $\Phi_{12} + \Phi_{23} + \Phi_{31}$ is immune to atmospheric pistons. This term is known as closure phases (Jennison, 1958).

Closure phase is equivalent to the phase part of a bispectrum (Lohmann et al., 1983), which is defined as:

$$\begin{aligned}
B_{123} &= \tilde{V}_{12}\tilde{V}_{23}\tilde{V}_{31} \\
&= \nu_{12}\nu_{23}\nu_{31} \exp[i(\Phi_{12} + \Phi_{23} + \Phi_{31})], \qquad (1.13)
\end{aligned}$$

where the amplitude part is called triple amplitude. Weigelt (1977) independently developed algorithms to reconstruct images using a bispectrum.

For more telescopes (N>3), closure amplitudes can be formed by:

$$A_{1234} = \frac{\nu_{12}\nu_{34}}{\nu_{13}\nu_{24}}. \tag{1.14}$$

This quantity can be formed in different ways by alternating the subscripts. The advantage of this quantity is that it is independent of the telescope-specific gain amplitudes.

1.2 Major Science with Optical Interferometers

The longest baseline of the currently operating optical interferometers is a few hundred meters, offering sub-milliarcsecond (mas) angular resolution which is two orders of magnitude higher than that of the Hubble Space Telescope. Such high angular resolution is able to resolve detailed structures of astronomical objects such as stellar surfaces, which could not be obtained by other methods.

However optical interferometry also suffers small field of view and low sensitivity, which limits its major targets to the nearby stellar systems. With larger telescope apertures and the aid of Adaptive Optics systems, some interferometers are/will be able to observe a few extragalactive sources. In this section, I will give an overview of scientific contributions from the optical interferometry to nearby stellar systems.

1.2.1 Stellar Diameters

It is not surprising that one of the main contributions from optical interferometers is to measure stellar diameters. This is especially true for early generations of optical interferometers which only consisted of two telescopes, providing one visibility measurement at a time and no phase information. Such limited measurements prevent scientists from studying complicated stellar physics. On the other side, even the close-by supergiants are as small as tens of mas in diameter, and the main sequence ones are only about a few mas or less. Such small angular sizes are beyond the angular resolution of a single telescope, and makes optical interferometry the only and

ideal technique to make contributions.

Assuming a star can be approximated as a circular uniform disk, one visibility measurement is sufficient in principle to determine its angular size θ_R. Modern optical interferometers are able to provide measurements from several baselines with different projections, thus constraining stellar angular sizes at different orientations (Monnier et al., 2007). Several catalogues of stellar angular sizes have been complied with measurements from optical interferometers (e.g. Mozurkewich et al., 2003; Berger et al., 2006; van Belle & von Braun, 2009; Boyajian et al., 2012). However angular sizes of most stars are still unknown either because they have not been observed by an optical interferometer or they are not resolved even with the longest baseline available. Several groups (e.g. Kervella et al., 2004c; Kervella & Fouqué, 2008) have developed the surface brightness-color relations to predict stellar angular size. The relations have been calibrated by the existing long-baseline optical interferometric observations of nearby stars (e.g. Figure 1.6 from Kervella & Fouqué, 2008). These relations as well as the catalogues are important to optical interferometry, gravitational microlensing, extrasolar planet transits, etc.

Stellar diameter is a basic parameter, and has important applications when combined with other measurements. One of them is deriving stellar effective temperature T_{eff} , which is defined as

$$
\begin{aligned}
T_{eff} &= \left(\frac{L}{4\pi\sigma R^2}\right)^{1/4} \\
&= \left(\frac{4\pi d^2 F_{bol}}{4\pi\sigma R^2}\right)^{1/4} \\
&= \left(\frac{F_{bol}}{\sigma\theta_R^2}\right)^{1/4},
\end{aligned}
\tag{1.15}
$$

where L is the stellar luminosity, σ is the Stephan-Boltzman constant, R is the stellar radius, d is the distance, F_{bol} is the bolometric flux, and θ_R is the stellar angular radius. Therefore given θ_R from interferometric measurements and F_{bol} from photometric measurements, stellar effective temperature T_{eff} can be determined.
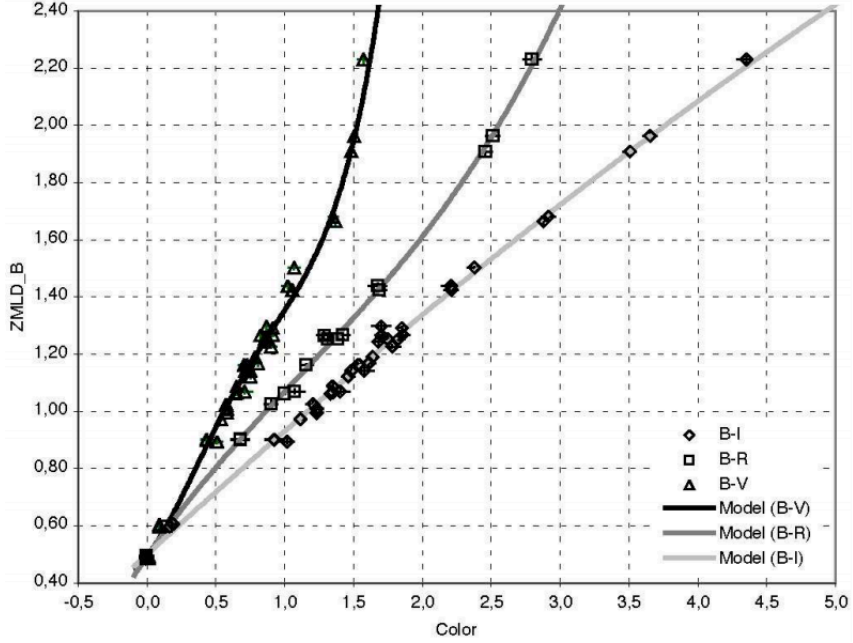
Figure 1.6. Polynomial fitting of stellar angular sizes as a function of color indexes (reprinted from Kervella & Fouqué, 2008). The y axis is the zero-magnitude limb-darkened disk angular diameter in B band.

1.2.2 Limb Darkening

The uniform disk approximation of a star is a reasonable first order approximation. However several subtle known effects can corrupt the accuracy of the estimated sizes. One of the important effects is limb darkening where a star appears to be brighter in the center than its limb. This phenomenon is related to the optical depth effects that one sees different layers of stellar atmosphere due to the different incidence angles at the center and limb of the star. Limb darkening must be correctly taken into account in order to improve the precision of the estimated stellar sizes.

A limb darkened circular disk is still point symmetric, therefore it does not show any effects on closure phases. The visibility curve of a limb darkened circular disk is very close to that of a uniform disk in the first lobe: the difference is about 0.1% which is far less than the typical uncertainties in interferometric measurements. In the second lobe, the difference is much more significant, but the visibility value is much lower. Therefore high precision long-baseline optical interferometers are required to detect and estimate the limb-darkening effects (e.g. White et al., 2013; Cruzalèbes
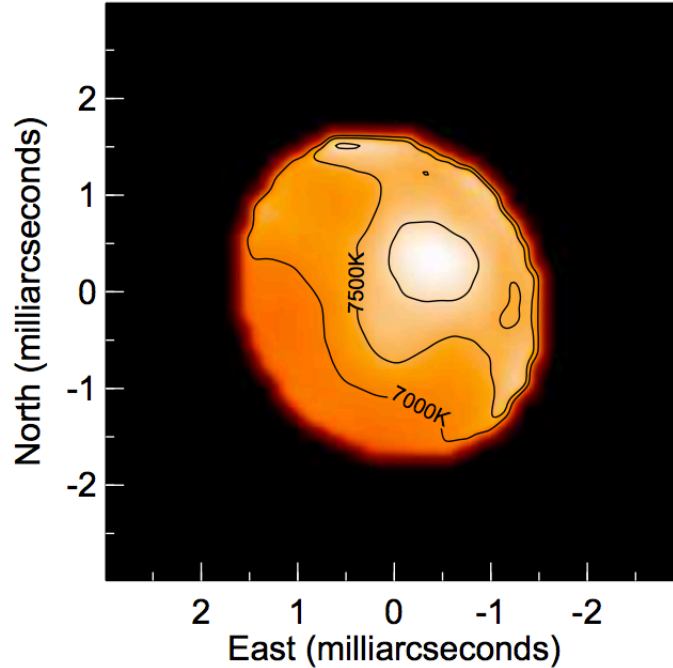
Figure 1.7. Reconstructed image of Altair observed by CHARA/MIRC on UT2006 Aug. 31st (reprinted from Monnier et al., 2007)

et al., 2013)

1.2.3 Rapidly Rotating Stars and Gravity Darkening

Unlike the Sun, a significant fraction of early spectral type stars are rapidly rotating. The rotation distorts stellar geometry: making the equatorial radius larger than the polar radius. Altair is the first main sequence star beyond the solar system that has been imaged, as shown in Figure 1.7 (Monnier et al., 2007). The image clearly shows an elongated equator as expected. Following Altair, several other rapid rotators with such geometry have been detected by interferometric observations (e.g. Domiciano de Souza et al., 2003; Zhao et al., 2009; Che et al., 2011). The angular rotation of these stars have been computed to be more than 90% of their breakup speed using a rigid rotation model (Aufdenberg et al., 2006). Such fast stellar rotation has strong effects on stellar evolution and properties.

One of the important effects is called gravity darkening: the effective temperature $T_{\rm eff}$ is related to the local effective gravity g which varies across latitudes due to stellar rotation. von Zeipel (1924a,b) first proposed that for a rapidly rotating star whose

envelope is dominated by radiation, the local effective temperature is proportional to the local effective gravity using a solid body rotation model:

$$T_{eff} \propto g^{0.25}. \tag{1.16}$$

Decades later, Lucy (1967) demonstrates a similar relation in a rapid rotator with convection-dominated envelope:

$$T_{eff} \propto g^{0.08}. \tag{1.17}$$

In general, one has $T_{eff} \propto g^{\beta}$, where $\beta = 0.25$ for a radiation-dominated envelope and $\beta = 0.08$ for a convection-dominated envelope. Since the poles have higher local effective gravity than the equator, the poles are always hotter than the equator for a rapid rotator, making the equator less luminous than the poles. This phenomena have been observed and confirmed on several rapid rotators with near infrared interferometric observations (e.g. Monnier et al., 2007; Zhao et al., 2009; Che et al., 2011), although the derived β takes non-standard values (see Section 2.8 for more details).

The variation of the brightness across the stellar surface indicates apparent luminosity and T_{eff} change as a function of the stellar inclination angle. For instance, if a rapid rotator is pole-on, then an observer sees the more luminous pole and higher effective temperature. And if the rapid rotator is edge-on, then the observer sees the less luminous equator and lower effective temperature. In either case, the true luminosity and T_{eff} are hidden from the observer. One relies on optical interferometry to resolve the stellar surface to derive the true values.

1.2.4 Stellar Spots

Just as the Sun has spots, stars have spots as well. However stellar spots could be either hotter or cooler, and they could be much larger than the solar spots in physical sizes. Interferometric studies of stellar spots started with supergiants because they are large and can be easily resolved by early generations of interferometers. However supergiants are rare compared to main sequence stars, and there are only a few close
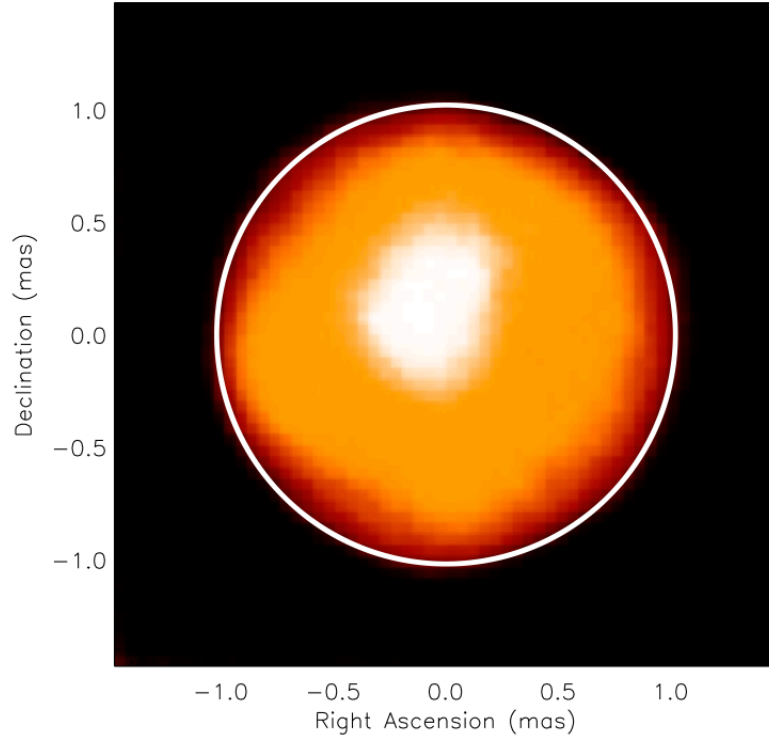
Figure 1.8. Reconstructed image of T Per observed by CHARA/MIRC (reprinted from Baron et al., 2014). The image shows a bright spot on the stellar surface. The white circle is the angular diameter of the star from model fitting.

to us.

Betelgeuse is one of the close-by supergiants that are well studied by optical interferometers. The large angular size ($\theta = 43.26\text{mas}$, Perrin et al., 2004) allows interferometers, especially single telescopes with aperture masking, to image and model its photosphere to reveal rich stellar surface features (Haubois et al., 2009). Several groups (Roddier & Roddier, 1983; Buscher et al., 1990; Young et al., 2000) have performed optical interferometric observations on Betelgeuse and shown evidence of bright spots that emit 10-20% of the flux in the visible and near-infrared.

Following Betelgeuse, many other giants and supergiants have been imaged for the last two decades and shown asymmetries on their surfaces (Tuthill et al., 1997, 1999; Ragland et al., 2006; Chiavassa et al., 2010). Such asymmetries or hot spots vary on a timescale of months, and they are more significant when observed at the shorter wavelengths. Figure 1.8 (Baron et al., 2014) shows a bright spot on the stellar surface of T Per observed by CHARA/MIRC. The image is convolved to the expected

angular resolution.

The hot spots were originally explained as the hot areas on the stellar surface caused by the upwellings of the convective envelopes (Schwarzschild, 1975). An alternative was proposed by Young et al. (2000) where a molecular blanket (e.g. TiO) covers most parts of the photosphere and leaves only a few holes due to inhomogeneities. The blanket is optically thick in the visible and thin in the infrared. Therefore visible light can escape through the holes and results in the observed hot spots.

1.2.5 Pulsating Stars: Cepheids

A large fraction of stars from main sequence to supergiants pulsate. The most important and interesting ones are the giants and supergiants with radial pulsations where the stellar brightness varies due to the expansion or compression of the stellar envelopes. The most likely mechanism that drives the pulsation is the κ mechanism where a partially ionized layer in the stellar envelope is ionized by absorbing the energy from the compression. This increases the opacity so that more radiation is trapped to produce a force of expansion. On the other hand during the expansion, the layer releases the energy from recombination, which results in lower opacity and therefore lower radiation pressure. The gravitational force overcomes the radiation pressure, and slows down the expansion and eventually starts another round of compression.

Cepheids are one kind of pulsating supergiant with periods of a few to several tens of days. They exhibit a tight correlation between the period and luminosity (P-L relation) as first discovered by Henrietta Leavitt. This important correlation now plays a crucial role in the cosmic distance ladder, and fills the gap between the stellar neighborhood and galaxies.

However, the correlation needs to be calibrated. The accuracy of the luminosity measurements depends on the accuracy of the stellar radius, which is usually estimated according to the Baade-Wesselink method. The method uses the stellar color and flux at two different times to estimate the change of stellar radii in ratio, and then use spectra through the pulsation to estimate the radial velocity of the stellar

surface, which is then integrated to compute the difference of the radii. Therefore the stellar radii at these two different times can be calculated.

The uncertainty of this method can be reduced by independent stellar angular diameter measurements from optical interferometry as discussed by Sasselov & Karovska (1994). However since Cepheids are rare and they are generally far away, the variation of the stellar radii is relatively small in the sub-mas level, which requires long-baseline optical interferometry.

Early attempts of interferometric observations of Cepheids from GI2T (Mourard et al., 1997), PTI (Lane et al., 2000), NPOI (Armstrong et al., 2001), IOTA (Kervella et al., 2001) have shown marginal detection of the pulsation. Positive detections of the pulsation have been revealed on several Cepheids (Lane et al., 2002; Kervella et al., 2004b; Davis et al., 2009) with improved signal-to-noise ratio . An example of angular size variation of δ Cepheid is shown in Figure 1.9 (Mérand et al., 2005). These measurements are used to calibrate and improve the precision of the P-L relation of Cepheids (Kervella et al., 2004a; Fouqué et al., 2007). With higher precision, subtle effects such as limb-darkening and circumstellar disks become the dominant errors of radius estimation from optical interferometry. Much effort has been invested in modeling these effects to further improve the precision of the P-L relation (e.g. Mérand et al., 2007).

1.2.6 Binary Systems

A significant fraction of stars are in binary or multiple systems, which is an outcome of the stellar formation process out of molecular clouds. Compared to single field stars, the revolution of binary systems offers a unique opportunity to measure their masses precisely which is crucial to the stellar evolution theory (Eggen, 1967). Also the fact that stars in a binary system generally have similar ages can be used to test stellar evolution models.

There are different types of binaries based on how their orbits can be measured. For visual binaries, the separations are so wide that individual stars can be resolved by a single telescope. For spectroscopic binaries, their separations are too small to be
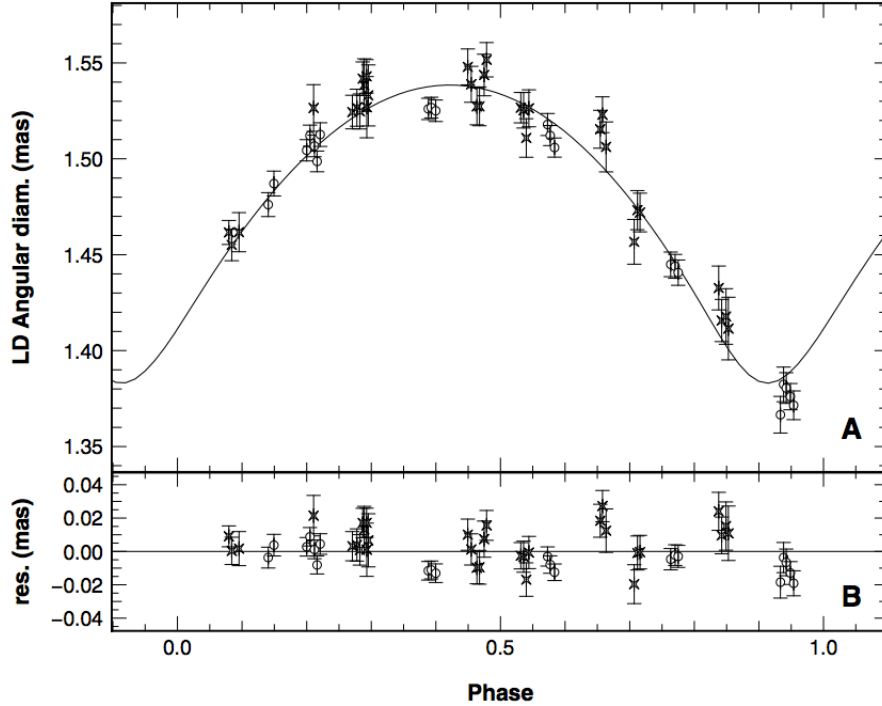
Figure 1.9. The angular sizes of δ Cepheid varies as a function of phase (reprinted from Mérand et al., 2005).

resolved by a single telescope, and the binary nature is only imprinted in the spectra due to the Doppler shifts from the revolution motion. If the binary orbit happens to be aligned with the line of sight, then part of light will be blocked when one star passes in front of the other, causing a periodic variation in photometry. Such binaries are called eclipsing binaries.

Measuring binary orbits has always been a major contribution from optical interferometry. Because of the high angular resolution, interferometers can resolve binary orbits and accurately determine astrometric binary orbits. Especially, optical interferometry can significantly improve the accuracy of orbital parameters of short period binaries, which were only observable spectroscopically due to their small separations (McAlister, 1985; Hummel et al., 1995; Hartkopf et al., 2001; Baron et al., 2012b; Mason et al., 2013). The most accurate orbit measurements can reach sub-milliarcsecond precision by modern interferometers to reach sub-1% precision of stellar parameters.

In some close binaries where one of the stars evolves to fill its Roche-Lobe and starts to lose mass to its companion, there is an opportunity to study stellar inter-
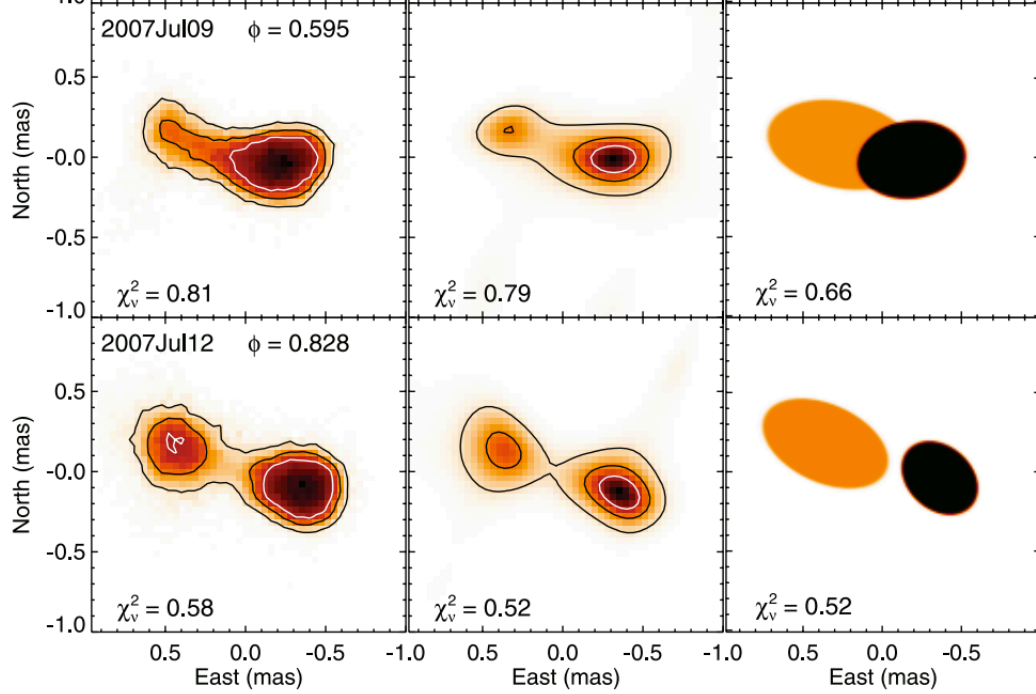
Figure 1.10. Reconstructed images of β Lyr observed by CHARA/MIRC. The left column is images reconstructed using MACIM algorithm, the middle is from BSMEM algorithm, and the right is model images (reprinted from Zhao et al., 2008).

action and mass transfer which is crucial to understand the stellar evolution in a binary system. Long-baseline optical interferometry provides a possibility to resolve and probe the active regions in between two stars (Richardson et al., 2012; Baron et al., 2012b; Chesneau et al., 2014). Figure 1.10 shows an example of reconstructed images of β Lyr at two different phases (Zhao et al., 2008).

1.2.7 Be stars

A Be star is a "non-supergiant B star whose spectrum has or had at some time one or more Balmer lines in emission" (Collins, 1987). In addition to the prominent line emission, other important observational characteristics of Be stars include infrared continuum excess and partial polarization of radiation. A general consensus to explain the emitting mechanism is free-free and free-bound emission from a thin circumstellar disk. This extended disk emission therefore can be more easily resolvable than stellar photosphere by optical interferometers. The angular sizes of the disks around Be stars in near and mid infrared have been reported using a symmetric Gaussian disk
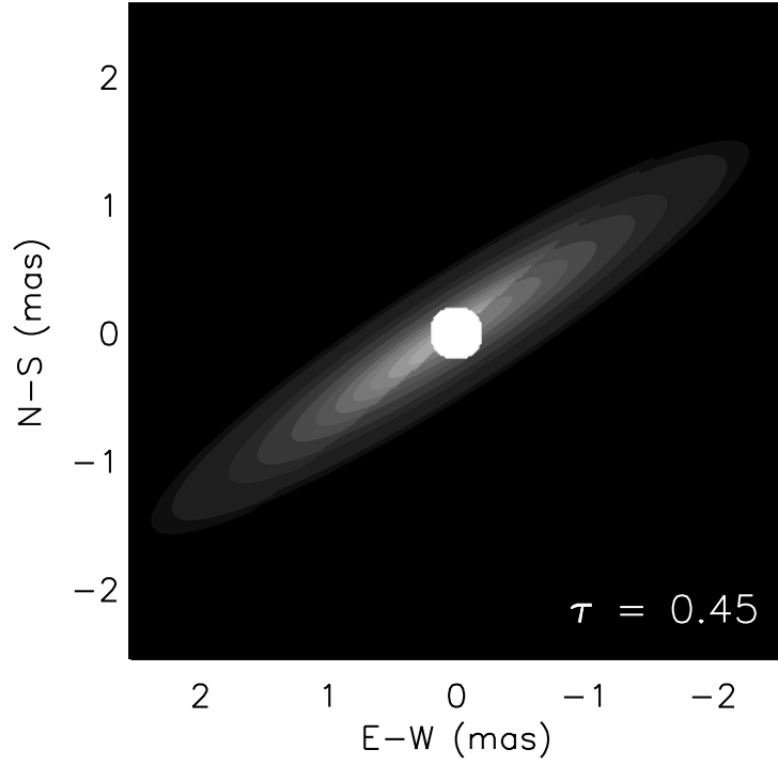
Figure 1.11. A model image of ζ Tau observed by CHARA/MIRC on Nov. 10th 2009 (reprinted from Schaefer et al., 2010).

model (Touhami et al., 2013; Meilland et al., 2009, 2012), and are about 1 - 10 times larger than the stellar radii. Figure 1.11 shows a fitted geometric model of ζ Tau (Schaefer et al., 2010).

Another distinctive phenomena of Be stars is the change of physical conditions in the disk, causing e.g. emission line profiles may vary over weeks to decades (Porter & Rivinius, 2003; Waters & Waelkens, 1998). One possible explanation for the short term variations is rotational modulation of the circumstellar disk where the disk intensity profile is uneven azimuthally (Porter & Rivinius, 2003), e.g. temperature or density enhancement at certain parts of the disk. As the enhanced region rotates, the integrated emission line profile varies. Such disk asymmetry has been found on several individual stars in both spectral lines and continuum emissions by optical interferometry (Stee et al., 1995, 1998; Vakili et al., 1998; Schaefer et al., 2010; Meilland et al., 2012).

Several mechanisms and models have been proposed to explain the formation

of the gaseous disk (Porter & Rivinius, 2003). The viscous "decretion" disk model pioneered by Lee et al. (1991) has successfully explained several key observations, and become the best candidate for explaining Be star disk formation. One key assumption in the model is that the central star is rotating rapidly. The initial velocities of Be stars are significantly higher than those of normal B stars, suggesting that fast rotation is crucial to Be phenomena (Martayan et al., 2006). In fact a recent spectro-interferometry survey of Be stars demonstrated the mean rotation rate $\Omega/\Omega_c = 0.95 \pm 0.02$ (Meilland et al., 2011). For such fast rotation, many instabilities such as non-radial pulsations could be sufficient to elevate stellar equatorial material into orbit (Townsend et al., 2004). Another key assumption in the viscous decretion model is a Keplerian rotation disk, which has also been confirmed by recent spectro-interferometry observations of α Arae (Meilland et al., 2007) and β Canis Minoris (Kraus et al., 2012b)

1.2.8 Young Stellar Objects

The dusty disks around Young Stellar Objects (YSOs) play an important role in the formation and evolution of stars as well as planetary systems. Disks transport metals, angular momentum etc. when feeding materials to central protostellar objects through accretion, and thus affect stellar initial metallicities, rotation speeds and masses. These initial properties determines the stellar evolution paths. Planets are believed to form inside the disks through a rapid process of aggregation from micron-size dust particles to kilometer-size bodies, although the detailed mechanisms are still in debate. Therefore studying the initial conditions of disks such as temperature distributions and dust components as well as their evolution is crucial to the understanding of the stellar systems like ours.

Early studies used disk models powered by viscous accretion and/or stellar radiation (Bell & Lin, 1994; Kenyon & Hartmann, 1987; Hillenbrand et al., 1992; Hartmann et al., 1993; Chiang & Goldreich, 1997), which are sufficient to fit to the observed Spectral Energy Distributions (SEDs) of most YSOs as a whole. However the detailed spatial distribution of the disk emissions at different wavelengths is not constrained

because SEDs do not contain spatial information, leading to the degeneracy between important disk parameters such as disk temperature distribution and dust properties. Interferometry complements SEDs by spatially resolving the disks and breaking down the degeneracy, and offers a new angle to test and constrain the disk models (e.g. Ragland et al., 2012). In fact, because the temperature of a YSO disk drops towards larger radii, photons of different wavelengths trace different disk radii, which gives a convenient way for interferometry at different wavelengths to probe different parts of a disk.

It is generally accepted that disks consist of a dusty hot rim (Dullemond et al., 2001) at the innermost edge with sublimation temperature (Monnier & Millan-Gabet, 2002; Chen et al., 2012). The rim consists of large grains and receives direct emissions from the central star. It can be heated up to a few 1000K and contributes mainly to the near-infrared (NIR) excess. With high angular resolution, the NIR emissions of 11 YSOs for the first time were resolved by the IOTA interferometer (Millan-Gabet, 1999; Millan-Gabet et al., 2001), and the measured disk sizes are many times larger than expected sizes from standard geometrically thin and optically thick disks (Monnier & Millan-Gabet, 2002). A further study by spectrally dispersed NIR interferometry (Eisner et al., 2007) suggested the hot rim had a radial temperature profile, which might reflect a separation of gas and dust components with different temperature and spatial distribution.

The first Mid Infrared (MIR) nulling interferometry observations of three YSOs were not resolved (Hinz et al., 2001), suggesting much smaller MIR disk sizes then predicted by standard disks. A further study using longer baselines was able to resolve three out of 13 stars (Liu et al., 2005, 2007). However the constrained disk properties were quite different from those from other wavelength, which suggested a complex disk structure. Monnier et al. (2009) carried out a MIR disk size survey on 34 YSOs using the segmented Keck telescope. Most of the objects were partially resolved, but the constrained MIR sizes did not seem to correlate with the stellar luminosity (Figure 1.13). Long baseline MIR interferometric observations were able to resolve more YSO disks. However no unique model seemed to be able to fit both MIR SEDs
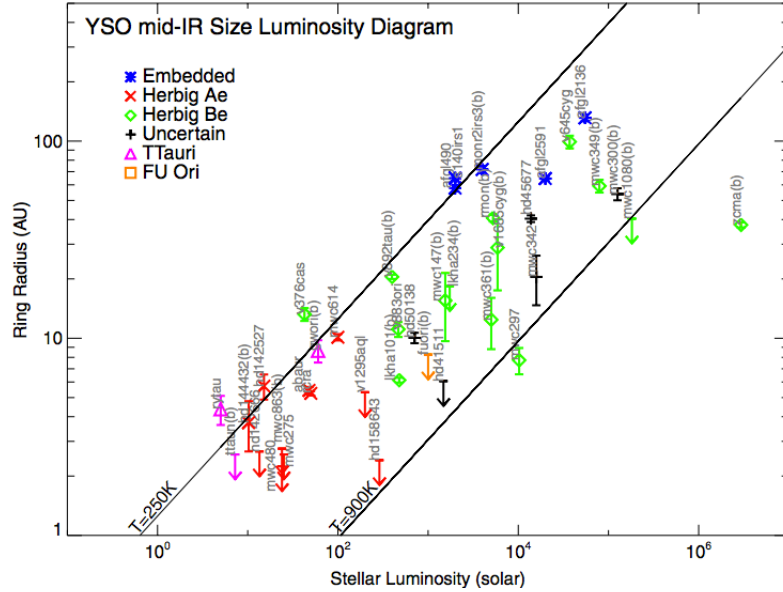
Figure 1.12. MIR disk size vs. stellar luminosity (reprinted from Monnier et al., 2009). YSOs are observed by the segmented Keck telescope.

and interferometric data (e.g. Ragland et al., 2012; Boley et al., 2013; Chen et al., 2012), suggesting the complexity of the YSO disks and posing a challenge for future theorists to build a better disk model.

Spectro-interferometry is another powerful tool in studying the YSO disks, because it not only resolves the disks, but also constrains the disk motion. Kraus et al. (2012a) were able to reproduce the measurements of a YSO disk from a spectro-interferometer across Brγ line with a Keplerian velocity field. Rousselet-Perraut et al. (2010) studied AB Aur by resolving the disk across Hα line, the results suggest disk winds are driven by magneto-centrifugal force. This conclusion is supported by spectro-interferometric observations of MWC297 in Brγ line (Weigelt et al., 2011). Eisner et al. (2010) spatially resolved the inner regions of YSOs across Brγ line, and determined the centroids of different velocity components of this gaseous emission. The model fitting results support the emission comes from an infall/outflow of the gaseous components rather than a disk.

23

1.2.9 Exozodiacal Dust

Exozodiacal dust is a layer of micron-sized dust that forms an optically thin disk around a star and can scatter the stellar light. It is the remnant of planet formation process, and can continue to exist for a long time thanks to the replenishment from the collisions of the large rocky bodies in the stellar systems. Hundreds of stars have been detected so far to contain exozodiacal dust, most of which are through their excess infrared emissions.

Characterizing exozodiacal dust has been an important task because it is one of the major sources that prevent directly imaging exoplanets. In fact, our own Earth may appear to be buried and undetectable in the zodiacal light to a distant observer. Therefore it is crucial to determine the exozodiacal light level to guide future space-based exo-Earth missions. On the other hand, the existence and morphology of the exozodiacal dust could be closely related to the dynamics of exoplanets (e.g. Thébault & Beust, 2001). So a study of the excess level and spatial distribution of exozodiacal dust could serve as an indicator of embedded exoplanets that are beyond detection.

Most of the detections of exozodiacal dust so far have been made in far-IR by space missions (e.g. Spitzer, WISE) because the dust lying at several tens of AU (analogous to the Solar systems Kuiper belt) from a solar-type star will reach a thermal equilibrium at several tens to a few hundreds of Kelvin, and can emit far-IR flux two orders of magnitude more than the stellar photospheric emission (e.g. Aumann et al., 1984; Trilling et al., 2008). However the hot (>300K) dust populations peaking at shorter wavelength in the inner planetary region are poorly known because the relative infrared excess to stellar emission is weaker at shorter wavelength. In addition, the spectro-photometry technique has an intrinsic limitation of how precisely the theoretical models can predict the infrared stellar photospheric fluxes.

Another way of detecting exozodiacal light is to use infrared interferometry to spatially resolve the dust emitting region. The infrared excess can be estimated by the difference between the calibrated visibilities and the expected visibilities from the stellar photosphere assuming the exozodiacal dust cloud is fully resolved. This technique has the advantage of being independent of absolute modeling and calibration

of the stellar spectrum. The only knowledge it requires is a crude estimation of the angular size of the host star.

Two types of interferometers are involved for studying exozodiacal light: MIR nulling interferometers (e.g. Keck Interferometer Nuller [KIN]) and high accuracy NIR interferometers (e.g. CHARA/FLUOR). Millan-Gabet et al. (2011) used KIN to study exozodiacal light around 25 nearby main sequence stars and found 1 significant detection and 2 marginal ones. Although interesting, this pioneering work does not provide enough positive detections to make a strong statistical estimation of how exozodiacal light varies as a function of stellar parameters. These measurements represent the best limits on detecting exozodiacal light with KIN. Another NASA funded project LBTI using nulling interferometry as KIN is expected to improve the sensitivity by a factor of 30.

On the other hand, high accuracy NIR interferometers, such as VLTI/VINCI (Absil et al., 2009), IOTA/IONIC (Defrère et al., 2011), and especially CHARA/FLUOR (Absil et al., 2013) are able to confirm most of the exozodiacal dust populations associated with detected cold debris disks by other methods, and detect several new ones. Absil et al. (2013) found 1% NIR excess within the first few AU around 11 main sequence AFGK stars out of 40 sampled with CHARA/FLUOR (Figure 1.13). In comparison, only 2 of these 11 stars show significant MIR excess by nulling interferometry (Stock et al., 2010). These results suggest that exozodiacal dust is more easily and abundantly detected in the NIR than in MIR.

1.3 Image Reconstruction

Since a true astronomical image and its corresponding complex visibilities in the (u,v) space are related by Fourier transformation (Equation 1.8), one can imagine in an ideal case where the full (u,v) space is sampled, a simple reverse Fourier transformation will be able to reconstruct the true image. This is equivalent to using a single dish telescope to some extent: each two little elements on the primary pupil samples a complex visibility in the (u,v) space, and all such pairs of elements cover the full (u,v) space within certain radius.
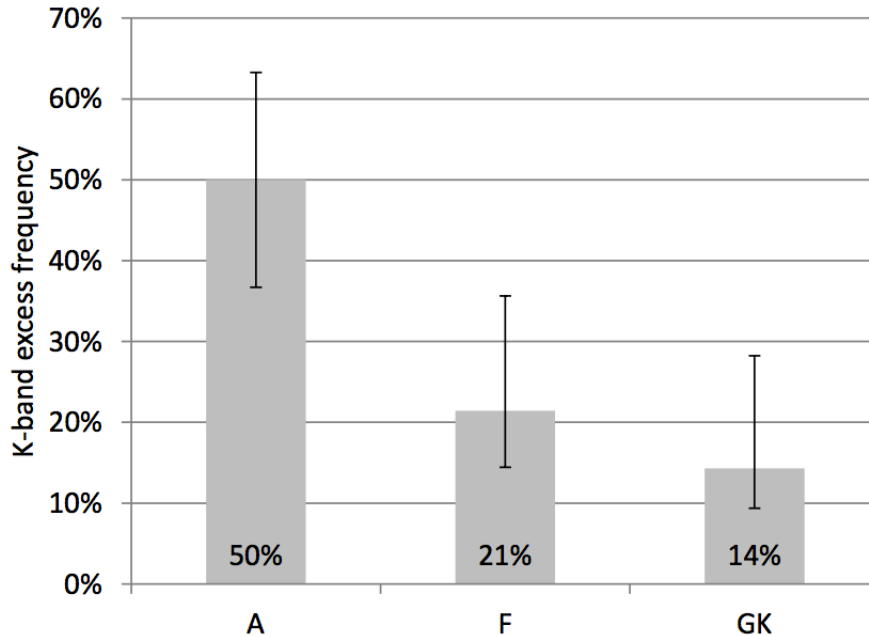
Figure 1.13. Percentage of K-band excess in the observed sample as a function of spectral type (reprinted from Absil et al., 2013).

For an optical interferometer in reality, only a limited number of telescopes are available, allowing a limited number of data points to be sampled in the (u,v) space. The problem gets worse due to the compromised phase information that can only be partially recovered from the data. As a result, reconstructing the image of an astronomical object with limited data has been a challenge in optical interferometry.

There are generally two approaches. The first one is to model the object by taking advantage of the pre-knowledge of the object. However this approach may be biased by which model one chooses, and the results are subject to the intrinsic uncertainties and limitations of the model. A second approach is to find the most likely image that agrees with the interferometric data while making the least assumptions about the object. This process is usually called image reconstruction, which has the great advantage of model-independency.

The number of images that agree with the data within the uncertainties could be infinite. Therefore it is necessary to place some constrains on the final image to break down the degeneracy. The constraints include non-negativeness and smoothness of the intensity distribution of an image. It is reasonable to assume the image intensity

Number of telescopes	3	4	5	6	10	20
Number of visibilities	3	6	10	15	45	190
Number of closure phases	1	4	10	20	120	1140
Number of independent closure phases	1	3	6	10	36	171
Percentage of phase information	33%	50%	60%	67%	80%	90%

Table 1.1. The number of visibilities and closure phases increase as a function of number of telescopes.

cannot be negative, but the approach may not be practical in some cases such as imaging at absorption lines. Smoothness is a requirement on the intensity within the angular resolution. Beyond the angular resolution, the degree of smoothness depends on the type of targets and imaging algorithms. Another constraint on the reconstructed images is a priori information. This constraint is somewhat arbitrary because it depends on how much is known about the target in advance. But it could be useful in highlighting interested components of the source and allowing imaging algorithms to converge to the final image faster.

The number of the sampled data points on (u,v) space and the evenness of their distribution are critical for image reconstruction. Modern imaging interferometers combines at least four telescopes, which measure 6 visibilities and 4 closure phases in a single snapshot. Adding more telescopes increases the number of data points rapidly because number of visibilities is proportional to n^2 and number of closure phases n^3, where n is the number of telescopes as shown in Table 1.1

The history of image reconstruction algorithms in radio interferometry is longer than that in optical interferometry. Some of popular algorithms in radio interferometry have been imported to optical interferometry, such as CLEAN first proposed by Högbom (1974). However radio interferometry usually has much larger number of antennas than the number of telescopes (6 telescope at most) in optical interferometry, yielding a much better (u,v) coverage. Plus in radio interferometry the phase information of complex visibilities could be obtained through phase-referencing or other processes, while in optical interferometry only part of phase information could be recovered through closure phases. Therefore even though algorithms such as CLEAN work most of time in radio interferometry, they do not work as well in optical inter-

ferometry.

Therefore better image reconstruction algorithms have been demanded in optical interferometry. Several groups have been developing new algorithms to improve the imaging results (Ireland et al., 2006; Thiébaut, 2008; Baron et al., 2012a). Here I will give an overview of two algorithms that have been used for the thesis work.

1.3.1   BSMEM

BSMEM is short for BiSpectrum Maximum Entropy Method, first developed and implemented in Fortran by David Buscher (Buscher, 1994). The idea of BSMEM (Baron & Young, 2008) is to reconstruct an image I from a set of data D including powerspectra and bispectra within noise using Bayesian statistics:

$$P(I|D) = \frac{P(I)P(D|I)}{P(D)}, \tag{1.18}$$

where $P(I|D)$ is the posterior probability density, $P(I)$ is the priori, $P(D|I)$ is the likelihood of the data give a certain image, $P(D)$ is the evidence. BSMEM tries to obtain the most likely image by maximizing the posterior probability iteratively.

Assuming Gaussian noise, the likelihood can be expressed as:

$$P(D|I) \propto \exp[-\frac{\chi_D^2(I)}{2}], \tag{1.19}$$

where $\chi_D^2(I)$ is the sum of χ^2 of the powerspectra and bispectra.

The priori takes the form of :

$$P(I) \propto \exp[\alpha H(I)], \tag{1.20}$$

where α is a real number, and $H(I)$ is an entropy function. There are several forms of the entropy function, one of them that is commonly used is the Gull-Skilling entropy (Gull & Skilling, 1984):

$$H(I) = \Sigma_{k=1}^{N}(I_k - M_k) - I_k \log(\frac{I_k}{M_k}), \tag{1.21}$$

where M is the given priori image, which is normally assumed to be a Gaussian disk or uniform disk, and k is the index of the pixels.

Therefore maximizing the posterior is equivalent to minimizing $J(I)$:

$$J(I) = \chi_D^2(I) - \alpha H(I) \tag{1.22}$$

where α is a regularization factor that balances the agreements to the data and the given priori image.

1.3.2 MACIM

MACIM (Ireland et al., 2006) also uses Bayesian theorem as shown in Equation 1.19 to maximize the posterior. It also pre-defines a priori $P(I)$ that can be used as a regularization of the final image. The difference is that instead of directly evaluating Equation 1.19, MACIM use a Monte-Carlo Markov Chain technique to sample the regions of image space where the posterior is highest.

The image space can be represented by a vector of flux elements. For each Markov Chain step, one or several of the flux elements can move randomly, new flux elements can be added, or old ones can be removed. Whether the new image will be accepted is a random process whose probability is determined by the χ^2 difference between the new image and old image. The probability is also affected by a regularizer which describes the properties of the image such as smoothness.

Another kind of regularizer is called dark interaction energy regularizer, which is the sum of all pixel boundaries with zero flux on either size of the pixel boundary. This regularizer encourages large regions of dark space in-between regions of flux, and therefore is very useful for imaging objects with clearly defined edges such as a stellar surface.

Another important feature of MACIM is that it allows a mixture of model fitting and imaging. For example, if ones tries to image a disk around a star where the star is not resolved, a single point source can be placed in the image to represent the star. And the only free parameter in the model is the flux ratio between the star and the disk.
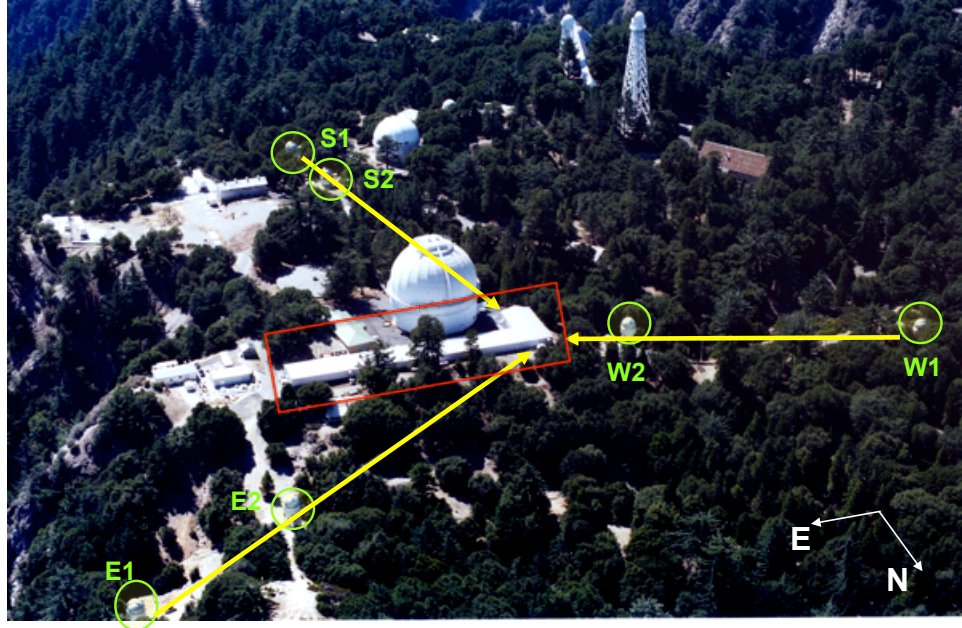
Figure 1.14. A bird-view of CHARA. The green circles highlights the six 1-m diameter telescopes. The photons collected by the telescopes propagates inside vacuum pipes (yellow arrows) to the beam combination laboratory highlighted by red square.

1.4 CHARA/MIRC

This whole PhD thesis including scientific research and instrumental developments, are carried out using the Michigan InfraRed Combiner (MIRC) at the Center for High Angular Resolution Astronomy (CHARA) array. In this section, I will give a brief introduction of them.

The CHARA interferometer array (ten Brummelaar et al., 2005, 2008) is located on Mount Wilson in California and operated by Georgia State University. The CHARA Array consists of six 1-meter telescopes arranged in a "Y" shape with 2 telescopes in each arm as shown in Figure 1.14 . It can potentially provide 15 baselines simultaneously ranging from 34 to 331 meters, possessing the longest baselines in optical/infrared of any functioning facility. With these baselines, CHARA offers high angular resolution up to ~ 0.4 mas at H band and ~ 0.7 mas at the K band to resolve nearby stellar systems including multi-object systems, circumstellar disks, rapidly rotating stars and spotted stars. More than 90 science papers have been published with observations at CHARA since commissioning in 2004.
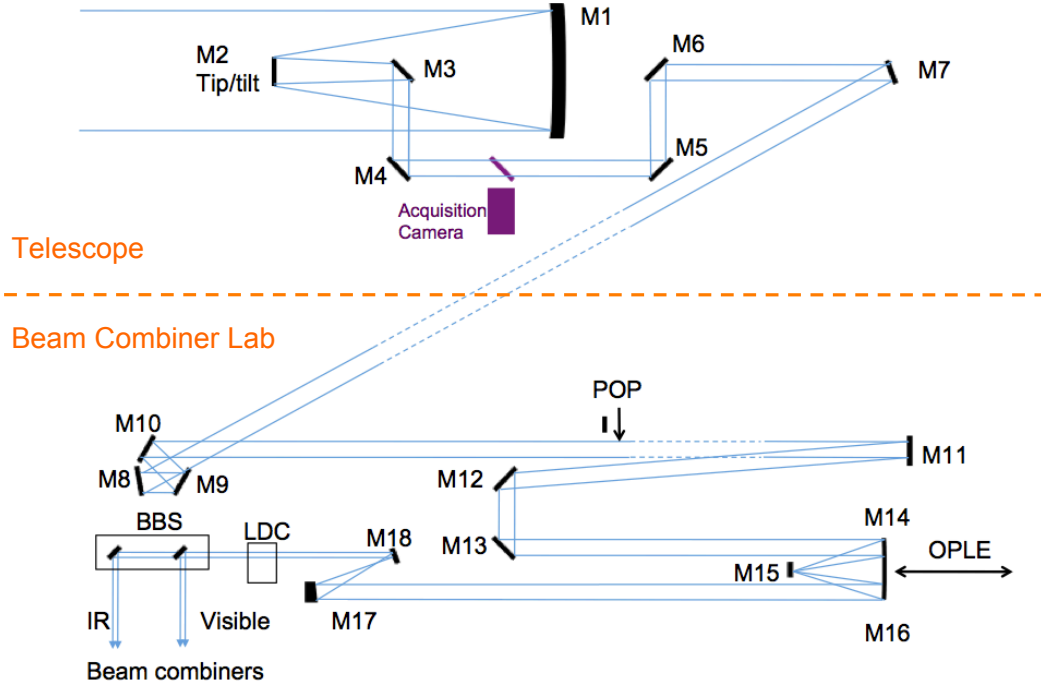
Figure 1.15. The beam path of one of the telescopes at CHARA array (Che et al., 2013). The blue indicates the beam path and the black are optics. The horizontal dashed line divides the optics into two parts. The ones above the line are inside a telescope, and the other ones are in the Beam Combiner Lab.

Figure 1.15 shows a typical beam path as well as optics from a telescope to the beam combiner lab at CHARA. The light collected by a telescope is guided through a vacuum pipe (between M7 and M8) into the beam combination laboratory. Mirrors M8-10 are used to match the polarization between different beams. The optical path difference between different beams are compensated in two stages. The first stage occurs in vacuum (between M10 and M11) and uses six parallel mirrors (PoP) to select appropriate delay segments. The mirrors of PoP can be remotely controlled to move in and out of the beam path. The second stage Optical Path Length Equalizers (OPLEs) uses cats-eye retro-reflectors which can move continuously on a 46m long steel rail.

The beams are then split into visible and near infrared by dichroics, and propagates into different beam combiners. One of them is Michigan Infrared Combiner (MIRC). A schematic drawing of MIRC is shown in Figure A.1. MIRC is an image-plane, near-infrared (H and K bands) combiner, designed to perform model-

independent interferometric imaging (Monnier et al., 2004, 2006). In order to obtain stable measurements of visibility and closure phase, MIRC utilizes single-mode fibers to spatially filter out the atmospheric turbulence. The fibers are arranged on a v-groove array with a non-redundant pattern so that each fringe has a unique spatial frequency signature. The beams exiting the fibers are collimated by a microlens array and then focused by a spherical mirror to interfere with each other. Since the interference fringes only form in one dimension which is parallel to the v-groove, they are compressed and focused by a cylindrical lens in the dimension perpendicular to the v-groove to go through a slit of a spectrograph. The spectrograph can be a prism with resolution R $\sim$ 45, a grism with R $\sim$ 150 or a grism with R $\sim$ 450. Finally the dispersed fringes are detected by a PICNIC camera. The philosophy of the control system and software is to acquire the maximum data readout rates in real time. The details about the software can be found in Pedretti et al. (2009).

MIRC had used indirect methods of measuring fluxes from individual telescopes, resulting in $\sim$ 10% uncertainty in visibility measurements. The large uncertainty allowed model parameters of observed targets to vary in a large range, and hindered MIRC from exploring deeper and broader area of astrophysics. One way to improve the data quality was to directly measure the beam fluxes by splitting the beams after the single-mode fibers, as was first proposed by Coudé du Foresto et al. (1997). The upgrade was carried out in 2009 (Che et al., 2010), and decreased the uncertainty of visibility measurements to $\sim$ 3%. The details of the upgrade are presented in Appendix A.

Another upgrade of MIRC was carried out in 2011 to expand it from a 4-beam combiner to a 6-beam combiner (Che et al., 2012a). MIRC was a four-beam combiner, measuring 6 visibilities and 4 closure phases simultaneously. To exploit the full advantage of 6 CHARA telescopes, we upgraded MIRC to a six-beam combiner in July 2011. The upgraded MIRC measures 15 visibilities and 20 closure phases simultaneously, which greatly boosts the imaging and modeling abilities of more complicated stellar systems such as circumstellar disks. The details of the upgrade are presented in Appendix B

The MIRC data reduction pipeline is described in Monnier et al. (2007), and was validated by using data on the calibration binary ι Peg. The pipeline first computes uncalibrated squared-visibilities and complex triple amplitudes after a series of background subtractions, Fourier transformations and foreground subtractions. Then the uncalibrated squared-visibilities and complex triple amplitudes are calibrated by the fluxes measured simultaneously with fringes.

CHAPTER 2

Rapid Rotators

The work of this chapter has been published (Che et al., 2011), much of the content has been extracted from the paper.

2.1 Introduction

While almost all cool stars rotate slowly, rapid rotation is the norm for hot stars. A large fraction of hot stars are observed to be rotating with equatorial velocities larger than 120 km s^{-1} (Abt & Morrell, 1995; Abt et al., 2002). Such fast stellar rotation can have strong effects on the observed stellar properties. The strong centrifugal forces distort stellar shapes and make them oblate. Stellar surface temperatures vary across latitudes due to the gravity darkening effect (von Zeipel, 1924a,b). Lower effective gravities at the equator results in lower temperatures compared to the poles. This temperature distribution implies that apparent luminosities L_{app} and apparent effective temperatures $T_{\mathrm{app}}^{\mathrm{eff}}$ depend on inclination angles, and the overall values are hidden from observers. Stellar rotation can also affect the distribution of chemical elements, mass loss rate and stellar evolution (Meynet & Maeder, 2000). Some kind of rapidly rotating massive stars may end up as γ-ray bursts (MacFadyen & Woosley, 1999).

Stellar rotation has been studied mainly through the Doppler broadening of line profiles, but the obtained information from these studies is limited due to the lack of spatial knowledge of stars, such as the inclination angles. An important and reliable way to extract such information is through long baseline optical/infrared interferometry, allowing us to study the detailed stellar surface properties for the first

time. Several rapid rotators have been well studied using this techniques, including Altair, Vega, Achernar, Alderamin, Regulus and Rasalhague (van Belle et al., 2001, 2006; Aufdenberg et al., 2006; Peterson et al., 2006; Domiciano de Souza et al., 2003; Monnier et al., 2007; Zhao et al., 2009).

These studies have revealed not only the stellar surface geometry but also the surface temperature distributions, allowing us to test and constrain stellar models. For instance, the surface temperature distributions have confirmed the gravity-darkening law in general, but deviate in detail from the standard von Zeipel model ($T_{\mathrm{eff}} \propto g_{\mathrm{eff}}^{\beta}$, where $\beta = 0.25$ for fully radiative envelopes). Particularly the studies on Altair and Alderamin prefer non-standard β values from the modified von Zeipel model (the β-free model in Zhao et al., 2009). These results imply the gravity darkening law is probably only an approximation for the surface temperature distribution, the real physics behind is still to be uncovered.

In this work we have studied two additional rapidly rotating stars with different spectral types from all the A type stars we have studied: β Cassiopeiae and α Leonis, observed with CHARA/MIRC.

2.2 Modeling of Rapid Rotators

We construct a 2D stellar surface model: the modified von Zeipel model. The model contains six free parameters (Figure 2.1), stellar polar radius, the polar temperature, the ratio of angular velocity to critical speed $\omega / \omega_{\mathrm{crit}}$, the gravity darkening coefficient (β), the inclination angle, and the position angle (east of north) of the pole, to describe the stellar radius, surface effective gravity and temperature distributions across stellar surface. The mass of a star is given and fixed in each model fitting process. Given the stellar mass, stellar polar radius and $\omega / \omega_{\mathrm{crit}}$, the stellar radius and surface effective gravity at each latitude can be determined (Aufdenberg et al., 2006). Then given the stellar polar temperature and β, the stellar surface temperature distribution can be computed from the gravity darkening law($T \propto g_{\mathrm{eff}}^{\beta}$). Lastly the orientation of the star is described by the inclination angle and position angle. In the model, we assume the solid-body rotation for simplicity; a more complicated and realistic model
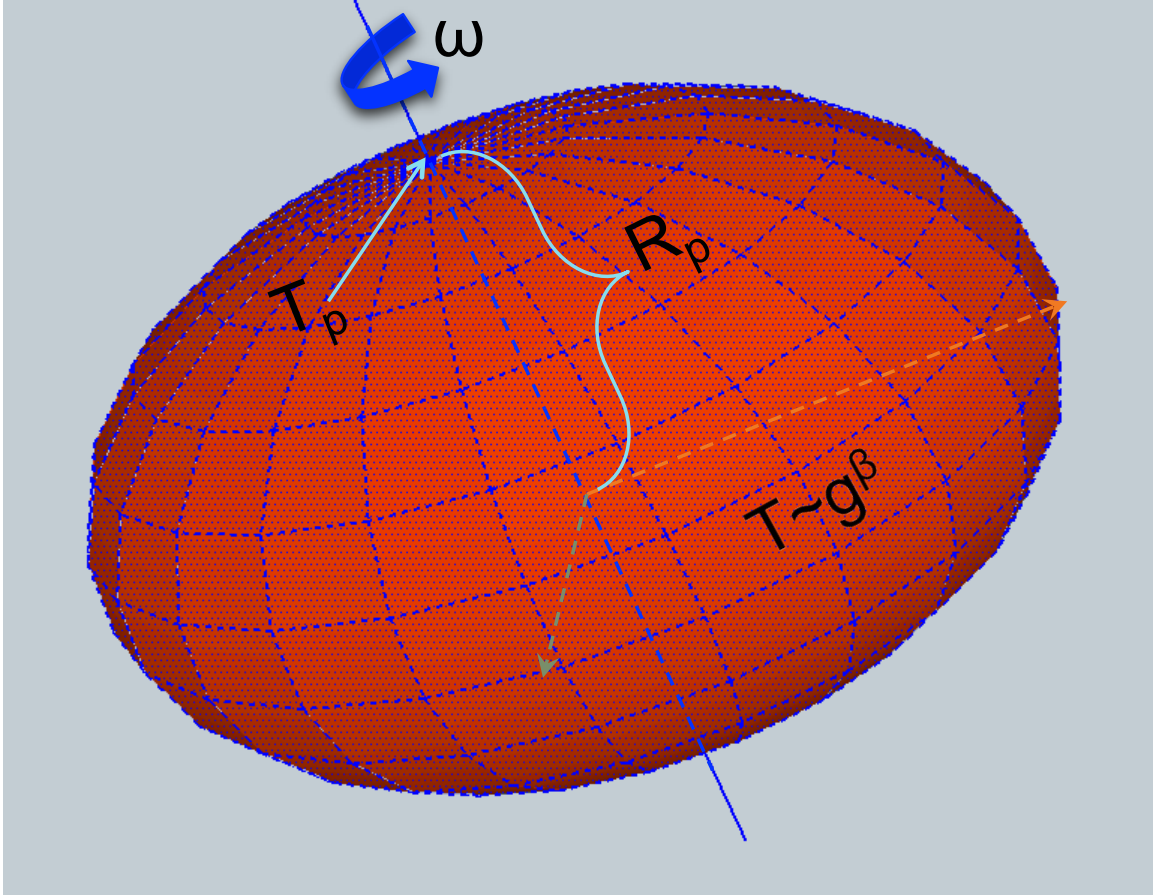
Figure 2.1. Schematics of a rapid rotator model. The inclination angle and position angle are not presented.

would consider the differential rotation which requires additional information (such as spectral lines) for fitting. The gravity darkening coefficient β is a free parameter in the model. By fixing β, the model reduces to the standard von Zeipel model ($\beta = 0.25$, radiative case) or Lucy model ($\beta = 0.08$, convective case).

In earlier work (Monnier et al., 2007), we found that allowing β to be a free parameter greatly improved the fit to the interferometric data. This flexibility allows us to independently test the validity of the standard von Zeipel and Lucy prescriptions. Furthermore, the mixture of radiative and convective regions in the same star may also cause deviations from expected values. For example, the polar temperature could be thousands of degrees higher than the equator temperature, resulting in a situation where upper atmosphere may be radiative at the poles while convective at

the equator. In general, the value of β also depends on various approximations made for the atmosphere, radiation transfer etc. (Claret, 1998). Therefore in our modified von Zeipel model, instead of setting β to be fixed, we allow β to change as a single free parameter of the model to fit the interferometric data. For comparison, we also present models with β fixed to the appropriate standard value. The error bars of stellar parameters from the modified von Zeipel model are in general larger than those from standard von Zeipel model or Lucy model. This is because there are certain degrees of degeneracies between the gravity darkening coefficient β and other stellar parameters, as discussed below.

During the model fitting process, the modified von Zeipel model is converted into a projected stellar surface brightness model, which is constrained by the observed V and H band photometric fluxes and three kinds of interferometric data from each night: squared visibilities, closure phases and triple amplitudes (see Section 1.1.2). In the modified von Zeipel model, the stellar surface is divided into small patches. The intensity of each patch is computed from a Kurucz model (Kurucz, 1992)[1] given the temperature, gravity, viewing angle and wavelength, so that the modified von Zeipel model can be converted into the projected brightness model. The projected brightness model is then converted into the same three kinds of interferometric data above by a direct Fourier transform to fit to the observed data. We use 4 sub-bands (binning two adjacent narrow channels dispersed by the MIRC prisms) across the H band for accuracy. In addition, the apparent V and H band photometric fluxes are obtained from the projected brightness model to fit to the observed values. The observed $v \sin i$ is not directly used in the model fitting, but is used to cross-check the results from model fitting. The detailed process is described in Zhao et al. (2009) and reference therein.

Data errors consist of random errors, errors due to variation of seeing condition, and calibration errors from using incorrect diameters of the calibrator targets. To get the errors from the first two parts, we treat the data from each night as a whole package and bootstrap packages randomly with replacement. Then we fit the sampled

---

[1]Data downloaded from kurucz.harvard.edu/

data and repeat fifty times to get the distribution of each model parameter. The upper and lower error bars quoted here are such that the interval contains 68.3% probability and the probability above and below the interval are equal. For the error from the third part, we used simple Monte Carlo sampling using the our estimated angular size uncertainties – these errors turned out to be somewhat smaller than the error from the first two parts.

We should point out that the stellar mass has to be given and fixed at the beginning of each model fitting process, but at first does not agree in detail with the model estimated from the fitting results on both L-R_{pol} and HR diagrams using the rotational correction (see Section 2.6). Our approach here has been to adopt the mass from the literature for the first attempt in the model fitting. The mass estimation from the first attempt is then used in the second round of the model fitting. This procedure is repeated until the mass given in the model agrees with what comes out of the model fitting. The final mass is referred as the model mass. The stellar metallicity is adopted from the literature and fixed throughout. The distance of the target is also adopted from the literature.

We also calculate the stellar mass based on the measured $v \sin i$ range from the literature, which is referred as the oblateness mass and was first proposed by Zhao et al. (2009). For each bootstrap, we extract the inclination angle, polar radius and $\omega / \omega_{\mathrm{crit}}$ from the best fitting, then uniformly sample $v \sin i$ values 100 times in the given range to obtain a mass distribution. By combining the mass distribution from each bootstrap, we obtain the whole mass distribution from which the upper and lower mass bound can be calculated such that the interval contains 68.3% probability and the probability above the upper bound and below the lower bound are the same. To compute the best estimation of the stellar mass, we use the best estimations of the inclination angle, polar radius and $\omega / \omega_{\mathrm{crit}}$ from the model fitting of all nights, and the $v \sin i$ value to be the mean of the measured range from the literature.

2.3 Imaging Of Rapid Rotators

We use the application MACIM (Ireland et al., 2006) to construct images for rapid rotators. It is usually difficult to image nearly point-symmetric objects because the closure phases will be close to either 0 or 180 degrees, making it harder to constrain the detailed structure. β Cas is close to pole-on and α Leo is almost equator-on, which are two cases of the point-symmetry, as will be shown in the following sections.

One strategy to image these kinds of stars is to take advantage of some prior knowledge. Stars have clear boundaries with elliptical shapes approximately. Therefore we employ a prior image which is an ellipse with uniform surface brightness. The spatial and geometric parameters of the ellipse come from the model fitting. The detailed process can be found in Monnier et al. (2007).

2.4 α Leo

2.4.1 Background

α Leonis (Regulus, HR3982) has $V = 1.391$ (Kharchenko et al., 2009), $H = 1.658$ (Cutri et al., 2003), 1.57 (Ducati, 2002), distance $d = 24.31$ pc (van Leeuwen, 2007). It is a well-known rapidly rotating star, classified as a B7V (Johnson & Morgan, 1953) or B8 IVn (Gray et al., 2003). The $v \sin i$ measurements from the literature range from ~ 250 km s^{-1} (Stoeckley et al., 1984) to ~ 350 km s^{-1} (Slettebak, 1963) and we have adopted here the recent precise value 317 ± 3 km s^{-1} from McAlister et al. (2005). Regulus is also a famous triple star system with the companions B and C forming a binary system at ~ 175” away from α Leonis A (McAlister et al., 2005). Recently Gies et al. (2008) has discovered that α Leonis A is also a spectroscopic binary with a white dwarf companion (~ 0.3 M$_\odot$) with an orbital period ~ 40.11 d. The primary mass has been estimated to be ~ 3.4 M$_\odot$(McAlister et al., 2005), however our study here will show it is much more massive. The diameter of Regulus has been estimated several times in the past because of its brightness and relatively large angular size. McAlister et al. (2005) combined the CHARA K-band interferometric data and a number of constraints from spectroscopy and revealed that Regulus has

Target	Obs. Date	Telescopes	Calibrators
α Leo	UT 2008Dec03	S1-E1-W1-W2	θ Leo
	UT 2008Dec04	S1-E1-W1-W2	54 Gem, η Leo
	UT 2008Dec05	S1-E1-W1-W2	θ Hya, θ Leo
	UT 2008Dec06	S1-E1-W1-W2	54 Gem, θ Hya, η Leo
	UT 2008Dec08	S1-E1-W1-W2	θ Leo
β Cas	UT 2007Aug07	S1-E1-W1-W2	7 And
	UT 2007Aug08	S1-E1-W1-W2	σ Cyg, 7 And
	UT 2007Aug10	S1-E1-W1-W2	σ Cyg, 37 And
	UT 2007Aug13	S1-E1-W1-W2	σ Cyg, 7 And, Ups And
	UT 2009Aug11	S1-E1-W1-W2	7 And, γ Tri
	UT 2009Aug12	S1-E1-W1-W2	7 And, γ Tri
	UT 2009Oct22	S2-E1-W1-W2	37 And, υ And, ϵ Cas, η Aur

Table 2.1. Observation logs of α Leo and β Cas at CHARA/MIRC.

the polar radius $R_{pol} = 3.14 \pm 0.06$ $R_\odot$ and the equatorial radius $R_{eq} = 4.16 \pm 0.08$ $R_\odot$.

2.4.2 Observations

α Leo was observed by CHARA/MIRC on 5 nights in 2008. The detailed log of the observation is presented in Table 2.1 and the calibrators in Table 2.2. The (u,v) coverage of the observations is shown in Figure 2.2.

2.4.3 Model Fitted Results

We first fit the stellar surface of the modified von Zeipel model to the interferometric data of α Leo . The parameters we adopted from the literature are given as following: distance = 24.31 pc (van Leeuwen, 2007), metallicity [Fe/H] = 0.0 (Gray et al., 2003). Mass = 3.4 $M_\odot$ (McAlister et al., 2005) was used for the first attempt of the model fitting. The fitting results from the modified von Zeipel model are shown in Figure 2.3, with the final stellar parameters listed in the middle column of Table 2.3. α Leo is rotating at 96% of its critical speed, causing the equatorial radius about 30% longer than the polar radius. The temperatures at the poles are more than 3000K hotter than that at the equator. The gravitational darkening coefficient β from the fitting is different from the "standard" values for either radiative or convective envelopes. The results show that α Leo is almost equator-on, which is shown as a

Calibrator	UD Diameter	Reference
7 And	0.659 ± 0.017	b, c, d
37 And	0.682 ± 0.030	b, c
υ And	1.14 ± 0.007	a, b, c, d
σ Cyg	0.542 ± 0.021	a
γ Tri	0.520 ± 0.0125	b
ϵ Cas	0.351 ± 0.024	c, d
η Aur	0.419 ± 0.063	c
θ Leo	0.678 ± 0.062	b, c
η Leo	0.644 ± 0.068	c
54 Gem	0.735 ± 0.033	b, c
θ Hya	0.463 ± 0.031	c, d

[a] Mérand (2008)

[b] Kervella & Fouqué (2008)

[c] Barnes et al. (1978)

[d] Bonneau et al. (2006)

Table 2.2. The calibrators used for CHARA/MIRC observations.
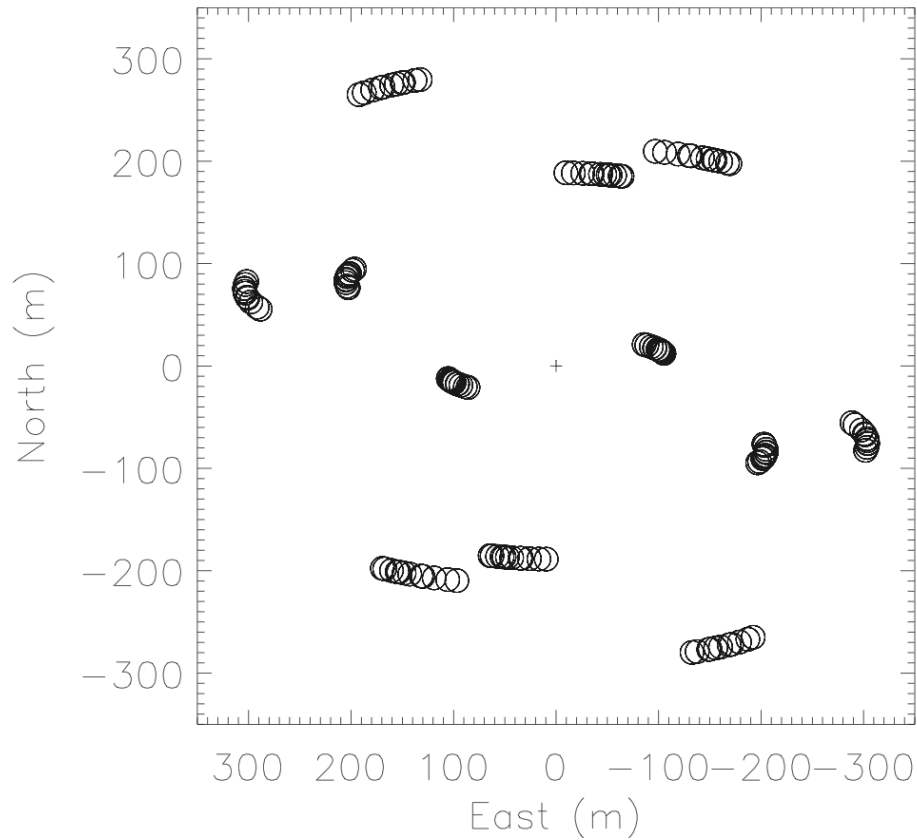
Figure 2.2. (u,v) coverage of α Leo for 5 nights of observations by CHARA/MIRC (Che et al., 2011).

dark strip in Figure 2.5 in the following subsection. Therefore the $L_{\rm bol}$ is higher than the $L_{\rm app}$. The model mass from HR diagram is 4.15 ± 0.06 M$_\odot$. Adopting the $v \sin i$ range $v \sin i = 317 \pm 3$ km s^{-1} from McAlister et al. (2005), the oblateness mass estimation corresponding to the model mass is $3.66^{+0.79}_{-0.28}$ M$_\odot$, which also agrees with the model mass within the errors. The large errors of the oblateness mass is due to the degeneracy of stellar parameters as discussed later. The observed $v \sin i$ (McAlister et al., 2005) is consistent with our derived value 336^{+16}_{-24} km s^{-1} with error bars.

Theoretically the high surface temperature of α Leo suggests that the envelope is fully radiative, corresponding to the gravity darkening coefficient $\beta = 0.25$. We fit the model again using the fixed β value, which is the standard von Zeipel model. The best fitting χ^2s for this model are much worse, nearly a factor of 2 higher. For completeness, we have included the results in the right column of Table 2.3. In this scenario, α Leo is rotating even faster. The larger gravitational darkening coefficient and faster rotation imply even larger temperature difference between the poles and equator. However the derived equatorial temperatures from the modified and standard von Zeipel models agree with each other. This is because Regulus is almost equator-on, the observed interferometric data is dominated by information from the equator. The χ^2s of the various interferometric data from the modified von Zeipel model are all significantly smaller than those from the standard von Zeipel model, supporting the modified von Zeipel model with $\beta = 0.19$ is preferred to describe the surface properties of Regulus, ruling out the standard von Zeipel value. This conclusion is also supported by the disagreements between the model mass and oblateness mass from the standard von Zeipel model, and between the model and observed $v \sin i$ values.

We expect some degeneracies of parameters from the modified von Zeipel model fitting because of the symmetry of the equator-on orientation. Therefore we explore the probability spaces of gravity darkening coefficients β with inclination angles and $\omega / \omega_{\rm crit}$ to assess possible correlations. For example, we first search the best model fitting results of all nights on a 40×40 grid of β and inclinations by fixing these two
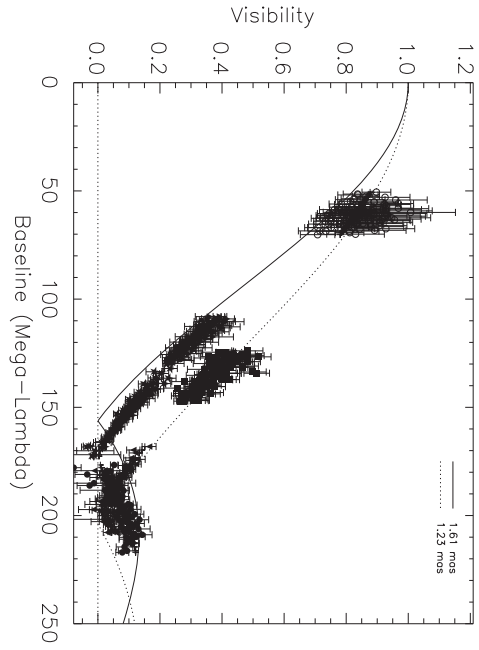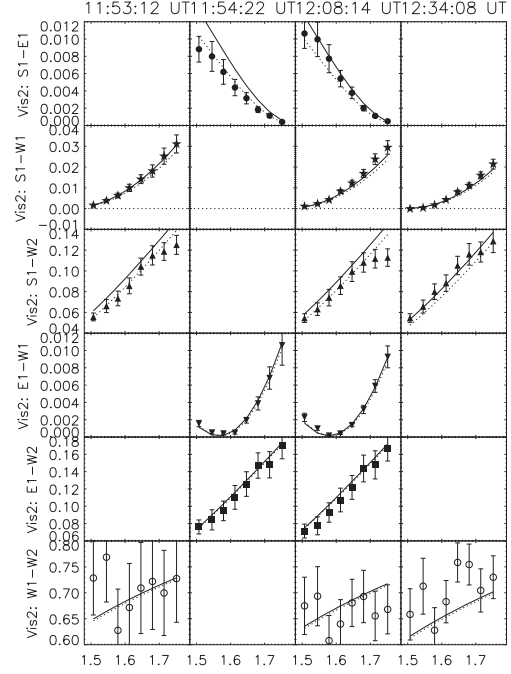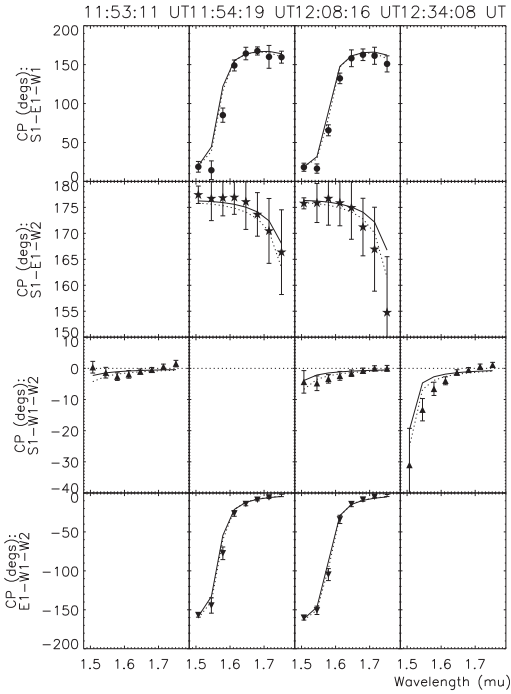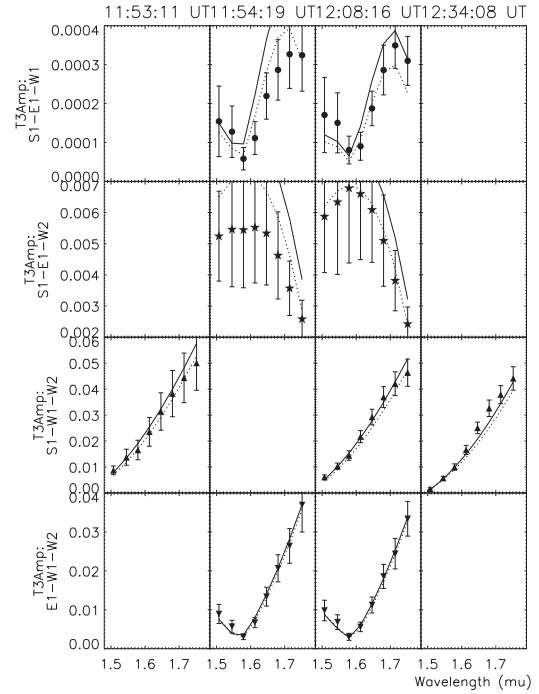
Figure 2.3. Upper left panel: all seven nights visibility data of α Leo . The solid line and dotted line show the visibility curves of uniform disks with diameters of major and minor axis of α Leo from model fitting. The rest panels: the modified von Zeipel model (solid line) and MACIM image (dotted line) vs. observed data (filled points with error bars) of α Leo from one single night. The reduced χ^2 of model is 1.32 and that of image is 0.78. The eight data points in each sub-panel are from eight sub-channels of MIRC observation across H band. The x axis shows the wavelengths corresponding to the data points. The y axis shows which telescopes of CHARA have been used. All the panels are reprinted from Che et al. (2011).

Model Parameters	Modified von Zeipel model (β-free)	von Zeipel model ($\beta = 0.25$)
Inclination (degs)	$86.3^{+1.0}_{-1.6}$	$87.5^{+0.2}_{-0.1}$
Position Angle (degs)	258^{+2}_{-1}	259^{+1}_{-2}
T_{pol} (K)	14520^{+550}_{-690}	16190^{+150}_{-110}
R_{pol} (mas)	$0.617^{+0.010}_{-0.009}$	$0.605^{+0.001}_{-0.001}$
$\omega / \omega_{\mathrm{crit}}$	$0.962^{+0.014}_{-0.026}$	$0.969^{+0.001}_{-0.002}$
β	$0.188^{+0.012}_{-0.029}$	0.25 (fixed)
Derived Physical Parameters		
T_{eq} (K)	11010^{+420}_{-520}	10920^{+100}_{-70}
R_{eq} ($R_{\odot}$)	$4.21^{+0.07}_{-0.06}$	$4.17^{+0.007}_{-0.006}$
R_{pol} ($R_{\odot}$)	$3.22^{+0.05}_{-0.04}$	$3.16^{+0.005}_{-0.004}$
Bolometric luminosity L_{bol} ($L_{\odot}$)	341^{+27}_{-28}	431^{+18}_{-9}
Apparent effective temperature $T^{\mathrm{eff}}_{\mathrm{app}}$ (K)	12080	12650
Apparent luminosity L_{app} ($L_{\odot}$)	252	294
Model $v \sin i$ (km s^{-1})[a]	336^{+16}_{-24}	346^{+1}_{-2}
Rotation rate (rot/day)	$1.64^{+0.02}_{-0.04}$	$1.70^{+0.01}_{-0.01}$
Model mass ($M_{\odot}$)[b]	4.15 ± 0.06	4.52 ± 0.05
Oblateness mass ($M_{\odot}$) [c]	$3.66^{+0.79}_{-0.28}$	$3.44^{+0.08}_{-0.01}$
Age (Gyr)[b]	0.09 ± 0.02	0.05 ± 0.01
Model V Magnitude[d]	$1.393^{+0.002}_{-0.005}$	$1.329^{+0.017}_{-0.021}$
Model H Magnitude[d]	$1.578^{+0.004}_{-0.006}$	$1.550^{+0.012}_{-0.015}$
χ^2 of various data		
Total χ^2_ν	1.32	2.57
Vis^2 χ^2_ν	0.76	1.26
CP χ^2_ν	1.97	3.80
T3amp χ^2_ν	0.92	1.52
Physical Parameters from the literature		
[Fe/H][e]	0.0	
Distance (pc)[f]	24.31	

[a] Observed $v \sin i$ = 317 ± 3 km s^{-1} (McAlister et al., 2005)

[b] Based on the Y^2 stellar evolution model (Yi et al., 2001, 2003; Demarque et al., 2004)

[c] Zhao et al. (2009)

[d] Vmag = 1.391 ± 0.007 (Kharchenko et al., 2009), Hmag = 1.658 ± 0.186 (Cutri et al., 2003), 1.57 ± 0.02 (Ducati, 2002)

[e] Gray et al. (2001)

[f] van Leeuwen (2007)

Table 2.3. Best-fit and physical parameters of α Leo

parameters on each pixel. Generally if the uncertainties of the data are independent, then the probability of fitted model parameters falling into each pixel is $\propto e^{-0.5\chi^2}$. However in reality the data errors are correlated, we modify the probability $\propto e^{-\alpha\chi^2}$, where α is a variable to be determined. Then we overplot the results of the two parameters from each bootstrap onto the probability space (not shown in the figure), and find the contour of the same χ^2 containing 68.3% of bootstrap results, from which α can be computed. The contour is defined as 1-σ.

Two figures of probability space of ω / ω_{crit} and the inclination vs. β are shown in Figure 2.4. Both pictures show a strongly elongated contour of the probability, implying significant correlation between these parameters. The solid contours show the 68.3% probability. We overplot the observed $v\sin i$ range from McAlister et al. (2005), which intersects the contour with a much smaller common area. Therefore a precise $v\sin i$ measurement would significantly reduce the degeneracy between the parameters and constrain them much better.

Based on only visibility data, McAlister et al. (2005) modeled α Leo and our new model results are generally consistent with this earlier work. Since MIRC has higher angular resolution, better UV coverage and the closure phase data, our data is more sensitive to the detailed structures such as the inclination and position angles. This work found acceptable fits for β values between 0.12 and 0.34 (best fit at 0.25), a range consistent with our more refined analysis. Although our estimates of the bolometric luminosity L_{bol} of Regulus are similar to those from their paper, the HR diagram (Figure 2.10) from our results suggests that the mass of the non-rotating equivalent of Regulus is $4.15 \pm 0.06\,\mathrm{M_\odot}$, much more massive then the $3.4 \pm 0.2\,\mathrm{M_\odot}$ that McAlister et al. (2005) obtained using the surface gravity $\log g$ from spectral analysis. Their results show that the non-rotating equivalent of Regulus has lower mass and consequently lower L_{bol} than rapidly rotating Regulus, which is in contrast to what Sackmann (1970) found, that a non-rotating equivalent actually has higher L_{bol} than its rapidly rotating equivalent.
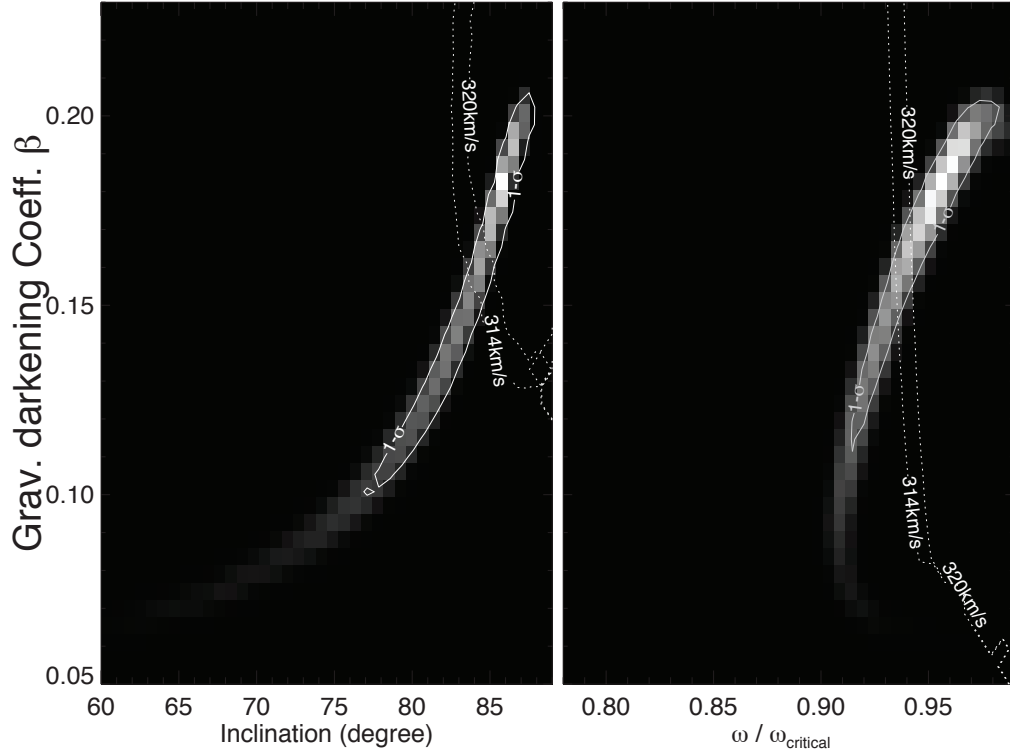
Figure 2.4. Probability spaces of α Leo show the degeneracy between stellar parameters. The left panel shows the probability space of the gravity darkening coefficient β and the inclination angle; the right one shows that of β and the fraction of critical angular velocity $\omega / \omega_{\text{crit}}$. The solid contours represent the 1-σ levels, containing 68.3% of the probability. The strong elongation of the contours in both panels suggest a strong correlation between these parameters. The dashed lines connect pixels in the probability space with the same $v \sin i$ values from model fitting. The $v \sin i$ value range is taken from McAlister et al. (2005), which intersects the probability contours with smaller common areas. Both panels are reprinted from Che et al. (2011).

2.4.4 Imaging

The left panel of Figure 2.5 shows the image of α Leo with latitudes and longitudes from the model, and surface brightness temperature contours. The reduced χ^2 of the image is 0.78. The right one shows the image from model fitting. α Leo is almost equator-on and the dark equator stretches along the North-South direction. One noticeable phenomenon is that the poles are not located exactly in the hot region. This is because in this particular case the poles at the stellar image edge look cooler due to limb-darkening, causing the brightest regions to shift towards the center of the image.
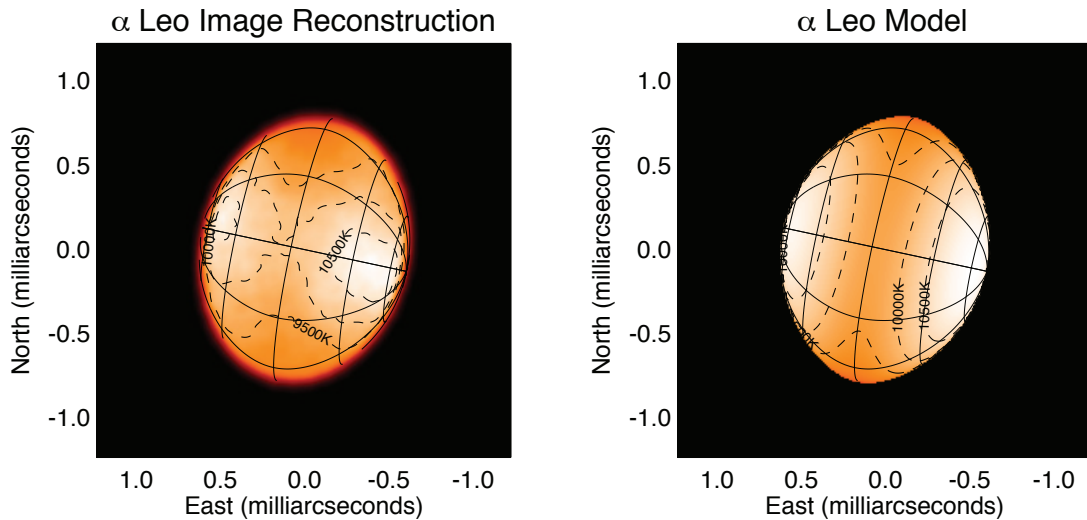
Figure 2.5. Images of α Leo . The left one shows the surface intensity distribution of α Leo from MACIM, overplotted with latitudes and longitudes from the model. The angular resolution is 0.55 mas (milli-arcsecond). The dashed contours represent the surface brightness temperatures of the image. The right one shows the image from model fitting, overplotted with brightness temperature contour from the model. The reduced χ^2 of the images from MACIM and model fitting are 0.78 and 1.32. Both images are reprinted from Che et al. (2011).

2.5 β Cas

2.5.1   Background

β Cassiopeiae (β Cas, Caph, HR21) has $V = 2.27$, (Morel & Magnenat, 1978), $H = 1.584$ (Cutri et al., 2003), 1.43 (Ducati, 2002), and is located at $d = 16.8$ pc (van Leeuwen, 2007). Its mass has been estimated as 2.09 $M_\odot$(Holmberg et al., 2007, see the electronic table on VizieR) and it has been classified as F2III-IV (Rhee et al., 2007), implying it was an A type star during main sequence and has evolved – here we will present updated mass and luminosity estimates (see Section 2.6). The rotational velocity has been reported between $v \sin i\ = 69$ km s^{-1} (Glebocki & Stawikowski, 2000) and 82 km s^{-1} (Bernacca & Perinotto, 1970) in the literature, although recent measurements are more consistently confined from 69 km s^{-1} to 71 km s^{-1} (Glebocki & Stawikowski, 2000; Reiners, 2006; Rachford & Foight, 2009; Schröder et al., 2009) which we prefer to use for this study. Previous studies measured its apparent effective temperature range from 6877 K to 7200 K (Gray et al., 2001; Daszyńska & Cugier, 2003; Rhee et al., 2007; Rachford & Foight, 2009) and estimated its radius from 3.43 $R_\odot$ to 3.69 $R_\odot$(Richichi & Percheron, 2002; Daszyńska & Cugier, 2003; Rachford & Foight, 2009).

2.5.2   Observations

β Cas was observed for 7 nights in 2007 and 2009 by CHARA/MIRC. The observation log is presented in Table 2.1 and the calibrators in Table 2.2. The UT 2009Oct22 observations used Photometric Channels (Appendix A) for data calibration. The (u,v) coverage of all the observations is shown in Figure 2.6.

2.5.3   Modal Fitted Results

We adopted the following basic properties of β Cas from the literature as inputs: distance = 16.8 pc (van Leeuwen, 2007) and metallicity [Fe/H] = 0.03 (Gray et al., 2001). We take [Fe/H] = 0 which is the closest value to the observation to extract intensities from Kurucz model. M = 2.09 $M_\odot$ (Holmberg et al., 2007, see the electronic table on VizieR) is adopted for the first attempt of the model fitting. The fitting
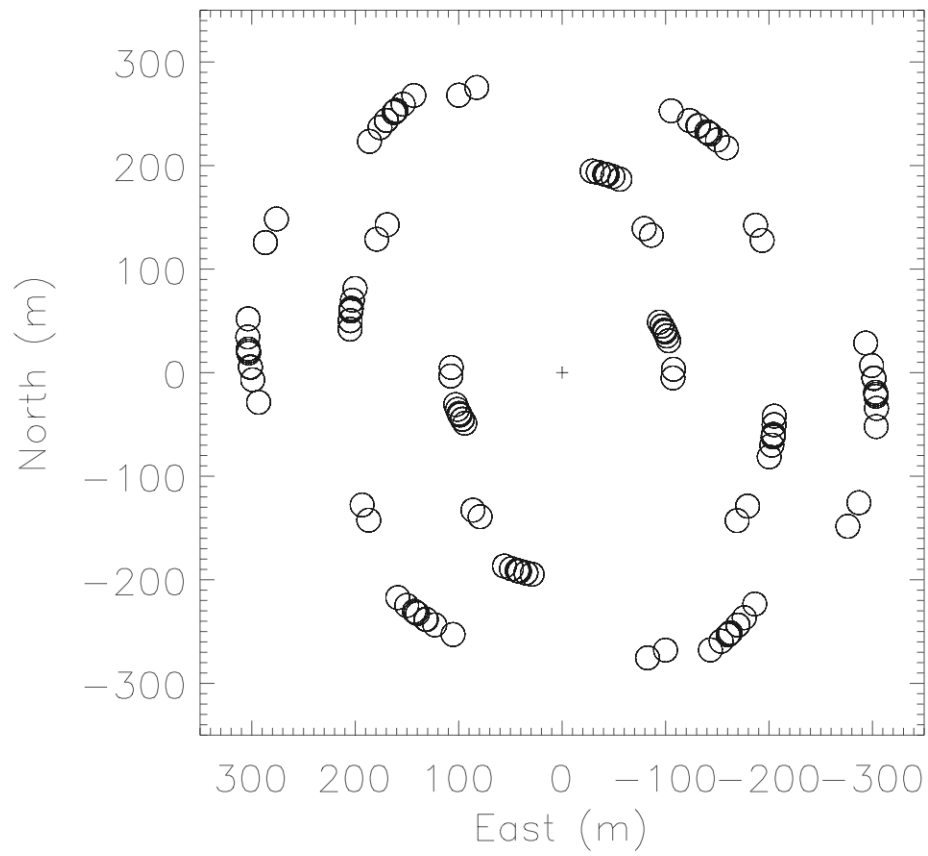
Figure 2.6. (u,v) coverage of β Cas for 7 nights of observations by CHARA/MIRC (Che et al., 2011).

results and final parameters from the modified von Zeipel model are shown in Figure 2.7 and the middle column of Table 2.4 respectively. The results show that β Cas is rotating more than 90% of its critical rate, which causes its radius to be $\sim 24\%$ longer at the equator than at the poles. The temperature at the pole is about $1000\,\mathrm{K}$ higher than that at the equator. These significant differences between the poles and equator imply that the L_{app} and $T_{\mathrm{app}}^{\mathrm{eff}}$ are highly dependent on viewing angles. The best model mass estimation of its non-rotating equivalent from L-R_{pol} and HR diagrams is $1.91\,\mathrm{M}_\odot$ (Figure 2.11), lower than $2.09\,\mathrm{M}_\odot$ from Holmberg et al. (2007). The oblateness mass estimation from a $v \sin i$ range 69 $\mathrm{km\ s}^{-1}$ to 71 $\mathrm{km\ s}^{-1}$ is $1.77^{+0.17}_{-0.05}\,\mathrm{M}_\odot$, which is consistent with our model mass within the error bars. Our $\beta = 0.146$ from the modified von Zeipel model fitting is significantly different from standard values for either radiation-dominated or convection-dominated envelopes. The inclination angle is low, implying we are looking at more of the polar area than the equatorial area as shown in Figure 2.9. This is why the apparent luminosity L_{app} is higher than L_{bol} .

Claret (2000) has computed the evolution of gravity darkening coefficients for different stellar masses, and showed that at such low T_{eff} β Cas should be convection-dominated in the envelope. Fixing gravity darkening coefficient $\beta = 0.08$ (Lucy model) for convective envelopes, we run model fitting again and the results are shown in the right column of Table 2.4. The best fitting χ^2s for this model is much worse, nearly a factor of 2 higher. Many parameters from the Lucy model are similar to those from the modified von Zeipel model, except the temperature at the equator. This is not surprising because the low β value means the weak dependence of the temperature on gravity, namely the temperature at the equator will be closer to that at the poles for the Lucy model. Consequently the luminosities L_{app} and L_{bol} and temperature $T_{\mathrm{app}}^{\mathrm{eff}}$ are a little higher than those from the modified von Zeipel model. The modified von Zeipel model gives significantly lower χ^2 than the Lucy model, especially that from the closure phase data which is sensitive to asymmetric structures on the stellar surface. This implies the modified von Zeipel model describes the surface temperature distribution better, ruling out the Lucy model in this case. This is also confirmed
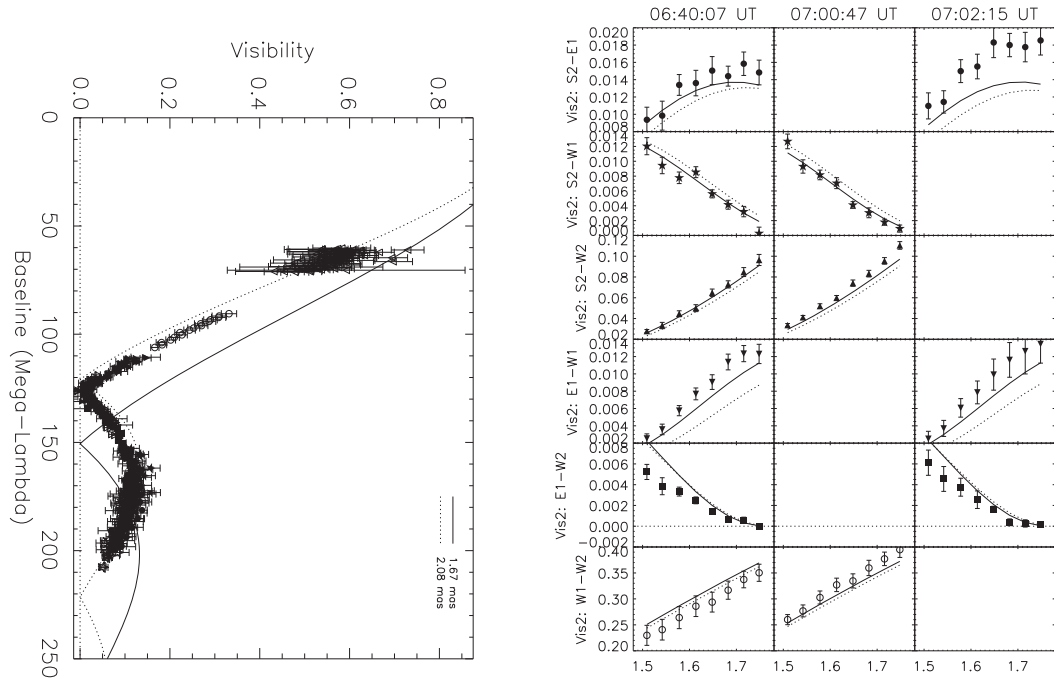
(a)

(b)
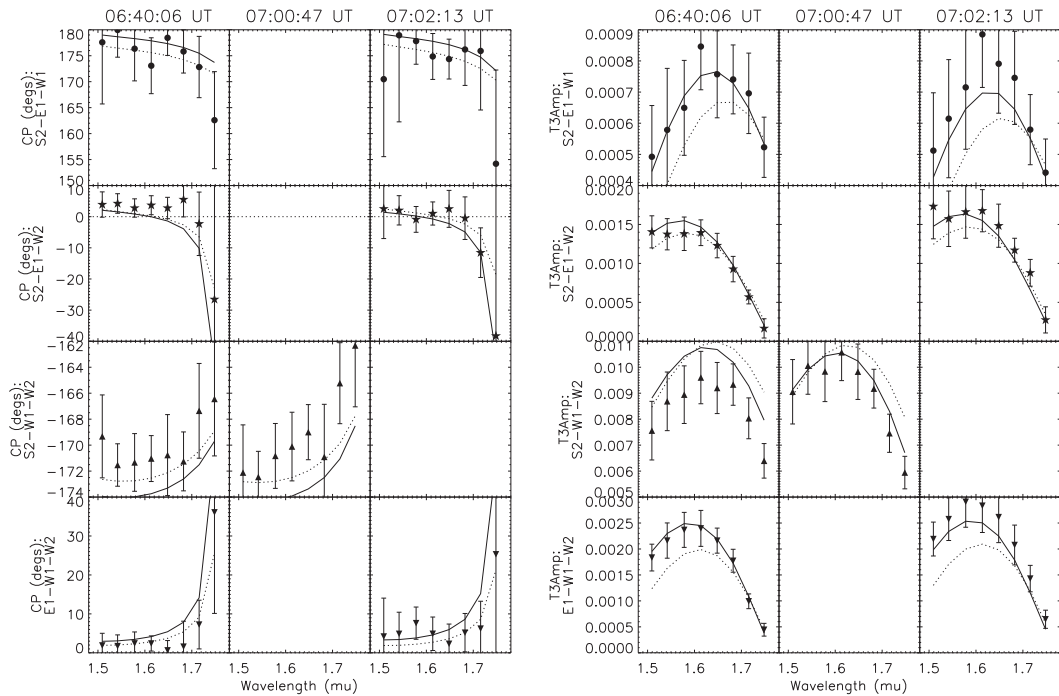
(c)

(d)

Figure 2.7. Similar panels of β Cas as those of α Leo in Figure 2.3. The reduced χ^2 of model is 1.36 and that of image is 1.20. All the panels are reprinted from Che et al. (2011).

Model Parameters	Modified von Zeipel model (β-free)	Lucy model ($\beta = 0.08$)
Inclination (degs)	$19.9^{+1.9}_{-1.9}$	$21.4^{+3.1}_{-0.9}$
Position Angle (degs)	$-7.09^{+2.24}_{-2.40}$	$-1.8^{+0.8}_{-1.7}$
T_{pol} (K)	7208^{+42}_{-24}	7108^{+14}_{-18}
R_{pol} (mas)	$0.849^{+0.023}_{-0.020}$	$0.835^{+0.035}_{-0.010}$
$\omega \, / \, \omega_{\mathrm{crit}}$	$0.920^{+0.024}_{-0.034}$	$0.930^{0.011}_{-0.050}$
β	$0.146^{+0.013}_{-0.007}$	0.08 (fixed)
Derived Physical Parameters		
T_{eq} (K)	6167^{+36}_{-21}	6487^{+12}_{-17}
R_{eq} ($R_{\odot}$)	$3.79^{+0.10}_{-0.09}$	$3.77^{+0.16}_{-0.04}$
R_{pol} ($R_{\odot}$)	$3.06^{+0.08}_{-0.07}$	$3.01^{+0.13}_{-0.04}$
Bolometric luminosity L_{bol} ($L_{\odot}$)	$21.3^{+1.0}_{-0.7}$	$22.7^{+1.4}_{-0.3}$
Apparent effective temperature $T^{\mathrm{eff}}_{\mathrm{app}}$ (K)	6825	6897
Apparent luminosity L_{app} ($L_{\odot}$)	27.3	28.3
Model $v \sin i$ (km s^{-1})[a]	$72.4^{+1.5}_{-3.5}$	$79.8^{+0.9}_{-1.0}$
Rotation rate (rot/day)	$1.12^{+0.03}_{-0.04}$	$1.16^{+0.01}_{-0.06}$
Model mass ($M_{\odot}$)[b]	1.91 ± 0.02	1.95 ± 0.03
Oblateness mass ($M_{\odot}$) [c]	$1.77^{+0.17}_{-0.05}$	$1.45^{+0.12}_{-0.27}$
Age (Gyrs)[b]	1.18 ± 0.05	1.09 ± 0.03
Model V Magnitude[d]	$2.284^{+0.012}_{-0.019}$	$2.251^{+0.020}_{-0.006}$
Model H Magnitude[d]	$1.398^{+0.007}_{-0.007}$	$1.394^{+0.010}_{-0.001}$
χ^2 of various data		
Total χ^2_{ν}	1.36	2.53
Vis^2 χ^2_{ν}	1.26	1.56
CP χ^2_{ν}	2.18	4.81
T3amp χ^2_{ν}	0.45	0.60
Physical Parameters from the literature		
[Fe/H][e]	0.03	
Distance (pc)[f]	16.8	

[a] Observed $v \sin i$ = 69 km s^{-1} to 71 km s^{-1} (Glebocki & Stawikowski, 2000; Reiners, 2006; Rachford & Foight, 2009; Schröder et al., 2009)

[b] Based on the Y^2 stellar evolution model (Yi et al., 2001, 2003; Demarque et al., 2004)

[c] Zhao et al. (2009)

[d] Vmag $= 2.27 \pm 0.01$, (Morel & Magnenat, 1978, with arbitrary error), Hmag $= 1.584 \pm 0.174$ (Cutri et al., 2003), 1.43 ± 0.05 (Ducati, 2002)

[e] Gray et al. (2001)

[f] van Leeuwen (2007)

Table 2.4. Best-fit and physical parameters of β Cas

by comparing the model $v \sin i$ with the observed values: $v \sin i = 72.4^{+1.5}_{-3.5}$ km s^{-1} from the modified von Zeipel model agrees with the observation 69 km s^{-1} to 71 km s^{-1}, while from the Lucy model $v \sin i = 81.3^{+0.9}_{-1.0}$ km s^{-1} deviates strongly from the observation. Further more, the oblateness mass and model mass don't agree with each other, suggesting that the Lucy model is not self-consistent in this case.

We found that the low inclination angle induces strong degeneracies between some parameters during the model fitting. For example when a star is pole-on the darkness at the equator could be due to either the high angular velocity or the high gravitational darkening coefficient since the oblateness can not be directly constrained from this viewing angle. The left panel of Figure 2.8 shows the degeneracy between β and the inclination. The contour represents the 68.3% probability level, and is weakly elongated in one direction. We further overplot onto the probability space the observed $v \sin i$ range which intersects the contour. This means a precise $v \sin i$ measurement would significantly constrain the stellar parameters from our model fitting. The same idea is applied to the probability space of β and $\omega / \omega_{\mathrm{crit}}$ (Figure 2.8 right) which shows a stronger correlation between these two parameters.

2.5.4 Imaging

The left panel of Figure 2.9 shows the reconstructed image of β Cas . The reduced χ^2 of the image is 1.20, comparable to our best-fit models. We overplot longitudes and latitudes with solid lines from the model and include contours of surface brightness temperatures with dashed lines. The right panel shows the image from the model fitting, overplotted with the surface brightness temperature contours from the model. Because of the inclination angle, the surface brightness temperature contours do not coincide with latitude contours. We find that the two images are consistent with each other in general. The images show a center bright region which is one pole of β Cas . The surface brightness drops gradually towards the edge due to gravity darkening. One may also notice limb-darkening at the edge of the stellar image.
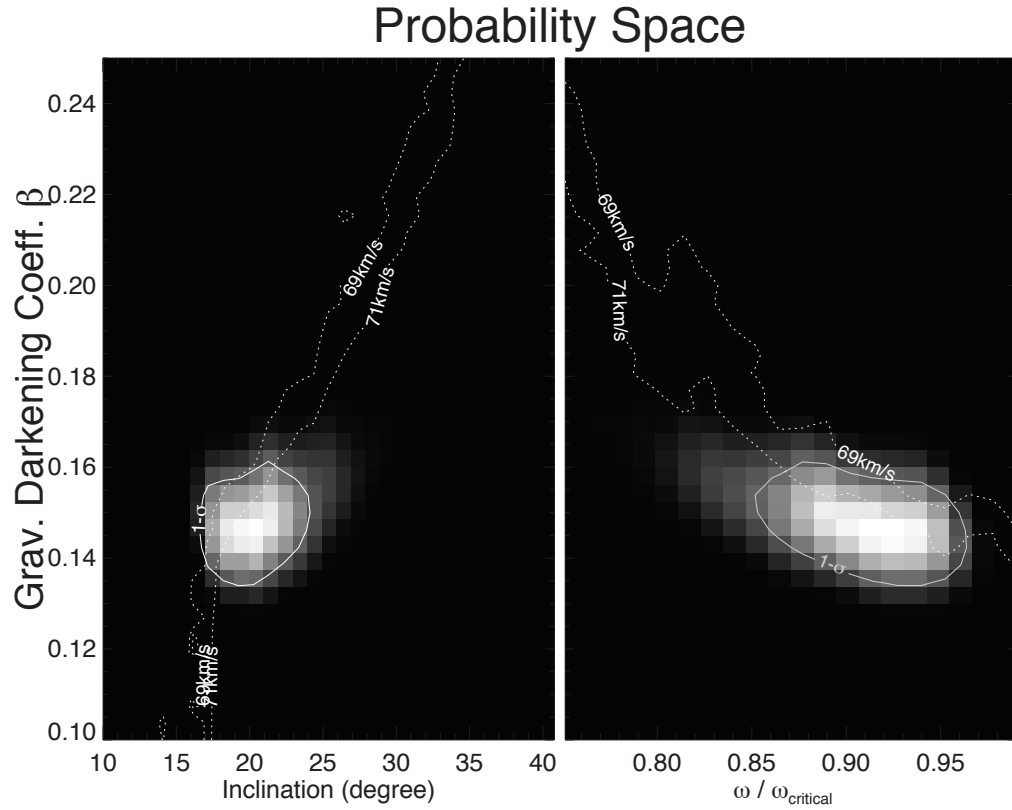
Figure 2.8. Probability spaces of β Cas show the degeneracy between stellar parameters. All the notations are the same as in the probability spaces of α Leo (see Figure 2.4). The $v \sin i$ value range 69 km s^{-1} to 71 km s^{-1} is adopted from the literature, and the corresponding lines intersect the 1-σ contours. Both panels show the elongation of the contours, which imply some degeneracies between these parameters. Both panels are reprinted from Che et al. (2011).
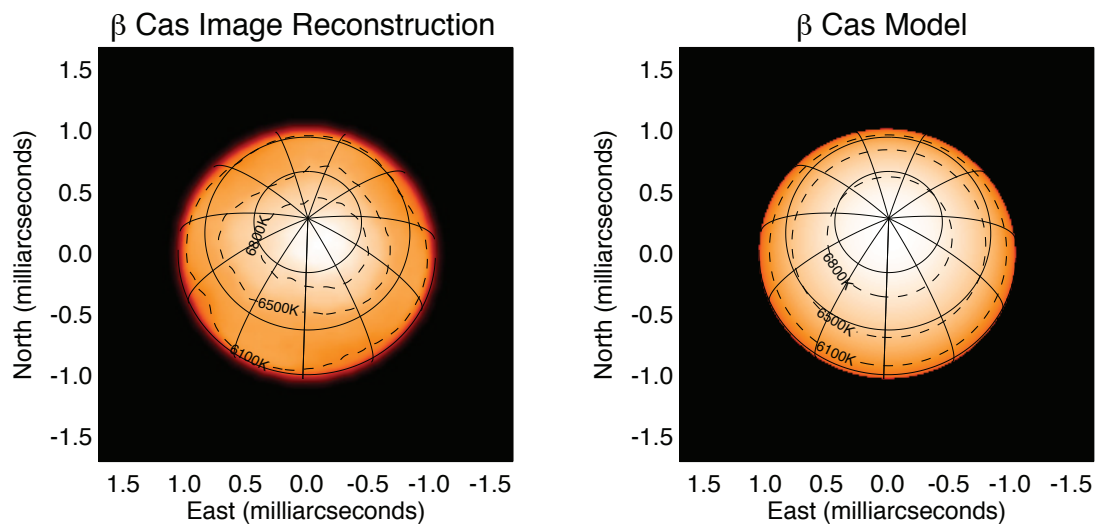
Figure 2.9. Images of β Cas . The notations are all the same as those in images of α Leo (see Figure 2.5). The angular resolution is 0.57mas. The reduced χ^2 of the images from MACIM and model fitting are 1.20 and 1.36. Both images are reprinted from Che et al. (2011).

2.6 Stellar Evolution Tracks of Rapid Rotators

One interesting topic for rapidly rotating stars is to locate their positions on the Hertzsprung-Russell (HR) diagram and compare with stellar models. While traditional HR diagrams for non-rotating stars have been available for a long time, the analogue for rotating stars have just been built (Ekström et al., 2012) very recently, which is later than the time this work was published. Applications of evolutionary models for rotating stars to interferometric studies of rapid rotators can be found in Monnier et al. (2012).

However for this work, we used a traditional HR diagram for analysis. This contains two issues. First, traditional photometric observations only see the apparent luminosities L_{app} and apparent effective temperatures $T_{\mathrm{app}}^{\mathrm{eff}}$ which depend on stellar inclination angles; the bolometric luminosities L_{bol} of rapid rotators are hidden from the observers. Interferometric observations allow us to construct 2-D surface models of stars, thus to obtain the L_{bol} (Zhao et al., 2009). We obtain the gravity and temperature distributions across the stellar surface from the model fitting. From Kurucz models, we are able to retrieve intensities from each patch of stellar surface, and then integrate the radiation all over the star to obtain the bolometric luminosity L_{bol} [2]. By comparison we also compute an inclination curve which shows stellar L_{app} and $T_{\mathrm{app}}^{\mathrm{eff}}$ as a function of the inclination angle, and we can mark the one corresponding to its inclination from the model fitting. The L_{app} can be calculated by $L_{\mathrm{app}} = 4\pi d^2 F_{\mathrm{bol}}$, where d is the distance and F_{bol} is the bolometric flux computed by integrating flux from each grid over the projected area. Then the $T_{\mathrm{app}}^{\mathrm{eff}}$ is obtained by $\sigma(T_{\mathrm{app}}^{\mathrm{eff}})^4 = \pi d^2 F_{\mathrm{bol}}/A_{\mathrm{proj}}$, where A_{proj} is the projected area.

Since typical HR diagrams are constructed for non-rotating stars, it is inappropriate to place a rapid rotating star on such diagrams. A rapidly rotating star shows a little lower L_{bol} than L_{nr} from its non-rotating equivalent (an imaginary spherical star which a rapid rotator would turn out to be if it spins down to no angular velocity),

---

[2]The "overall effective temperature" $T_{\mathrm{bol}}^{\mathrm{eff}}$ can be estimated from the L_{bol} divided by the total surface area; However, in the case of a rapid rotator, this overall effective temperature is just a definition with limited physical meaning, so it is not used to infer the masses or ages of stars.

meaning a rotating star will appear as a lower mass star on HR diagram. Therefore the interpreted mass and age from the rotating star deviates from the true values. To partially solve this problem, one has to convert the properties of a rapidly rotating star to its non-rotating equivalent. Studies have shown that the bolometric luminosity and polar radius do not change much as a star spins up. Following this, we alter the traditional HR diagram to a new one with axes of bolometric luminosity and polar radius (L-R_{pol} diagram), and locate rotating stars on the new diagram to infer the mass and age (Peterson et al., 2006, private communication, 2010). To compare with the astronomy-friendly HR diagrams, one can also translate these two values of non-rotating equivalents into L_{nr} and $T_{\mathrm{nr}}^{\mathrm{eff}}$.

The left panels of Figure 2.10 and 2.11 show α Leo and β Cas on L-R_{pol} diagrams from Y^2 model (Yi et al., 2001, 2003; Demarque et al., 2004). The cross and square symbols represent the bolometric luminosity and polar radius before and after the rotational correction respectively (Sackmann, 1970). The corrections are trivial: L_{nr} and $\mathrm{R}_{\mathrm{pol,nr}}$ decrease by 5.5% and 1.3% respectively for a 2 solar mass star as it spins up to close to critical speed. So on L-R_{pol} diagrams one may even directly use L_{bol} and $\mathrm{R}_{\mathrm{pol}}$ of a rotating star for rough estimates of its mass and age. We have begun work on a more exact formulation using a new grid of rotating models, but this is the subject of future detailed studies.

The traditional HR diagrams are shown in the right panels of Figure 2.10 and 2.11. The solid lines are the inclination curves, which show the L_{app} and $T_{\mathrm{app}}^{\mathrm{eff}}$ as a function of inclination angles. The star symbols on the curve represent the estimated inclination angles. The square symbols stand for L_{nr} and $T_{\mathrm{nr}}^{\mathrm{eff}}$ of the non-rotating equivalent. The position of non-rotating equivalent on HR diagram deviates severely from the position of the rapidly rotating equivalent based on its apparent values. For instance, Regulus would be about 0.08 Gyr older and 0.5 M$_{\odot}$less massive from its L_{app} and $T_{\mathrm{app}}^{\mathrm{eff}}$ than from L_{nr} and $T_{\mathrm{nr}}^{\mathrm{eff}}$. So we strongly recommend to correct for the effects of rotation when placing a rapidly rotating star on HR diagram. Zhao et al. (2009) didn't adopt this correction, which may lead to an additional error in determining age and mass of rapidly rotating stars.
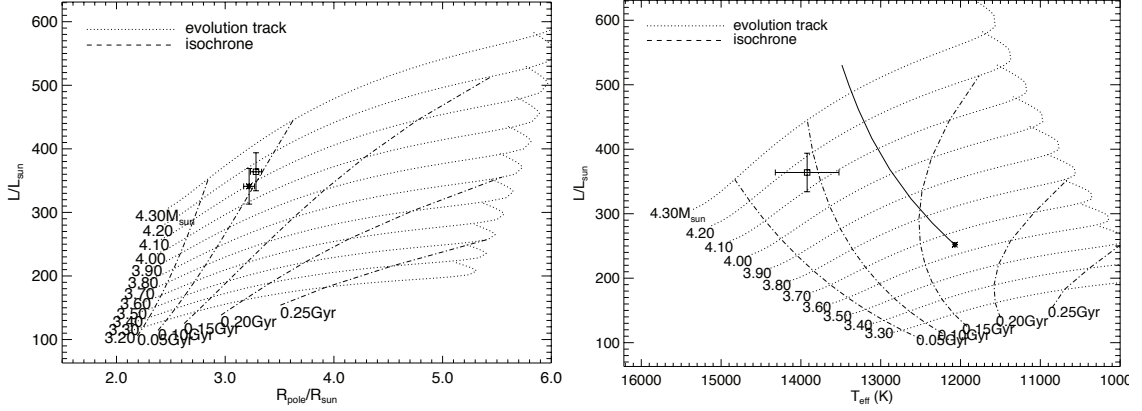
Figure 2.10. α Leo positions on L-R_{pol} (left) and Hertzsprung-Russell (right) diagrams based on Y^2 model (Yi et al., 2001, 2003; Demarque et al., 2004). In the left panel, the cross symbol with error bar stands for the rapidly rotating α Leo based on its L_{bol} and polar radius from modified von Zeipel model fitting. The square symbol with error bar is the non-rotating equivalent of α Leo , the corrections of L_{bol} and polar radius because of rotation is adopted from Sackmann (1970). In the right panel, the solid line is the inclination curve, which shows how L_{app} and $T_{\mathrm{app}}^{\mathrm{eff}}$ change as a function of inclination angles. The star symbol is α Leo with its estimated inclination angle. The meaning of the square symbol is the same as in the left panel. Both images are reprinted from Che et al. (2011).

2.7 Rotation Coupling Between Stellar Core and Envelope

Measuring ω / ω_{crit} as a function of age provides a way of studying the coupling between the stellar core and envelope in terms of angular momentum. As a star evolves along the main sequence, the core contracts and spins up due to the conservation of the angular momentum, while the spherical-shell envelope expands and spins down. ω_{crit} also drops as the star expands. Given the initial rotational conditions and the evolution of stellar inner structure, the evolution of ω / ω_{crit} depends only on how much the core and envelope are coupled. In the case when the core and envelope are not coupled, the angular velocity of the envelope changes roughly proportional to R^{-2}. The critical angular velocity ω_{crit} is proportional to $R^{-1.5}$. So ω / ω_{crit} decreases roughly as $R^{-0.5}$ as a star expands. While in the other extreme case of solid body rotation, namely the core and envelope are fully coupled, the core transfers the most angular momentum to the envelope, and ω / ω_{crit} may increase as a star expands. We can also predict its value in the past, knowing the current ω / ω_{crit}.

One critical component in the discussion above is the evolutionary model of stellar
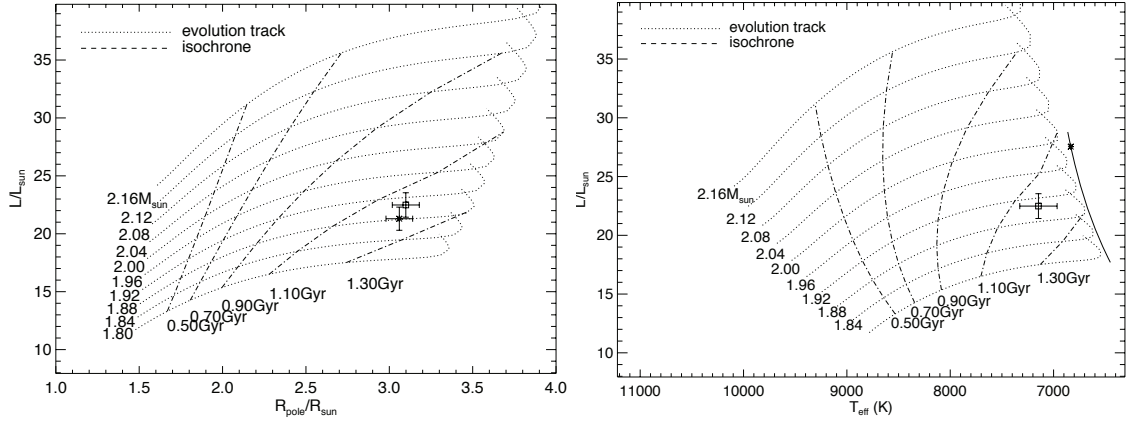
Figure 2.11. β Cas position on $L\text{-}R_{\rm pol}$ and HR diagrams based on Y^2 model. The notations are the same as those on diagrams of α Leo (see Figure 2.10). Both images are reprinted from Che et al. (2011).

inner structure. As mentioned above, by the time this work was submitted, no general evolutionary models for rotating stars existed. Therefore we used an evolutionary model for non-rotating stars for analysis. We assume that a non-rotating stellar model is a good approximation for calculating evolution of internal density profiles because rotation has very little effect on iso-potential surfaces inside the star. For instance, for a rapidly rotating star with $\omega\,/\,\omega_{\rm crit} = 0.9$, its equatorial radius is elongated by only 21.6%, but gravity quickly dominates as one looks deep into the star. This means $\omega_{\rm crit}$ is much larger than angular velocity at certain radius and smaller, and the structure can again be approximately described by a non-rotating stellar model. So in the following calculation we adopt a non-rotating stellar model[3]

By computing how the moment of inertia changes with time, we are able to calculate the evolution of $\omega\,/\,\omega_{\rm crit}$ for a $1.9\,\mathrm{M}_\odot$ non-rotating star (Figure 2.12). In the left panel, all the values are normalized to their initial values. The solid line shows the evolution of the stellar radius, the dotted and dashed lines show the evolution of the ratio $\omega\,/\,\omega_{\rm crit}$ when the core and envelope are fully coupled and uncoupled. When the core and envelope are uncoupled, the ratio drops as the star expands as

---

[3]EZ-Web http://www.astro.wisc.edu/~townsend/static.php?ref=ez-web is a web-browser interface to the EZ evolution code (Paxton, 2004), developed and maintained by Rich Townsend.

expected. When the core and envelope are fully coupled, the ratio actually increases a little due to the transference of angular momentum from the core to the envelope. This result may explain high ω / ω_{crit} value of β Cas .
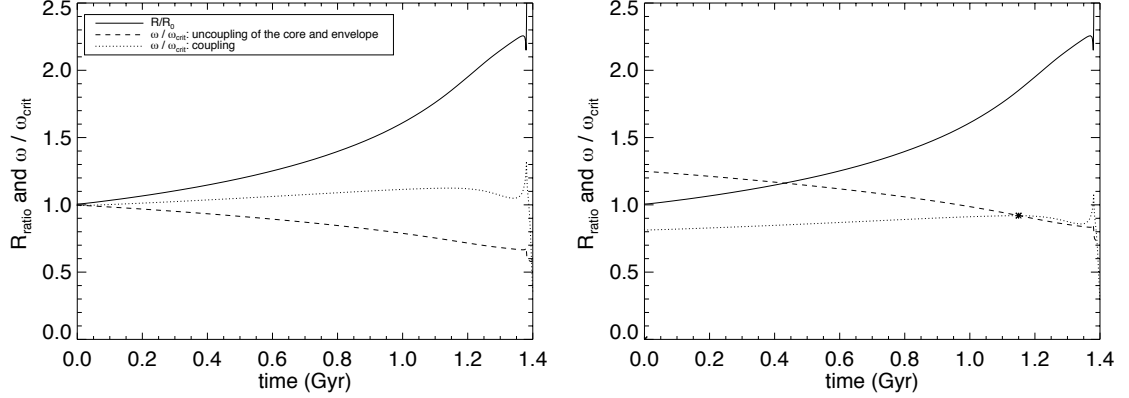
Figure 2.12. The evolution of stellar rotation. The model is adopted from the evolution of a 1.90 $M_{\odot}$ non-rotating star (Paxton, 2004, the web-browser interface is developed and maintained by Rich Townsend). The left panel: solid line is the ratio of the stellar radius to its value at the beginning of main sequence; dashed line is the ratio of ω / ω_{crit} (ω is angular velocity; ω_{crit} is the critical angular velocity when the centrifugal force balances the gravity at the equator) to its initial value when the core and envelope are not coupled; dotted line is the ratio when they are totally coupled. The right panel: using the current ω / ω_{crit} value (represented by asterisk) from model fitting, track back to its previous values assuming uncoupling and total coupling of the core and envelope. Both images are reprinted from Che et al. (2011).

In the right panel, we use the ratio ω / ω_{crit} = 0.92 from model fitting as the current value of β Cas , and trace back to its previous values in the extreme cases of full-coupling and no coupling. We notice that if the core and envelope are not well-coupled (dashed line), the ratio will exceed the unit in the past, which is not allowed. On the other hand if they are totally coupled (dotted line), the ratio value remains below 1. Reading off the panel, ω / ω_{crit} changes more rapidly in the past $\sim$ 0.5 Gyr if the core and envelope are not coupled. These results suggest that during the stellar evolution of β Cas , the angular momentum is efficiently transferred from the core to the envelope in the past 500 Myr. These results seem to confirm earlier findings by Danziger & Faber (1972) based on analysis of $v \, sin \, i$ statistics.

60

2.8 Gravity Darkening

Von Zeipel introduced the idea of gravity darkening in 1924 and predicted the standard value of β to be 0.25 for stars with fully radiative envelopes. Our group has studied five rapid rotators (α Aql, α Cep, α Oph, α Leo, β Cas) up to now, four of them show non-standard Gravity darkening coefficient (β) values from the modified von Zeipel model fitting. α Oph was only fitted with β-fixed model because of the high degeneracy between gravity darkening coefficient and rotational speed due to its almost equator-on orientation (Zhao et al., 2009).

In Figure 2.13 we plot the results of β versus temperature for the four targets with their gravity darkening coefficients obtained from the modified von Zeipel model fitting. The shadow areas show the temperature ranges from the pole to equator and the 1-σ uncertainties of β from the model fitting for each star. For comparison, we also plot the solid line representing the predicted relation between β and temperature adopted from Claret (2000). We digitize the evolution plot of a 2 solar mass star in Claret (2000) paper and extend β to high temperature 14500 K with β fixed to 0.25. We should point out that the predicted relation shifts a little to lower temperature for stars with higher masses, but it is not a big issue in our case. For α Cep, α Aql and β Cas, their masses are close to 2 $M_\odot$, so they can share the same relation. α Leo is much more massive than 2 $M_\odot$, the predicted curve shifts to low temperature a little (less than 1000K).

Figure 2.13 shows that α Cep, α Aql and β Cas partially intercept the transition area of the predicted curve, meaning that the equatorial regions might start to show convection. In our model fitting, we use a single β to describe the relation between the gravity and temperature, instead of letting β change as a function of temperature. This may partially explain why these three stars have non-standard β values, because their poles could be radiation-dominated while the equators convection-dominated, the resulting β may be some weighted values across the stellar surfaces. However the analysis here is non-physical, a detailed stellar model that includes radiation and convection in a rapidly rotating star is required to fully understand the gravity
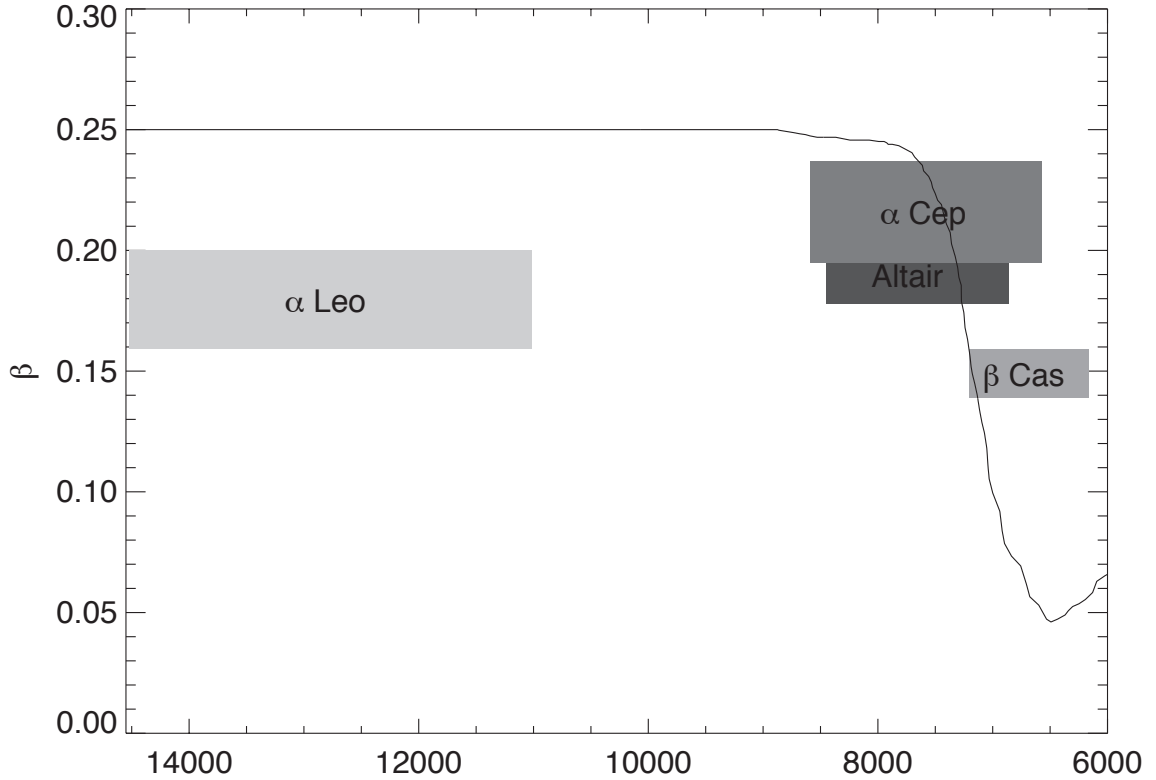
Figure 2.13. Gravity darkening coefficient (β) vs. temperature for four targets our group has studied (reprinted from Che et al., 2011). The solid line represents the theoretical relation between the gravity darkening coefficient β and effective temperature, adopted from the evolution of a non-rotating 2 solar mass star (Claret, 2000). The curve is extended to higher temperature for comparison with α Leo . The temperature range of each star contains temperature from the poles to equator. The β range indicates the uncertainty from the model fitting.

darkening law of these stars with intermediate temperatures.

However α Leo has such high temperature range that even the equator is supposed to be fully radiative theoretically. So the poles and equator will share the same $\beta = 0.25$, justifying the standard von Zeipel model in this case. But our result still prefers non-standard $\beta = 0.188^{+0.012}_{-0.029}$. One possible explanation is that even at such high temperature, the envelope is not fully radiative. Tassoul (2000) concludes that solid-body rotation is impossible for a pseudo-barotrope in static radiative equilibrium. The solid-body rotation will disrupt the constancy of the temperature and pressure over the stellar surface, and cause the temperature and pressure gradients between the equator and poles. The gradients will induce a flow of matter which forms a

permanent meridional circulation and break down the strict radiative equilibrium. The matter flow may further lead to the failure of our model assumption: solid-body rotation. The material from higher latitudes carries less angular momentum than those from lower latitudes. The meridional flows moving towards higher or lower latitudes will speed up or slow down the rotational speed of local material on their way, which triggers differential rotation. In fact the standard von Zeipel's law may only be valid for slow rotators (Espinosa Lara & Rieutord, 2011) where the difference of temperature and effective gravity across latitudes is trivial so that the assumption of solid body rotation and radiative envelope are still valid.

Another study from Lovekin et al. (2006) compares the effective temperature distribution across the surface of a 6.5 $M_\odot$ solid-body rotator between a stellar evolution model with rotation (ROTORC) and von Zeipel's law, and finds that the temperature distribution is shallower in the model which is consistent with lower β value we obtained from α Leo . A few observations on W UMa systems (Kitamura & Nakamura, 1988; Pantazis & Niarchos, 1998) roughly confirm von Zeipel's law, but with very large scatter. The material flows on the surfaces of these stars are less complicated due to an important feature of the binary systems: the stars are tidally locked by their companions. Hence the stellar differential rotations are effectively depressed and the resulting solid-body rotations are well regulated. Therefore these stars may maintain radiation-dominated envelopes which validate the standard von Zeipel model.

Based on the similar β values found for all our objects and for α Leo in particular, we recommend researchers adopt a new standard β=0.19 for future modeling of rapid rotating stars with radiative envelopes.

2.9   Conclusion

We have studied two rapid rotators with extreme spectral type: β Cas and α Leo observed by CHARA-MIRC. By fitting the modified von Zeipel model, namely the solid-body rotation model with free-β gravity darkening law, to observed infrared interferometry data and V and H photometric fluxes, we find both stars are rotating at close to critical speed: ω / $\omega_{\rm crit}$= 0.92 and 0.96. The fast rotations elongate

their equators by 24% and 30% compared with their poles, and their equatorial temperatures are 1000K and 3000K cooler than their polar values. We estimated the mass of α Leo to be 4.15 ± 0.06 $M_\odot$ from both L-R_{pol} and HR diagrams corrected for rotational effect, and it is higher than 3.4 ± 0.2 $M_\odot$ found by McAlister et al. (2005). We have also reconstructed aperture synthesis images using MACIM. The images are consistent with the temperature distribution from the fitted models.

We discussed the evolution of ω / ω_{crit}. The ratio could increase or decrease depending on how much stellar cores and envelopes are coupled. In the case of fully coupling, ω / ω_{crit} increases a little during main sequence and sub-giant branch due to the angular momentum transferred from the core to the envelope. Our study on β Cas, which is about 1.18 Gyrold but still rotating at 92% of its critical speed, suggests the core and envelope are well coupled during the evolution.

All our targets from the modified von Zeipel model fitting prefer the non-standard gravity darkening coefficients, especially in the case of α Leo whose envelope should be fully radiative because of the high surface temperature range 11010K - 14520K. One possible reason is that solid-body rotation breaks down the constancy of temperature and pressure on the stellar surface and induces meridional flow, which violates strict radiative equilibrium. Furthermore the meridional flow may result in differential rotation which causes the failure of our solid-body rotation assumption. Until better models are created, we recommend using the empirically-determined gravity-darkening coefficient $\beta = 0.19$ for rapidly-rotating stars with radiative envelopes.

CHAPTER 3

Be Binary System: δ Sco

The work of this chapter has been published (Che et al., 2012b), much of the content has been extracted from the paper.

3.1 Background

δ Scorpii (hereafter δ Sco) is a Be binary system with a high-eccentricity (e $\sim$ 0.94) orbit and a period of 10.74 years (Tycner et al., 2011). The binary nature was discovered with speckle interferometry by Labeyrie et al. (1974) near maximum separation. It is at a distance of 150^{+24}_{-17} pc (van Leeuwen, 2007). The primary of the system is a B0.5V star with a gaseous disk and the secondary is a B2V star (Bedding, 1993; Tango et al., 2009). The orbital parameters of δ Sco have been revisited by several groups (e.g. Mason et al., 2009; Tango et al., 2009; Tycner et al., 2011). Tycner et al. (2011) combined radial velocity measurements from Miroshnichenko et al. (2001) with interferometric observation obtained with Navy Precision Optical Interferometer (NPOI), and predicted the recent periastron on UT 2011 July 06 $\pm$ 2days.

It provides a unique opportunity to study active disk formation. The system did not show clear evidence of Be phenomena until the periastron in 2000. The brightness increased by 0.4 mag (Otero et al., 2001) in the visible, and strong Hα emission was detected by spectroscopic observations (Fabregat et al., 2000) during the 2000 periastron. The following spectroscopic and photometric observations confirmed the gradually increasing strength of Hα emission, which implied a developing circumstellar disk (Miroshnichenko et al., 2003; Gandet et al., 2002). The fact that it took 2

years for δ Sco to reach its optical maximum is not typical, because it took decades for other active Be disks to reach their highest optical brightness (Bjorkman et al., 2002; Telting et al., 1993). The disk started to fade in 2005 in both optical and infrared, while the Hα equivalent width (EW) was rising (Carciofi et al., 2006). The visible brightness of the system increased again in 2010[1] , one year before the predicted periastron.

A number of observations were carried out on δ Sco coordinated with the periastron passage of the system which was anticipated at the beginning of July 2011. This provided another opportunity to study the gaseous disk and how it responded to the increased gravitational disturbance. Possible physics behind the 2000 periastron activity was that when the effective surface gravity of the primary along the connecting line to the secondary was reduced, the rotation could become locally supercritical, releasing material into orbit (Harmanec et al., 2002). One of the goals of this work is to test if this scenario happened again in the 2011 periastron. The data used in this work are from an infrared and a visible interferometer. We carried out 7 nights of H band interferometry observations on δ Sco about one week after the predicted periastron to study the disk properties, and 128 nights in total of visible interferometer observations from 2000 to 2011 periastron to refine the binary orbital parameters.

The main goal of the work is to verify if the disk grows during the secondary passage by quantifying the disk asymmetry after periastron. The gravity disturbance of the secondary due to tidal forces should make it easier for the primary to lose mass and this extra mass might be ejected asymmetrically. Thus our observations could shed light on the Be disk formation mechanism. With excellent (u,v) plane coverage in the interferometry data, we are also able to constrain and discuss other properties of the binary system, such as inclination angles of the disk plane and orbital plane.

———————————————————

[1]$http://varsao.com.ar/delta\_Sco.htm$

UT Date	Telescopes	Calibrators
2011Jul10	S1-S2-E2-W1-W2	58 Oph, HD 160042
2011Jul11	S1-S2-E2-W1-W2	58 Oph
2011Jul13	S1-S2-E2-W1-W2	53 Ser, 58 Oph
2011Jul16	S1-S2-E2-W1	58 Oph
2011Jul17	S1-S2-E2-W1-W2	53 Ser, 58 Oph
2011Jul20	S1-S2-E2-W1-W2	58 Oph
2011Jul22	S1-S2-E2-W1-W2	58 Oph

Table 3.1. CHARA/MIRC observation logs of δ Sco

3.2 Observations

3.2.1 CHARA/MIRC Interferometry

The observations of δ Sco were carried out at CHARA/MIRC, taking advantage of the upgraded of 6-beam MIRC (Appendix B) and the second version of Photometric Channels (Appendix A) . The enormously boosted (u,v) plane coverage and improved data quality not only allow MIRC to image more complex objects such as spotted stars, but also increases the MIRC sensitivity to reach fainter objects. MIRC sensitivity was limited by the visibility calibration due to the uncertainty of the real time flux measurements of each beam. The uncertainty is reduced with the new version of PCs, which allows weaker MIRC visibilities to be well calibrated. We also re-aligned the polarization of some fibers to provide better instrumental fringe contrast.

We observed δ Sco on 7 nights (Table 3.1) in July 2011 just after periastron with the upgraded MIRC. We used three calibrators and calculated their uniform disk sizes to be: 58 Oph = 0.705±0.04 mas ; HD160042 = 0.65±0.05 mas ; 53 Ser = 0.45±0.03 mas (Kervella & Fouqué, 2008; Barnes et al., 1978; Bonneau et al., 2006). A typical (u,v) plane coverage of one night of δ Sco observation is shown in Figure 3.1. The data were reduced using the MIRC data pipeline (Monnier et al., 2007). In addition to the random error that is estimated in our pipeline, we must include errors associated with calibration of the changing transfer function. Based on a study of calibrators, we have adopted the following procedure. First, we apply a multiplication of 1.5 to the errors of visibilities squared and triple amplitudes. Next, we insist that the visibility squared errors are never below 0.1 × visibilities squared or .001, whichever

67
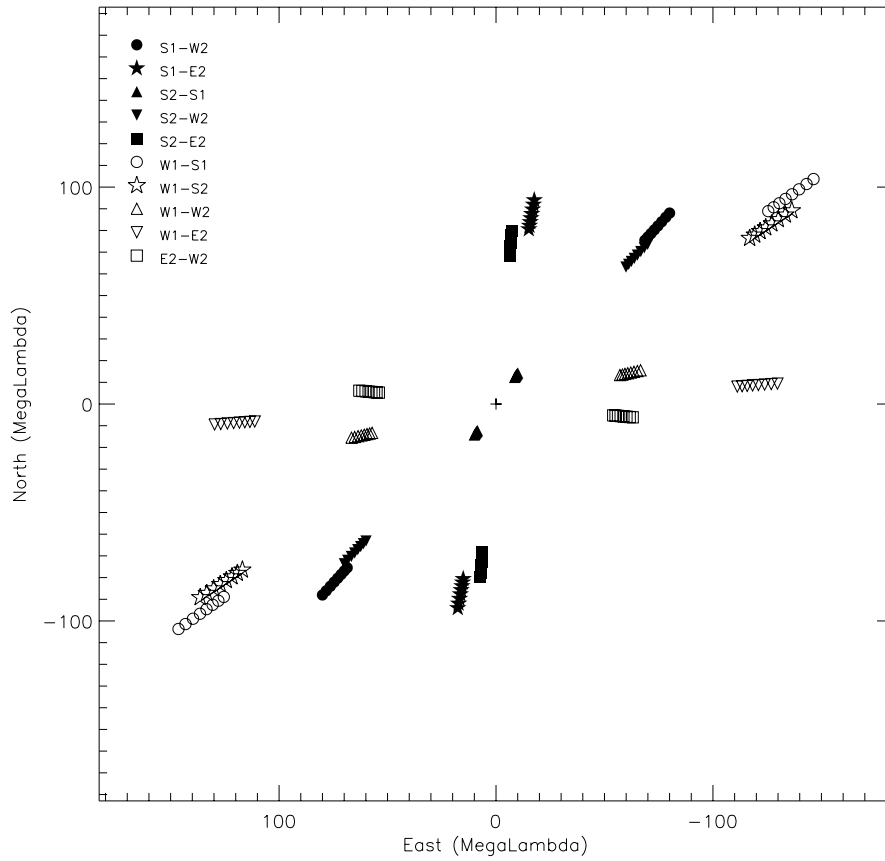
Figure 3.1. (u,v) coverage of one typical night (2011 July 22) observation of δ Sco with upgraded MIRC. The observation was taken in the H filter which is further divided into 8 spectral channels. The figure is reprinted from Che et al. (2012b).

is lower, and that the triple amplitude errors are no less than $0.15 \times$ triple amplitudes or .00002. Lastly, we apply a minimum noise threshold of 1 degree for the closure phases.

3.2.2 NPOI Interferometry

The visible interferometric observations were obtained as an extension of the results presented in Tycner et al. (2011), which focused on refining the orbital parameters of the δ Sco system before the periastron passage of 2011. The data presented in Tycner et al. (2011) were acquired using the Navy Prototype Optical Interferometer, which was recently upgraded to a fully operational status and is known as the Navy

Precision Optical Interferometer (NPOI). The NPOI is a six-element optical interferometer capable of simultaneously recording signal from up to 15 unique baselines at 16 spectral channels in the wavelength range 560–870 nm (Armstrong et al., 1998).

In this study we utilized all 96 nights (covering the 2000–2010 time frame) that were presented in Tycner et al. (2011), and we complemented this set with newly acquired additional observations on 32 nights in 2011, including three nights close to the periastron passage in July 2011. The new NPOI observations have been acquired and reduced using the same procedure as described in Tycner et al. (2011) and references therein. The calibrator star ζ Oph (HR 6175, O9V) used to reduce the raw interferometric observations was the same as used previously. This allowed us to simply combine the data from the 32 nights in 2011 to the observational data set previously published in Tycner et al. (2011).

The resulting binary fits to each night of NPOI observations produced the angular separation (ρ) and the position angle (P.A., θ) of the two stellar components. The previously unpublished 32 nights from 2011 are listed in Table 3.2.

3.3 Modeling

3.3.1 Orbital Parameters From NPOI data Only

The spectral resolution of the NPOI places the Hα emission from the disk and the continuum light from the stellar photosphere into separate channels (Tycner et al., 2003). Thus, line-free channels provide relative astrometry of the binary independent of the contribution from the disk. NPOI has observed δ Sco for more than 11 years since the 2000 periastron which provided the best available phase coverage of the binary system. Tycner et al. (2011) did a precise binary orbit fit with NPOI data before 2011 and predicted the 2011 periastron to be on July 06 $\pm$ 2 days. We also include 32 more days of NPOI observations of δ Sco in 2011 from March to July, including a few nights around the predicted periastron. We fit a new orbit of δ Sco to all NPOI data. The new fit (second to the last column of Table 3.3) agrees well with Tycner et al. (2011) in general, as the new data are consistent with the old NPOI

UT Date	MJD[a]	Separation (mas)	PA (°)[b]	σ_{Major} (mas)[c]	σ_{Minor} (mas)[d]	PA error (°)[e]
2011Mar11	55631.319	41.12	28.97	1.399	0.108	2.9
2011Mar13	55633.328	40.56	29.47	1.376	0.113	4.7
2011Mar16	55636.323	40.55	29.16	1.363	0.114	4.8
2011Mar28	55648.339	36.76	31.25	1.076	0.279	3.2
2011Mar29	55649.326	37.26	31.28	1.204	0.126	6.2
2011Apr 2	55653.343	36.20	31.95	1.411	0.120	6.0
2011Apr 5	55656.338	35.37	32.39	1.341	0.116	4.2
2011Apr12	55663.351	32.38	34.92	1.399	0.122	6.9
2011Apr13	55664.337	32.67	34.52	1.412	0.118	6.2
2011Apr15	55666.346	31.29	35.78	1.396	0.123	5.5
2011Apr16	55667.332	32.31	34.55	1.441	0.122	5.5
2011Apr17	55668.319	30.61	36.47	1.350	0.116	4.1
2011Apr18	55669.341	29.67	37.48	1.478	0.118	6.7
2011Apr21	55672.336	28.49	38.75	1.412	0.121	5.4
2011Apr22	55673.323	28.33	38.93	1.404	0.123	7.3
2011Apr25	55676.318	28.08	38.97	1.334	0.127	7.4
2011May 1	55682.344	26.62	40.74	1.468	0.125	8.9
2011May 2	55683.330	25.69	41.53	1.368	0.123	5.2
2011May 3	55684.317	25.31	42.02	1.435	0.118	5.9
2011May 4	55685.339	25.17	42.26	1.369	0.122	5.6
2011May 5	55686.325	24.76	42.71	1.376	0.120	5.3
2011May15	55696.333	21.44	47.43	1.264	0.117	6.6
2011May16	55697.319	20.99	47.96	1.327	0.123	4.5
2011May22	55703.346	19.53	49.79	1.328	0.117	4.3
2011May23	55704.332	18.97	51.40	1.375	0.123	5.7
2011May24	55705.318	18.85	51.31	1.369	0.122	5.6
2011May25	55706.341	18.54	51.91	1.338	0.116	4.2
2011May26	55707.327	18.83	50.61	1.331	0.120	7.9
2011May27	55708.350	18.48	51.29	1.219	0.137	9.6
2011Jul 3	55745.240	6.18	173.79	1.161	0.097	0.2
2011Jul13	55755.321	7.81	230.23	1.036	0.094	0.8
2011Jul23	55765.329	10.64	272.12	1.024	0.092	1.4

[a] MJD = JD - 2400000.5

[b] Position angle of the secondary, East of North

[c] Semi-major axis of error ellipse

[d] Semi-minor axis of error ellipse

[e] Position angle of error ellipse, East of North

Table 3.2. δ Sco astrometric measurements from NPOI in 2011

Parameters	Tango et al. (2009)	Tycner et al. (2011)	NPOI only (new fit)	NPOI and MIRC
a (mas)	98.3 ± 1.2	99.1 ± 0.1	99.041 ± 0.030	98.94±0.14
i (deg)	38 ± 6	32.9 ± 0.2	32.30 ± 0.30	34.12±0.79
Ω	175.2 ± 0.6	172.8 ± 0.9	174.4 ± 0.6	175.0±2.1
e	0.9401 ± 0.0002	0.9380 ± 0.0007	0.9387 ± 0.0005	0.9373±0.0009
ω	1.9 ± 0.1	2.1 ± 1.1	0.2±0.6	-0.5±2.5
T_0 (MJD)[a]	51797.4 ± 0.1	51797.0±0.5	55745.53±0.16	55745.29±0.19
P (days)	3922.7 ± 7.3	3950.8± 1.8	3947.73±0.46	3945.4±2.8
Reduced χ^2[b]	-	-	0.51	2.5

[a] MJD = JD - 2400000.5

[b] of all NPOI data

Table 3.3. The Orbital Parameters of δ Sco

orbital data of δ Sco . Because the 32 new NPOI astrometric measurements are close to periastron, the orbital period and the time passage through the periastron are much better constrained. All NPOI data and the fitted orbit are shown in the Figure 3.2. Figure 3.3 zooms in around the periastron. The new predicted periastron obtained by fitting to all NPOI data was UT 2011July 03 12:40 ± 4:10.

3.3.2 Modeling the δ Sco Components

The modeling of δ Sco contains three components: the primary, the secondary, and the disk. Be stars are generally thought to contain a near-critically rotating star. However most papers from literature have concluded δ Sco is not rotating close to the critical rate. One of the possible reasons is that they assumed the same inclination angle for the primary star and the orbit, which is a reasonable approximation when the stellar inclination angle is unknown. We adopt a rapidly rotating model for the primary star. However since the primary is not fully resolved by MIRC/CHARA and it is contaminated by the flux from the disk, the infrared interferometry data are not sufficient to constrain the primary parameters.

Therefore we use a new way (Kraus et al., 2012b) to iterate the rapidly rotating stellar model (Aufdenberg et al., 2006) to get a set of stellar parameters that are consistent with observations from literature. Then the stellar angular size can be estimated given the distance 150 pc. The observations include $v \sin i = 157$ km s^{-1} (Glebocki & Gnacinski, 2005), V band magnitude before 2000 periastron (no positive disk detection) $V_{mag} = 2.31$, apparent effective temperature $T_{eff} = 27000$K (Carciofi et al., 2006; Miroshnichenko et al., 2001). We also use the HR diagram as one more
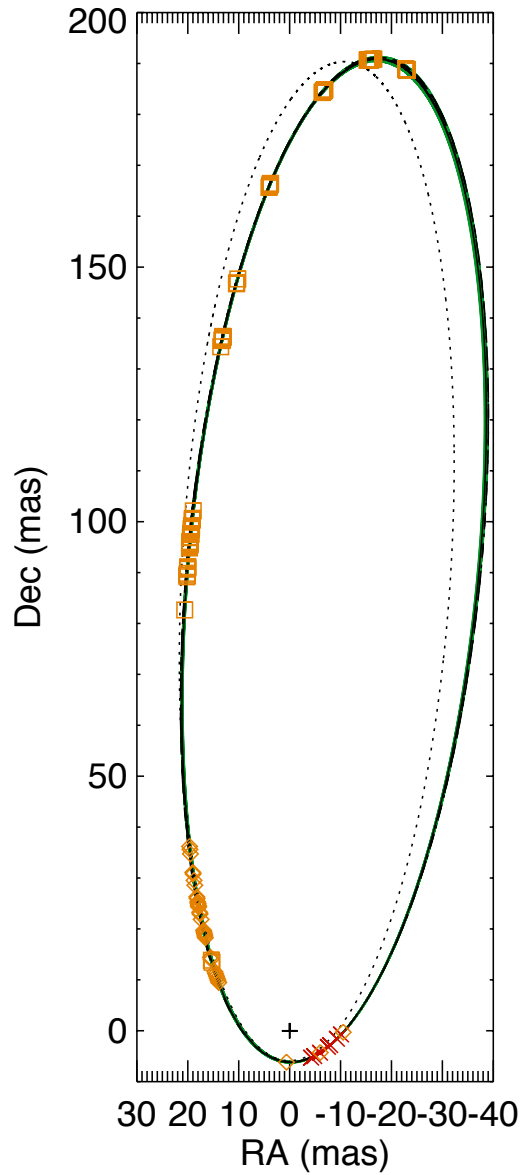
Figure 3.2. δ Sco secondary orbit. The orange symbols represent NPOI data, the squares are old NPOI data from Tycner et al. (2011), the diamonds are new NPOI data measured in 2011. The red crosses are MIRC/CHARA astrometric measurements during 2011July. The plus sign is the fixed primary. The green and black solid lines are the binary orbits from global model fitting to both NPOI and MIRC data (see Section 3.4), the black line is the best fit orbit while the width of the green line represents the uncertainty of the orbit. The dotted line represents the orbit from Tango et al. (2009). The dashed line is orbit from Tycner et al. (2011). The dotted-dashed line is the orbit from model fitting to both new and old NPOI data. The figure is reprinted from Che et al. (2012b).
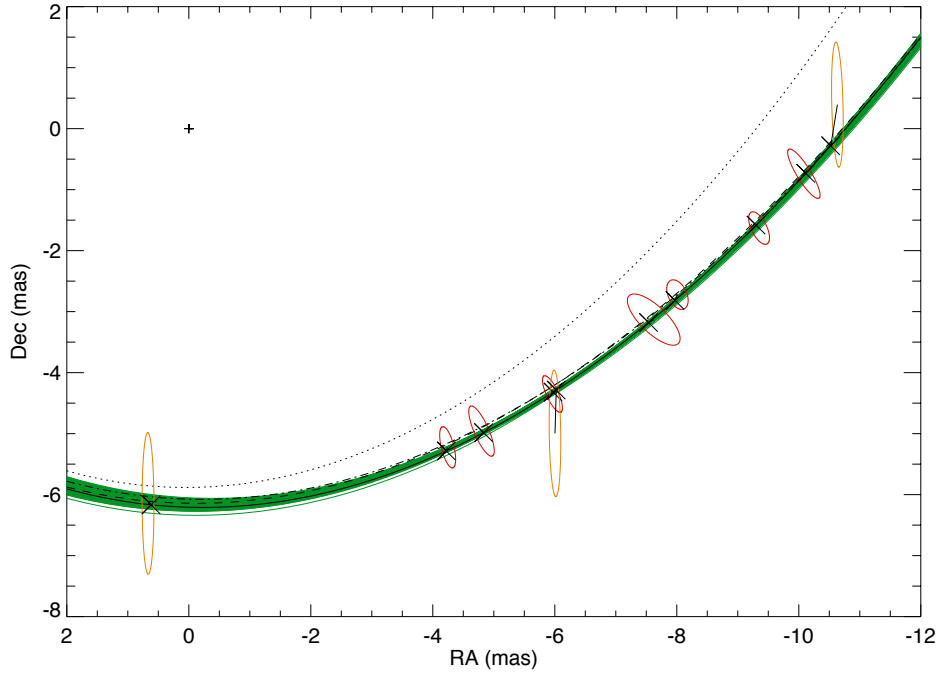
72

Figure 3.3. Zoom in around the periastron of the δ Sco secondary orbit. The notations of the lines are the same as in the Figure 3.2. The orange ellipses represent the uncertainty of NPOI astrometric measurements at each epoch, while the red represent MIRC. The cross symbols are predicted secondary positions from the global model fitting at different epochs of MIRC and NPOI data. The figure is reprinted from Che et al. (2012b).

constraint to the model. The rapidly rotating stellar model contains 6 parameters: stellar mass, inclination angle, fractional angular velocity, polar radius, polar temperature, and the gravity darkening coefficient. The last parameter is fixed to 0.19 (Che et al., 2011) for hot stars with radiative-dominated envelopes. This still leaves 5 free parameters but only 4 constraints, so we did a 1-D grid search of inclination angles and the resulting stellar model parameters are listed in Table 3.4. The detailed steps are listed below.

1. Fix stellar inclination angle

2. Assign stellar mass of the first iteration to $15\,\mathrm{M_\odot}$(Tango et al., 2009)

3. Calculate stellar polar radius, fractional angular velocity and polar temperature based on the $v \sin i$, V band magnitude and apparent T_{eff} measurements above using a rapidly rotating stellar model (Aufdenberg et al., 2006).

4. Following the procedure outlined by Che et al. (2011), we calculate the non-

rotating equivalent luminosity and effective temperature based on the gravity-darkened model (Sackmann, 1970)

5. Place the star on a non-rotating HR diagram (Ekström et al., 2012) based on its corrected luminosity and T_{eff} (Che et al., 2011)

6. Compare the derived stellar mass from HR diagram with the assumed mass in step 2. Iterate from step 2 until these two masses agree

Among the stellar models in Table 3.4, we adopt the 25° inclination angle model with Ω/Ω_c= 0.87 which is the average value from Frémat et al. (2005). Actually the difference between stellar models in Table 3.4 is less than 0.5% in terms of visibility, and this difference is negligible considering the primary only contributes a small amount of H band flux as we will see in the following sections. We further simplify the primary model with 25° inclination angle as a uniform ellipse since it is barely resolved by MIRC/CHARA. The mean diameter of the uniform ellipse from the fitted results is 0.22mas at distance of 150pc, and the ratio between the major and minor axes is 1.03. This leaves the flux fraction and stellar position angle of the major axis as the only two free parameters for the primary. We should emphasize that the flux of each component we mention is the flux ratio to the total flux rather than the flux in physical units.

Inclination (°)	40	30	25	20	17
Mass ($M_\odot$)	14.2	14.0	13.9	13.7	13.5
Ω/Ω_c	0.66	0.79	0.87	0.96	0.997
Polar radius ($R_\odot$)	6.8	6.5	6.2	5.7	5.2
Polar radius (mas)	0.21	0.20	0.19	0.18	0.16
Equatorial radius ($R_\odot$)	7.3	7.3	7.3	7.4	7.4
Equatorial radius (mas)	0.22	0.22	0.22	0.23	0.23
Polar temperature (K)	28000	28000	29000	29000	30000
Equatorial temperature (K)	26000	25000	25000	23000	20000
True luminosity ($L_\odot$)	24000	22000	20000	18000	16000
Apparent luminosity ($L_\odot$)	25000	25000	25000	25000	26000

Table 3.4. Primary stellar parameters

We adopted a simple uniform disk model for the secondary because the stellar size is too small to be resolved by MIRC/CHARA and there are no spectroscopic measurements of the secondary from literature to constrain a rapidly rotating model

as we did for the primary. Bedding (1993) measured the V band magnitude difference between the primary and the secondary to be $\Delta m = 1.5 \pm 0.3$ before the 2000 periastron. The effective temperature of the secondary is approximated with T_{eff} = 22000K based on the spectral type B2V (Kenyon & Hartmann, 1995). Given the primary $T_{\text{eff}} = 27000$K and radius = 0.22 mas , we calculated the radius of the secondary to be 0.12 mas , and the flux ratio of the binary in H band to be 3.3:1, which is fixed in the following model fitting. The secondary has two more free parameters: its position relative to the primary in the projected two-dimension space.

In our model, the intensity of the disk is assumed to follow a 2D Gaussian profile in the radial direction, with a hole in the center containing the central star. The disk model contains 5 parameters: radius of the disk hole ($R_{diskhole}$) and Half Width at Half Maximum (HWHM) of the intensity profile along the major axis , disk inclination angle (i), position angle (PA) of the major axis (East of North), and flux fraction. The first 4 parameters are schematically visualized in Figure 3.4. The disk is assumed to be circular, the projected elliptical shape on the plane of the sky is caused by the inclination angle. Therefore radius of the disk hole and HWHM along the minor axis are scaled down by a factor of $\cos(i)$ compared with those along the major axis. As the inner edge of the disk is very close to the stellar surface, $R_{diskhole}$ along the major axis is fixed to the radius of the primary star along the major axis. The position angle of the major axis of the disk is always matched to the position angle of major axis of the primary during the model fitting.

The sum of the flux fraction from the disk, primary and secondary is a free parameter instead of fixed to 1, because we find some large scale envelope extended to several mas   contributing a few percentage of the total flux. The envelope is so resolved that it acts as a scaling effect to the measured visibilities.

3.3.3   Astrometric Measurements From MIRC

We did a 2D grid search of secondary position relative to the primary for each epoch of the MIRC data using a symmetric disk model for simplicity. The reduced χ^2 of each pixel of the 2D grid is conservatively scaled, being divided by the reduced χ^2_{min}
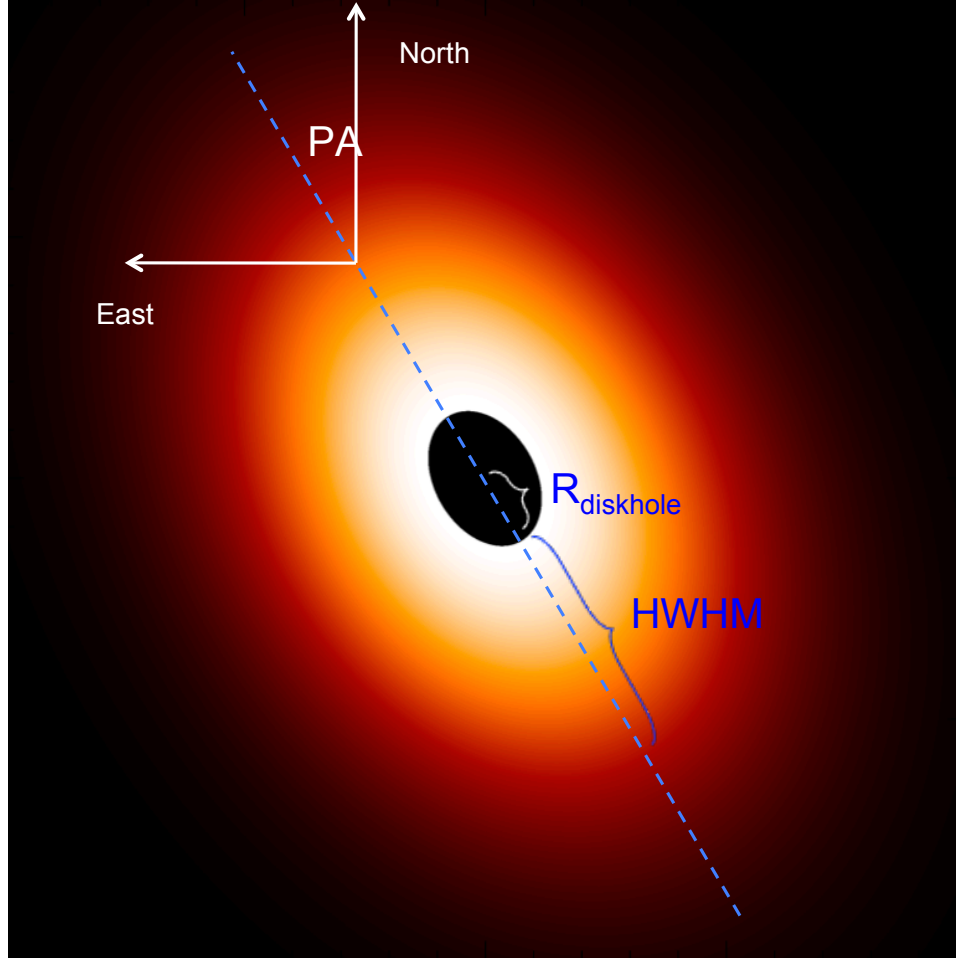
Figure 3.4. 2D Gaussian intensity profile of the disk model with a hole in the center (Che et al., 2012b).. The geometry of the disk model is described by radius of the disk hole along major axes ($R_{diskhole}$), disk inclination angle (i), half width at half maximum (HWHM) of the intensity profile along major axis, position angle (PA, East of North). The model disk image presented here uses the disk parameters from the global model (Section 3.3.4).
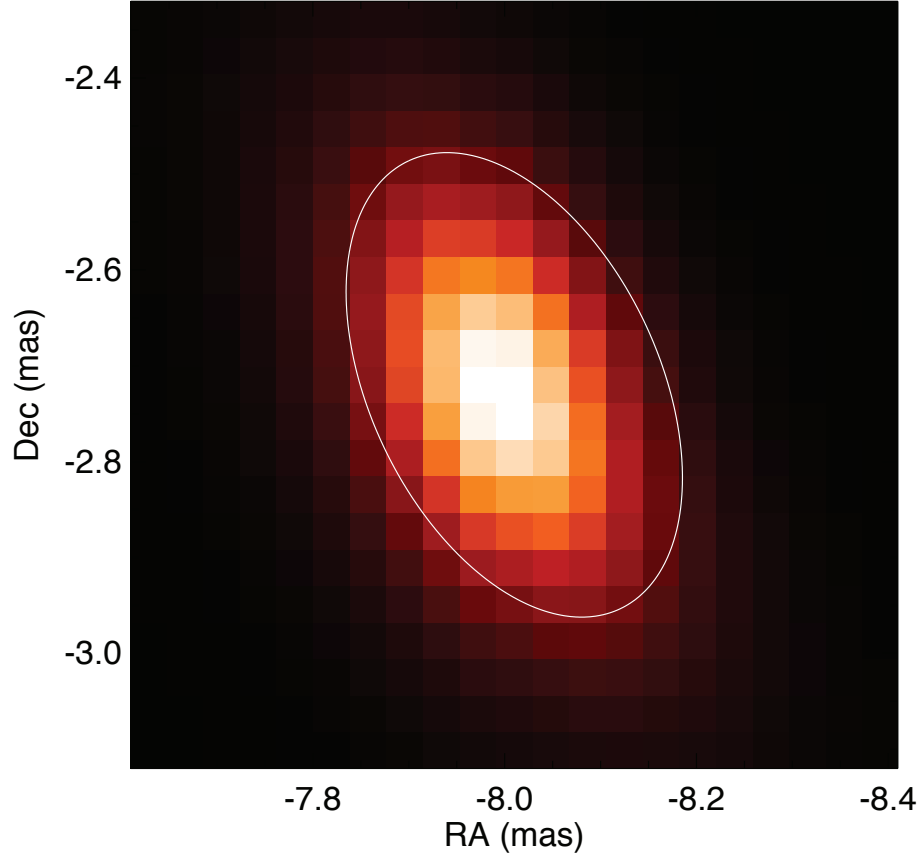
Figure 3.5. likelihood space of secondary position from symmetric disk model fitting to 2011 July 17th MIRC data. The solid line is the error ellipse, which contains 68.3% of the probability. The figure is reprinted from Che et al. (2012b).

of the grid because of the correlation between errors of data points. Then the new χ^2 space is translated into likelihood space by likelihood $\sim exp(-0.5 \times \chi^2)$. The errors of the secondary position are defined by the error ellipse which contains 68.3% of probability with minimum area. Figure 3.5 shows an example of the likelihood space of MIRC UT 2011July 17 with the white solid error ellipse. The astrometric measurements from MIRC are listed in Table 3.5.

3.3.4 Global Symmetric Disk Model

The disk may or may not be distorted by the gravitational force of the secondary during periastron. As a reasonable start, we assume the disk to be symmetric and

UT Date	MJD[a]	Separation (mas)	PA (°)[b]	σ_{Major} (mas)[c]	σ_{Minor} (mas)[d]	PA error (°)[e]
2011Jul10	55752.237	6.73	219	0.348	0.103	14.0
2011Jul11	55753.236	6.90	224	0.446	0.119	23.5
2011Jul13	55755.227	7.38	234	0.327	0.097	24.9
2011Jul16	55758.260	8.24	248	0.562	0.217	46.1
2011Jul17	55759.176	8.46	251	0.258	0.151	25.3
2011Jul20	55762.205	9.49	260	0.291	0.126	26.2
2011Jul22	55764.249	10.11	266	0.471	0.114	31.7

[a] MJD = JD - 2400000.5
[b] Position angle of the secondary, East of North
[c] Semi-major axis of error ellipse
[d] Semi-minor axis of error ellipse
[e] Position angle of error ellipse

Table 3.5. δ Sco astrometric measurements from CHARA/MIRC

fit the model to MIRC data of individual nights independently, namely the disk flux and size from different nights are not forced to be consistent. The details of each component of the model is described in Section 3.3.2. Table 3.6 lists only the disk parameter results of the model fitting. The errors of the disk parameters are estimated by bootstrapping the visibilities and closure phases from the same night based on baselines and triangles. The fact that the disk flux fraction of the total flux and the disk geometry are similar for models of different nights implies a stable inner disk during the period of MIRC observation time. The small variations may be due to the systematic error changes from night to night.

In order to better control from night-to-night systematic errors and to constrain the average disk properties, we construct a global model. Each component of the global model is essentially the same as described in Section 3.3.2. The properties of the symmetric disk are consistent through all 7 MIRC/CHARA nights and the secondary positions are constrained to follow a Keplerian orbit. The global model is fit to both NPOI and MIRC data simultaneously. The model data from the fitted results and MIRC data on the same night are plotted in Figure 3.6 to 3.9. Table 3.7 lists the results of the disk, primary and secondary parameters from the global model fitting. The fitted results of the orbit are listed in last column of Table 3.3. The larger errors on the orbital parameters from the global model fitting compared with those from NPOI-data only fitting suggest some inconsistency between the MIRC and NPOI data due to calibration or other systematic errors. The reduced χ^2s of

each epoch of MIRC/CHARA data are reported in Table 3.6. The green solid line in Figure 3.2 shows the corresponding orbit and the width of the line represents the uncertainty. Originally the errors in Table 3.7 were obtained by treating data from each night as a whole package and bootstrapping MIRC and NPOI packages separately with replacement. But this treatment does not properly take into account the astrophysical scatter of the disk properties. So to be more conservative, we use the standard deviations of the disk properties of each MIRC observation (Table 3.6) as the errors for the global model. From now on, all the model parameters mentioned below are from the global model fitting of both MIRC and NPOI data if not specified. Figure 3.10 shows the model images of the primary and its disk for the 7 nights of MIRC/CHARA observation, over-plotted with the predicted orbits.

We compare the parameters from the global model fitting with those from Millan-Gabet et al. (2010) which modeled δ Sco with data observed with MIRC/CHARA in 2007, and those from Le Bouquin et al. (2011) which modeled δ Sco with data observed with PIONIER/VLTI on June 4th 2011. The disk contributes $71.4 \pm 2.7\%$ of the flux in H band in 2011, which is much higher than $\sim 30\%$ flux contribution from the disk in 2007 from Millan-Gabet et al. (2010). This agrees with the visible photometry observation that V_{mag} in 2007 is at least 0.3 magnitudes fainter than it is in 2011. However the disk FWHM in H band in 2011 is $(0.34 + 0.22) \times 2 \sim 1.1$ mas , which agrees with 1.18 ± 0.16 in 2007 from Millan-Gabet et al. (2010) and a little smaller than Le Bouquin et al. (2011) ~ 1.5 mas. The relatively stable disk size in the H band may be because H band flux only comes from the hot part of the disk, and the disk temperature beyond ~ 1 mas is too low to contribute significantly to the H band flux. According to our modeling, the flux contribution from the secondary is $\sim 6\%$, which agrees with $6.3 \pm 0.5\%$ from Le Bouquin et al. (2011). The position angle of the disk in 2007 is $25 \pm 29°$ (Millan-Gabet et al., 2010), which agrees with our result $9 \pm 14°$. The orbital parameters are in general consistent with those from Tycner et al. (2011). The revised periastron timing from MIRC and NPOI data in 2011 of UT2011July 03 $07:00 \pm 4:30$, agrees with that from NPOI data only.

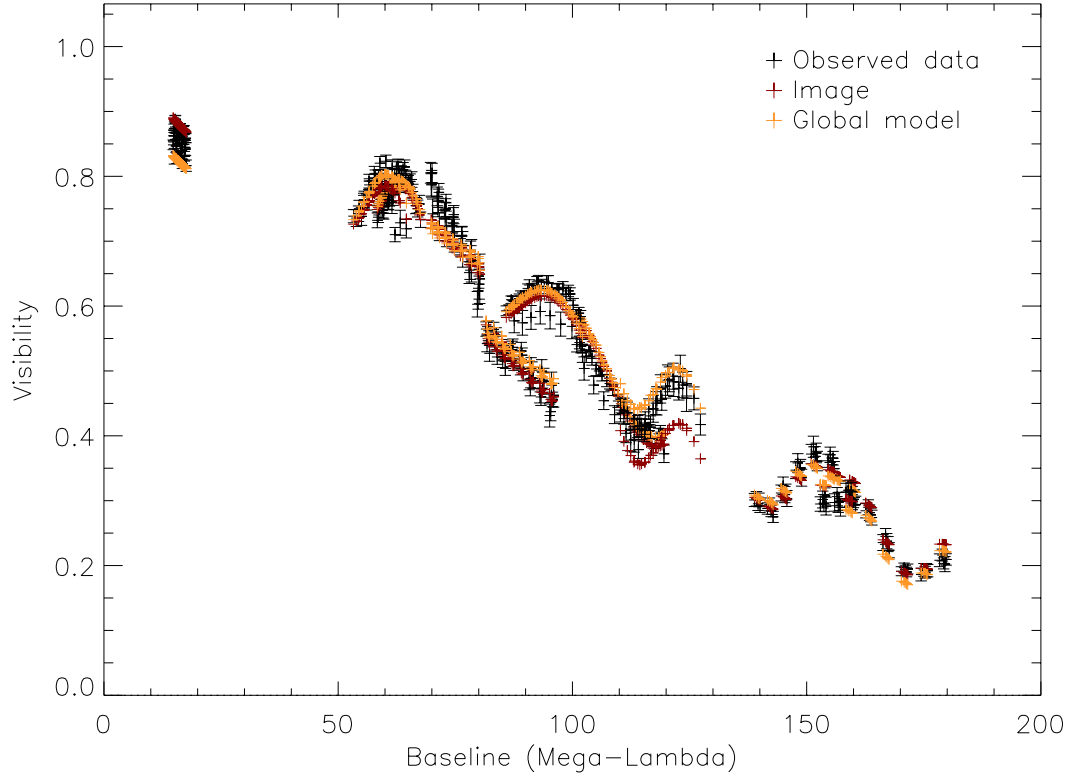The flux ratio from the large scale envelope is found to be $\sim 3\%$ (Table 3.7).

79

Figure 3.6. All visibilities of different baselines from MIRC observation on 2011 July 22nd are plotted together. The observed data are in black, and model data from the global model (Section 3.3.4) in yellow and the model data from imaging (Section 3.4) in red. The figure is reprinted from Che et al. (2012b). The notations are the same for the following figures 3.7, 3.8, 3.9.

UT Date	Disk Flux Fraction	$i^{\circ a}$	HWHM (mas)[b]	PA ($^{\circ}$)[c]	Reduced χ^{2d}
2011Jul10	0.718±0.008	24±5	0.342±0.015	27±5	1.5
2011Jul11	0.760±0.011	28±4	0.366±0.017	20±3	1.1
2011Jul13	0.715±0.010	31±2	0.365±0.013	-9±5	0.8
2011Jul16	0.749±0.018	23±2	0.319±0.014	5±8	0.8
2011Jul17	0.688±0.007	21±4	0.314±0.014	11±6	1.9
2011Jul20	0.694±0.008	32±3	0.363±0.009	13±5	1.4
2011Jul22	0.742±0.005	38±2	0.426±0.021	33±2	2.4

[a] Disk inclination angle

[b] Half Width at Half Maximum (HWHM) of the intensity profile along major axis of the disk

[c] Position angle of Major axis East of North

[d] Total reduced χ^2 of equally weighted visibility square and closure phase

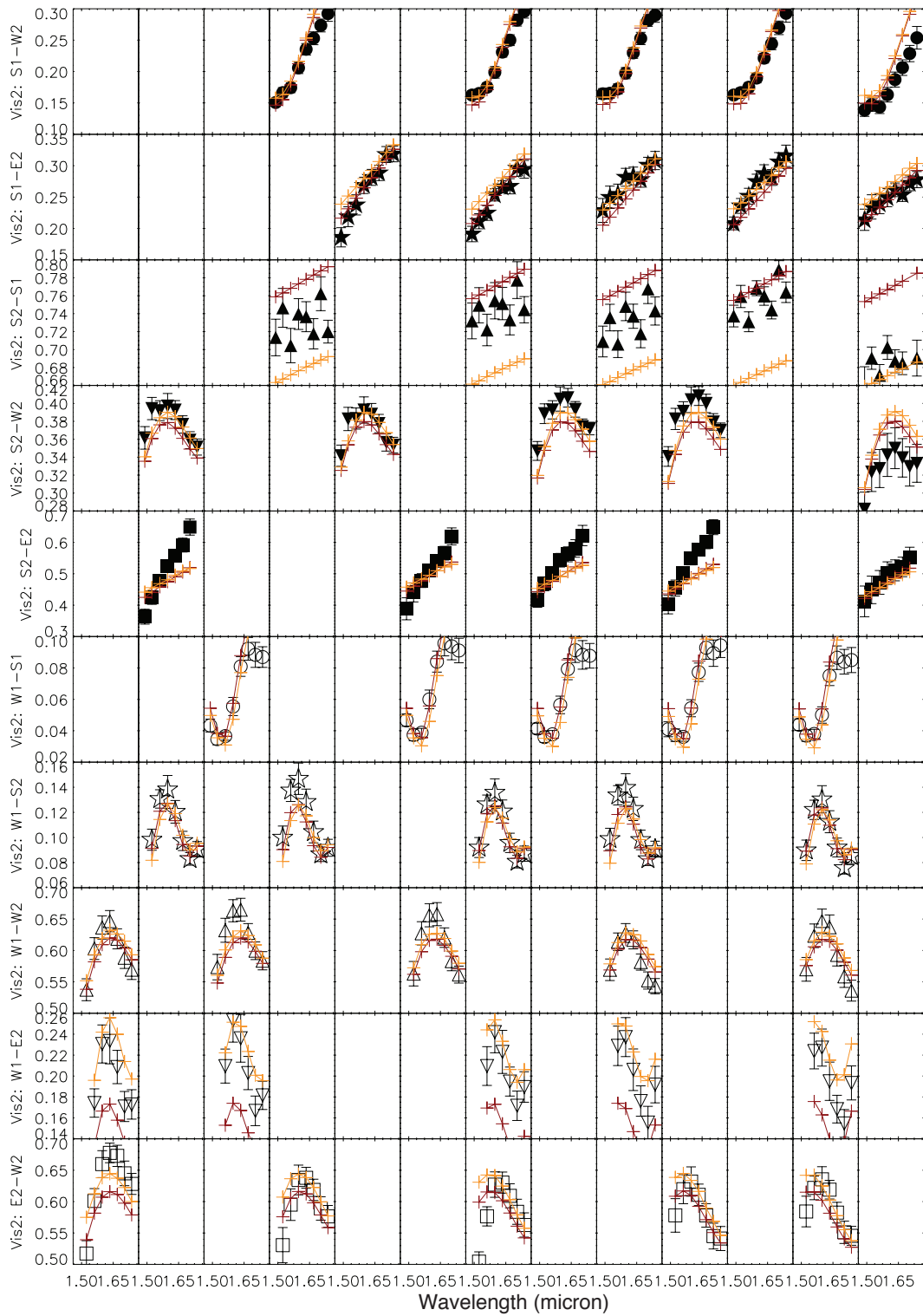**Table 3.6.** Symmetric Disk Model from Individual nights of MIRC data

Figure 3.7. Visibility square of MIRC observation on July 22nd. See the notations in Figure 3.6. The figure is reprinted from Che et al. (2012b).
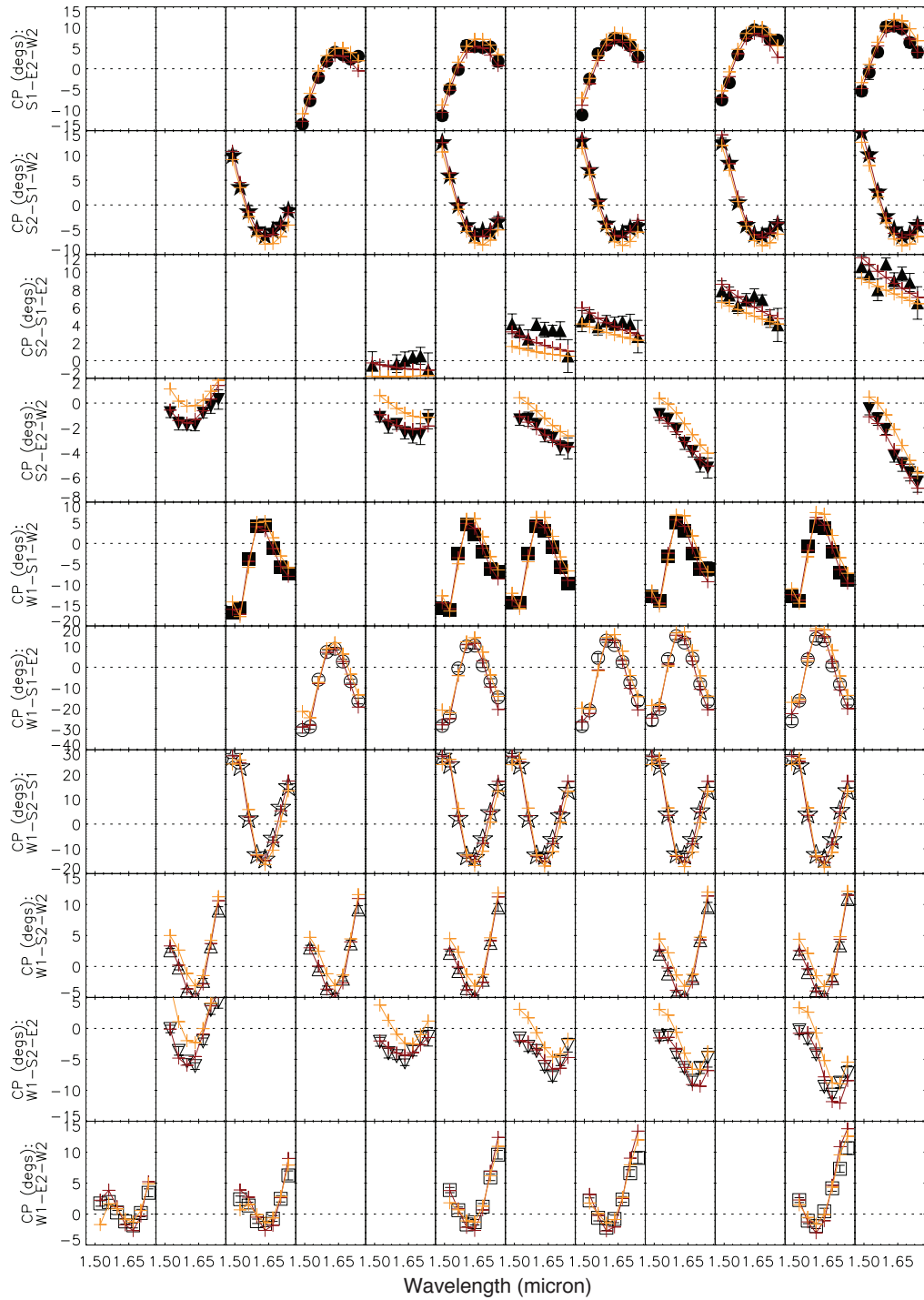
Figure 3.8. Closure phases of MIRC observation on July 22nd. See the notations in Figure 3.6. The figure is reprinted from Che et al. (2012b).
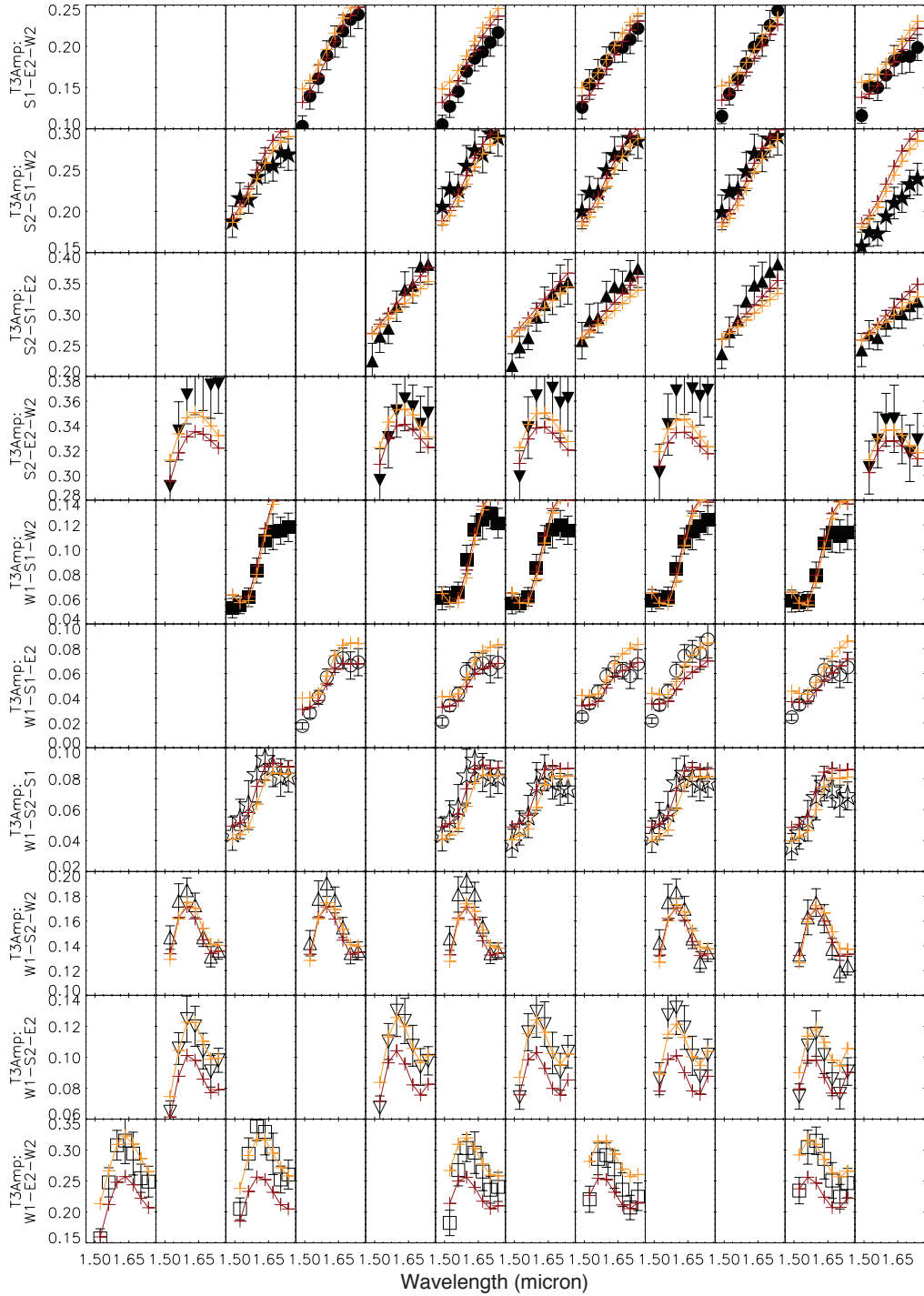
Figure 3.9. Triple amplitude of MIRC observation on July 22nd. See the notations in Figure 3.6. The figure is reprinted from Che et al. (2012b).
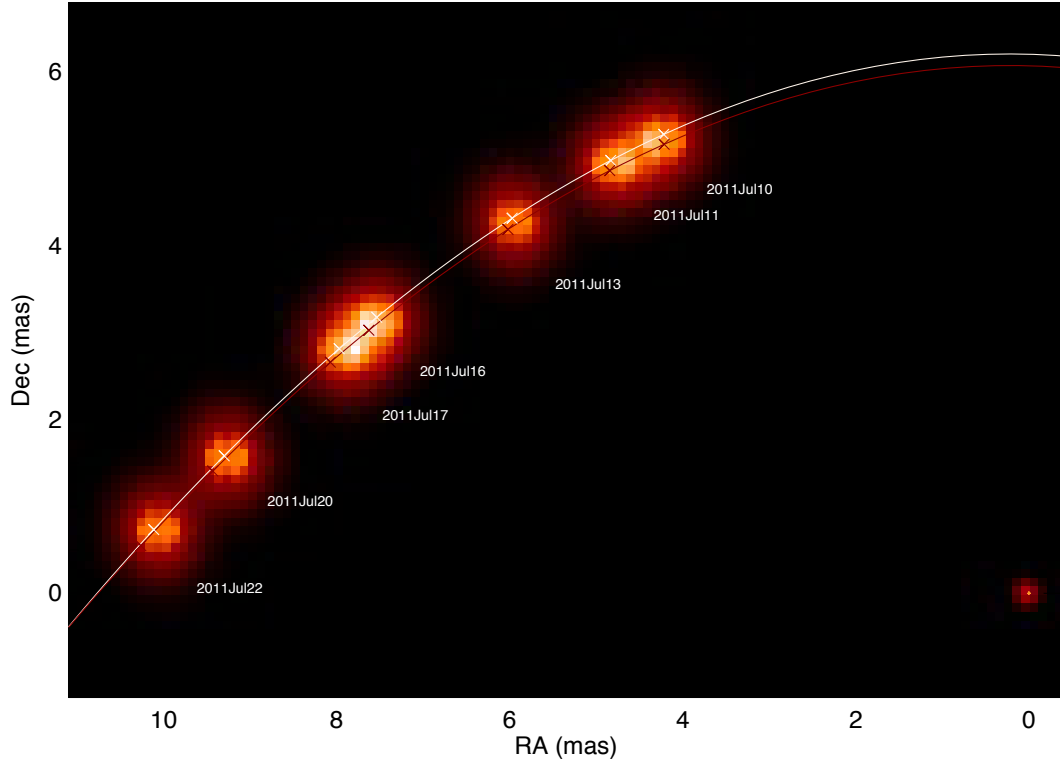
Figure 3.10. The δ Sco images from the global model fitting of 7 nights of MIRC/CHARA observations. The secondary is fixed at origin for all 7 nights, and the primary along with its disk change their positions relative to the secondary from night to night. The white solid line and crosses are the predicted orbit and primary positions on those 7 nights from the global model. The red line and crosses are the orbit and positions of the primary from binary model fitting of NPOI data only. The figure is reprinted from Che et al. (2012b).

Parameters	Values from model fitting
Disk	
Flux Fraction	0.714±0.027
Radius of the hole along major axis ($R_{diskhole}$, mas)[b]	0.22
Disk inclination angle (°)	27.6±6.0
PA of major axis (°, East of North)	9.±14.
HWHM of major axis (mas)	0.341±0.038
Primary	
Flux fraction	0.195±0.019
Radius along major axis[b](mas)	0.22
Radius along major axis[b](mas)	0.21
PA of major axis (°, East of North)	9.±14
Secondary	
Flux fraction	0.060±0.006
Radius[b](mas)	0.12
Flux fraction in extended component	0.032±0.026

[a] the orbital parameters of the global model is shown in Table 3.3, the reduced χ^2s of each epoch of MIRC data are reported in Table 3.8

[b] fixed in the model

Table 3.7. Global model fit to both NPOI and MIRC data[a]

This is not a calibration bias as we find the scaled-down visibilities from different nights of δ Sco observation using different calibrators. The possible explanation of the envelope is an extension of the circumstellar disk. MIRC only sees the H band flux which mostly comes from the inner part of the disk, but the real disk could be much larger as Hα emission line observations show (Meilland et al., 2011). And the fully resolved envelopes in H band are also found in other Be stars (Smith et al 2012, submitted).

3.3.5 Spotted Disk Model

Although the fitting from the global model is good in general, the reduced χ^2s of closure phases of the MIRC data are much larger than unity (Table 3.8). The closure phases are sensitive to the asymmetry of projected images, and the large reduced χ^2s indicate additional asymmetry of the system which is probably from the disk. In order to parameterize the amount of asymmetry, we simply add a bright spot to the disk to represent any asymmetry on the disk. This adds three more free parameters to the model: spot flux, spot position angle and spot distance from the center of the primary. We fix the remaining model parameters from the global model with symmetric disk, and only let the three spot parameters be free and fit to the MIRC data of each night individually. This allows us to see how the point-like asymmetry varies from night to night, and gives us a sense of how asymmetric the disk is. The fitted results are shown in Table 3.8. Although the spot contributes less than 3% of the total flux in H band with a few percent variation, the reduced χ^2s of closure phases decrease by a factor of up to 3 (Table 3.8). The variations of the spot properties from night to night are discussed in Section 3.5.3.

3.4 Imaging the Disk

We employ the algorithm MACIM (Ireland et al., 2006) to reconstruct images of δ Sco . The algorithm has been validated by Lawson et al. (2006). Since the main goal of imaging is to detect any asymmetry of the disk, we fix the primary and secondary parameters from the global model and subtract the interferometric data of the two

		10th[a]	11th	13th	16th	17th	20th	22nd
Global Model	Reduced χ^{2b}	2.61	2.14	1.63	2.36	2.46	2.28	2.38
(Symmetric disk)	Reduced CP χ^2	4.46	3.18	1.82	2.49	3.91	3.66	5.48
	Reduced Visibility χ^2	1.04	1.07	1.43	2.28	0.95	0.96	0.80
Spotted Disk	Reduced χ^{2b}	1.03	1.02	1.03	1.07	1.47	0.95	1.87
	Reduced CP χ^2	1.09	0.95	0.67	1.23	1.97	1.06	2.97
	Reduced Visibility χ^2	0.98	1.08	1.40	0.98	0.95	0.85	0.73
	Flux fraction in spot	0.011	0.010	0.011	0.060	0.010	0.031	0.010
	Spot PA (°)	290	340	350	260	340	310	330
	Spot Distance (mas)	0.84	1.49	1.50[c]	1.42	1.50[c]	0.73	1.21

[a] The dates are in July 2011
[b] Reduced χ^2 is an average of that of equally weighted visibilities and closure phases
[c] The spot distance to the center of the primary is limited to be smaller than 1.5 mas

Table 3.8. Spotted disk model fitting Results

stars to leave only image information for the disk part. We use a model image of the disk from the best global model fitting as an initial starting point for image reconstruction. The model image of the primary is later overplotted onto the disk image (Figure 3.11). The secondary is not shown in the image. The image grid is 40 × 40 with the pixel size of 0.1 mas .

Interferometry constrains the separation between the photocenters of two objects. In the case of δ Sco , one of the objects is the secondary, and the other is the primary plus the disk. Therefore there is degeneracy between the positions of the secondary and the disk relative to the primary: one can move the disk relative to the primary to maintain the same photocenter separation as if the secondary is shifted. An example of how the positions of the secondary and the disk are related is shown in Figure 3.11. The central panel shows the imaging result of the primary and its disk when the secondary is fixed to the position estimated from the global model. The panels surrounding the central panel show the same images when the secondary is shifted 0.1 mas up or down and left or right corresponding to where the panel is relative to the central panel. 0.1 mas is about the uncertainty of the secondary position in the global model fitting. The primary is always fixed at the center of the images as a reference point for the disk. The plus sign in each panel is a reference point for the secondary which is always located 10.14 mas away with position angle of 265.86° (East of North). From the figure, we find the disk always shifts a similar direction and distance as those of the secondary to keep the same photocenter separation. And the
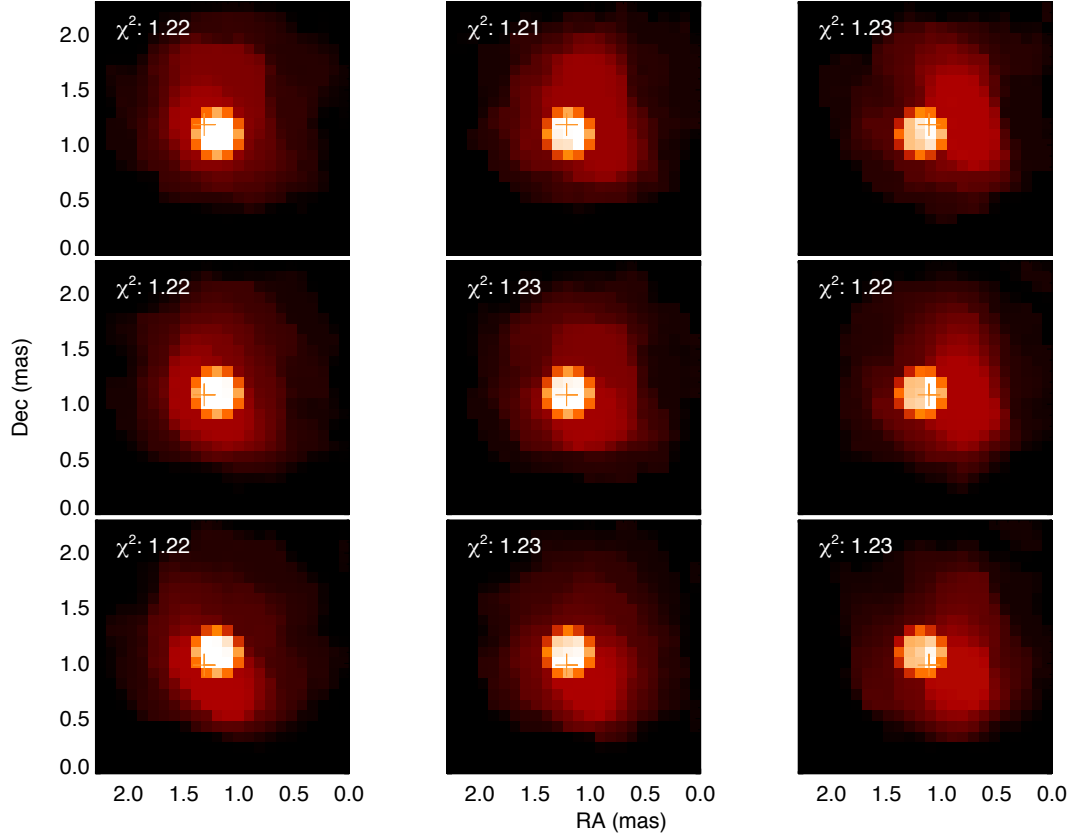
Figure 3.11. The central panel shows the primary plus disk image from MACIM when the properties of the secondary and the primary are fixed from the global model. The other panels show the same images when the secondary is shifted up or down and left or right with step size of 0.1mas . The '+' sign in each panel represents a reference point of which the secondary is located 10.14 mas away with position angle of 266°. The reduced χ^2s of each image is shown in the panels. The disk images are plotted as intensity with power index of 0.7. The figure is reprinted from Che et al. (2012b).

reduced χ^2 of all panels are all about the same. This implies for a range of secondary positions the disk can always shift to compensate. As a result, even if the real disk is symmetric, the disk from imaging could be asymmetric if the secondary is placed at a wrong position relative to the primary star. MIRC data are not able to resolve the position of the secondary and the disk at the same time.

Therefore we fix the separation between the primary and secondary stars estimated from the global model during the imaging process. The comparison of the reconstructed image and the MIRC data on one night is plotted in Figure 3.6 to 3.9. The first 7 panels of Figure 3.12 show the images of the primary and the disk from the 7 nights. The last panel shows the average image of all 7 nights, and the angular
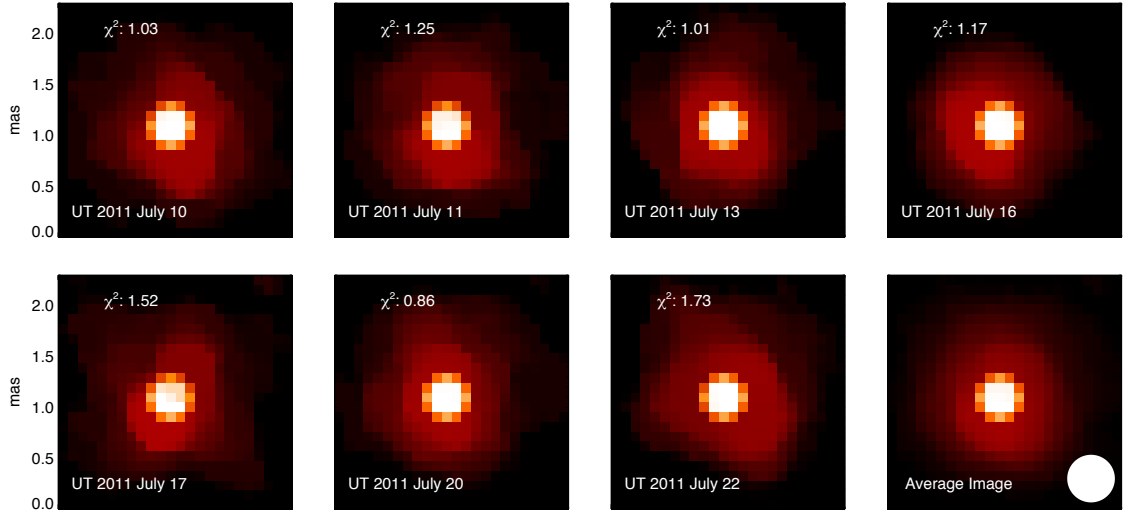
Figure 3.12. Disk plus primary images from 7 nights of MIRC observations. The last panel shows the average images from all 7 nights. The white circle in the lower right corner represents the angular resolution (∼0.5mas) of MIRC/CHARA. The disk images are plotted as intensity with power index of 0.7 to see more details. The figure is reprinted from Che et al. (2012b).

resolution ($\frac{\lambda}{2 \times Baseline}$) of MIRC/CHARA at the lower right corner. The disk images vary from night to night. It is hard to distinguish if the variation reflects real disk structure or some artifact from the imaging reconstruction because the disk size is only about twice the angular resolution. We conclude that imaging the δ Sco disk is really at the limit of the imaging ability of MIRC/CHARA. The average image shows a mostly symmetric disk, with the elongation along north and south which agrees with the disk position angle from modeling.

3.5   Discussion

3.5.1   Binary Masses

The masses of the primary and the secondary can be better constrained with the revised binary orbit. The orbital period and semi-major axis from the global model are 3945.4 ± 2.8 days and 98.94±0.14 mas . The parallax estimation of δ Sco revised by van Leeuwen (2007) is 6.64 ± 0.89 mas . The total mass of primary and secondary derived from Kepler's Law is $M_{total} = 28 \pm 11 M_{\odot}$, the large error bar comes from the uncertainty of the parallax estimation. We also estimate the mass ratio of the primary and secondary stars based on the Radial Velocity (RV) measurements from the 2000 periastron (Miroshnichenko et al., 2001). The likelihood space of the primary and
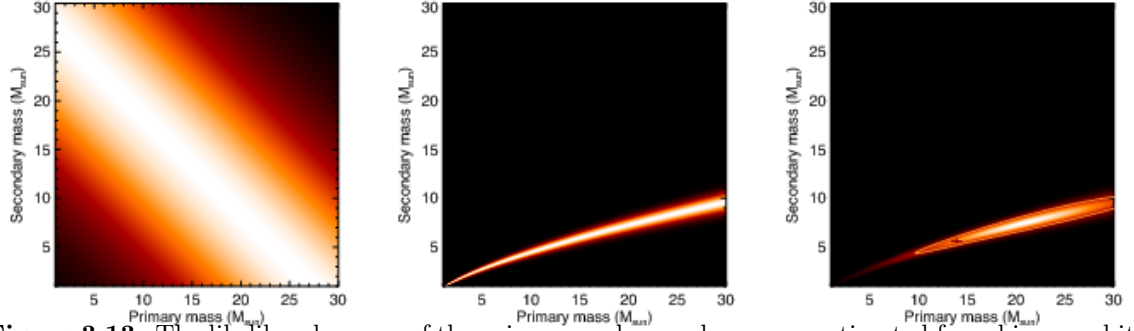
Figure 3.13. The likelihood spaces of the primary and secondary mass estimated from binary orbit (1st panel) and Radial Velocity (2nd panel) measurements. The last panel shows the combined likelihood from the two measurements, the contour represents total 68.3% (1σ) inside. The plus symbol in the last panel represents the binary masses derived from this work. The figure is reprinted from Che et al. (2012b).

secondary masses from the binary orbit and RV measurements are shown in Figure 3.13. The first panel shows a very broad likelihood distribution because of the large error on distance estimation. The last panel is the combined likelihood space. The contour represents a total 68.3% (1σ) of probability inside. As the primary mass is determined to be 13.9 $M_\odot$ from photometry and spectroscopic measurements in Section 3.3.2, the corresponding secondary mass from the combined likelihood space is $\sim$6 $M_\odot$.

3.5.2 Inclination Angles

The inclination of the disk is 27.6±6.0° from the global model fitting, which agrees with the assumed inclination angle 25° of the primary in general. The inclination angle of the orbit is 34.12 ± 0.79 from the global model. The mutual angle between the disk plane and orbital plane is given by:

$$cos\Omega = cosi_1 cosi_2 + sini_1 sini_2 cos(\Omega_1 - \Omega_2) \tag{3.1}$$

where i_1 and i_2 are the inclination angles of the disk and orbital planes, and Ω_1 and Ω_2 are the ascending nodes. We have measured the ascending node of the orbit to be 175.0±2.1°. The ascending node of the disk is less constrained due to two degen-

89

eracies: the side of the disk closer to us and the direction the disk is rotating (Figure 3.14). Fortunately, using archival VLTI/AMBER spectro-interferometric data, we can determine the rotation sense of the disk by measuring the photocenter displacement between the blue- and red-shifted line wing (Kraus et al., 2012b). For this purpose, we used δ Sco data (Meilland et al., 2011) recorded on UT 2010 April 19 and 20 in the He I and Brγ line using AMBER's high spectral dispersion mode of $\lambda/\Delta\lambda = 12,000$. We extract wavelength-differential phases (Figure 3.15, top), from which we compute the corresponding 2-D photocenter displacement vectors (Figure 3.15, bottom) using equation (1) from Kraus et al. (2012b). The signs of the differential phases are calibrated using the method presented in Kraus et al. (2012a), which allows us unambiguously to assign the vector direction to the orientation on sky. Both for the He I and Brγ line, we find that receding (red-shifted) emission is offset to the northwest of the stellar continuum emission. This indicates the binary orbit and the disk are on retrograde orbits, eliminating two cases in Figure 3.14: case 3 and 4. However the PA of the disk from VLTI/AMBER does not agree with that from CHARA/MIRC, so we will report two sets of mutual angles. VLTI/AMBER gives disk PA = 167±3° for Brγ line (Figure 3.15 left panel) and 158±4° for HeI line (Figure 3.15 right panel). The average PA of these two measurements is 163.8±5.8°. The mutual angle between disk and orbital plane is then either 171.3±4.7° or 118.6±6.0°. If we use PA of disk 9±14° from CHARA/MIRC, then the mutual angle is either 170.3±6.4° or 118.8±6.1°

3.5.3   Disk Asymmetry

Although the spotted models fit well to the interferometry data, the spot distances vary from night to night and the position angles of 7 nights do not fit into a period. This is probably because our single-spot model is too simple to reflect the true asymmetry. The spot represents only some kind of average of the real asymmetry, therefore its behavior could appear to be complex from night to night. Also the orbital periods of the inner and outer disk are of order 0.5 to 1.5 days respectively assuming Keplerian rotation. Such short period differential rotation could easily dis-
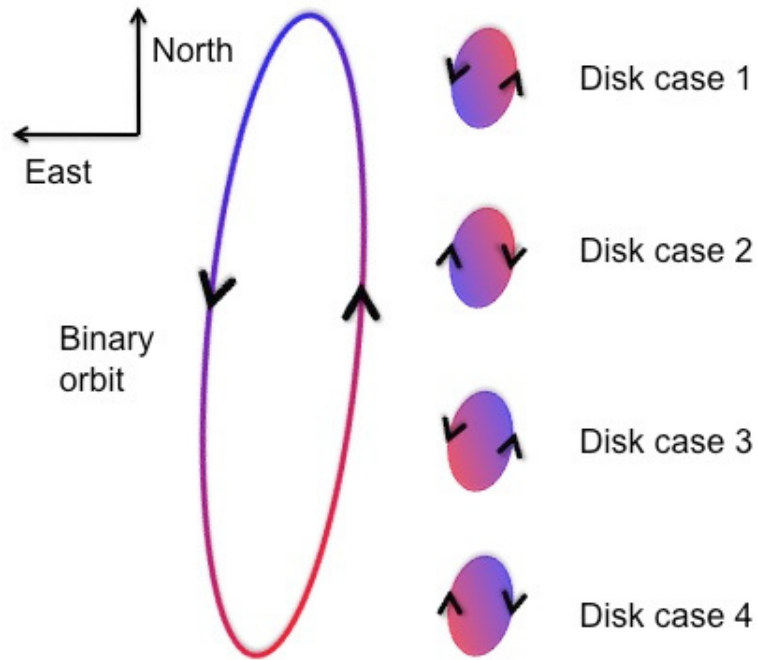
Figure 3.14. The degeneracy of the disk orientation and rotation. The sizes of the disk and binary orbit are not scaled. The big left panel shows the binary orbit, and the right small panels show the four possibilities of the disk orientation and rotation. In each panels, the arrows represent the orientation of the rotation: clockwise or counterclockwise. Red color mean the disk or the secondary are rotating away from us, while blue means they are rotating towards us. Disk case 3 and 4 are eliminated by the VLTI/AMBER data. The figure is reprinted from Che et al. (2012b).
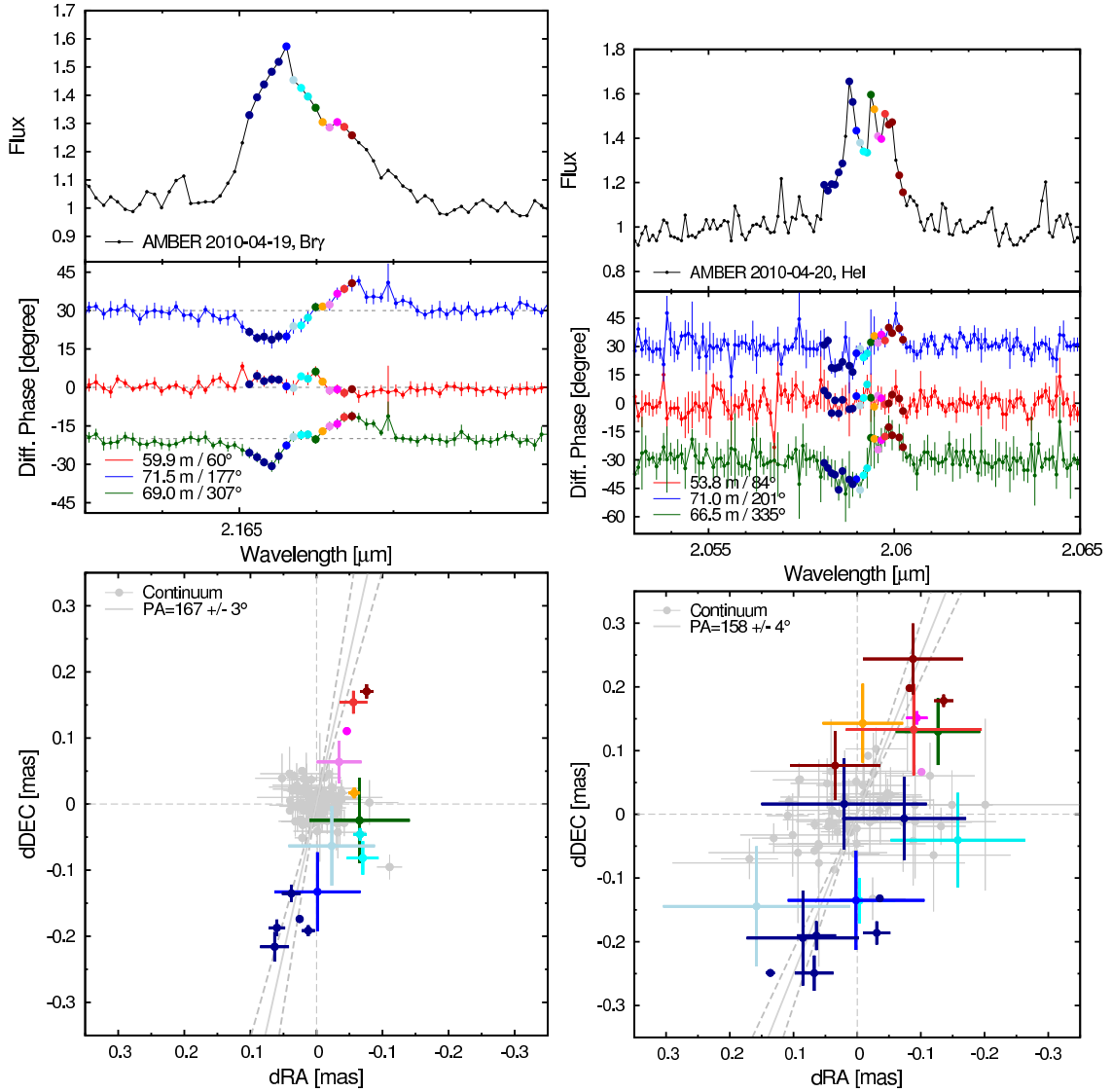
Figure 3.15. Using archival VLTI/AMBER data (2010 April 19 and 20; Meilland et al., 2011), we derive spectra (top row) and differential phases for three interferometric baselines (2nd row from top). From these differential phases, we compute for each spectral channel the 2-D photocenter displacement vector (3rd row from top). The data points are color-coded according to their spectral channel, revealing that the receding (red-shifted) part of the disk is located to the northwest of the star. The figure is reprinted from Che et al. (2012b).

tort the asymmetry pattern and make it different every day. So the most we can get out of the spotted model fitting is that the inner part of the disk is only distorted about a few percent in terms of the H band flux in a point-like asymmetry if there is any. This implies that the secondary passage did not trigger any strong mass outflow from the primary to the disk orbit during this periastron. Any asymmetry in the disk could be caused by some internal dynamic instability of the disk. This is supported by the photometric monitoring[1]over the last few years which shows the disk started to brighten about one year before 2011 periastron and stayed relatively stable during the 2011 periastron passage ($\sim 10\%$ flux variation in V band). Halonen et al. (2008) also find some asymmetry in the Hα line that can not be modeled by an axis-symmetric disk in 2006 away from the periastron, supporting that the disk asymmetry is self-induced. However this seems to contradict the 2000 periastron where many observations supported a growing disk during the periastron. Of course the discussion of the disk in this study is limited to the parts that emit the H band continuum flux, while we are not able to constrain the most extended disk regions ($>$ 1mas). It is still possible that the outer part of the disk (traced by the Hα emission) is more significantly distorted as it is closer to the secondary. For instance, the disk radius measured in Hα line is about 4.8 mas (Meilland et al., 2011). From the global model fitting, the distance between the primary and secondary at periastron is about 6.2 mas . So the gravity force from the secondary is about 13 times stronger at the Hα disk edge than at the H band edge.

3.6 Conclusion

δ Sco was expected to reach periastron in the early July of 2011. We revised the binary orbit and studied the disk properties of the primary star around the periastron with two interferometers: 32 nights of NPOI astrometric measurements during 2011 and 7 nights of MIRC/CHARA H band 5-telescope data about one week after the predicted periastron. A global model where the secondary follows a Keplerian orbit and the

---

[1]$http://varsao.com.ar/delta\_Sco.htm$

disk properties are consistent through 7 nights of CHARA/MIRC observation was fit to all of the data above plus another 96 nights of NPOI astrometric measurements before 2011 (Tycner et al., 2011). The revised the binary parameters agree with Tycner et al. (2011) in general and the new periastron estimation was UT 2011 July 03 07:00 ± 4:30. We also estimated the mass of the secondary, based on the revised binary orbit and radial velocity measurements from Miroshnichenko et al. (2001), to be $\sim$ 6 $M_\odot$, with the primary mass 13.9 $M_\odot$ estimated from $v \sin i$, apparent $T_{\rm eff}$ and V band photometry measurements. The mutual angles between the disk mid-plane and orbital plane are estimated to be either $\sim$ 119° or $\sim$ 171° with the spectro-interferometric data from VLTI/AMBER to partially remove the degeneracy. From the fitted global model, we also find $\sim$3% of the H band flux comes from a fully resolved envelope. The primary disk was found to be mainly symmetric and stable contributing 71.4±2.7% of the total H band flux throughout the 7 nights of the CHARA/MIRC observation. This implies a quiescent inner disk and no on-going material outflow after the periastron. But from closure phase measurements, we also found weak asymmetry structure with less than 3% of total H band flux for a spot-like pattern. However, this does not rule out other complicated asymmetric patterns due to the limited angular resolution.

CHAPTER 4

CHARA Adaptive Optics Upgrade

The work of this chapter has been published (Che et al., 2013), much of the content has been extracted from the paper.

4.1 Motivation

With the highest angular resolution among the operating optical interferometers, CHARA has been contributing to our knowledge of nearby stellar systems. To extend the target pool of fainter objects and improve the science results of bright ones, we have started to install Adaptive Optics (AO) systems on each of the telescopes to correct for atmospheric turbulence. Currently, CHARA has been funded by NSF-ATI for Phase I AO (Ridgway et al., 2008; ten Brummelaar et al., 2012). During this phase, we mainly modify the current optics in telescope domes to prepare for full AO systems and install WaveFront Sensors (WFSs). The WFSs and the modified tip/tilt (TT) systems close the loop. In the meantime CHARA has been applying for the funds for Phase II AO, which will add a large Deformable Mirror (DM) on each telescope to perform full AO correction.

One of the key science goals of the AO upgrade is for imaging Young Stellar Objects (YSOs) in the Near InfraRed (NIR) to study the evolution of the innermost disks and their interactions with the central objects. The practical sensitivity of the current system is of R $\sim$ 12 and H $\sim$ 8, covering 11 known YSOs in Taurus. After the Phase I upgrade, we expect about 50 of them will be observable as illustrated in Figure 4.1.

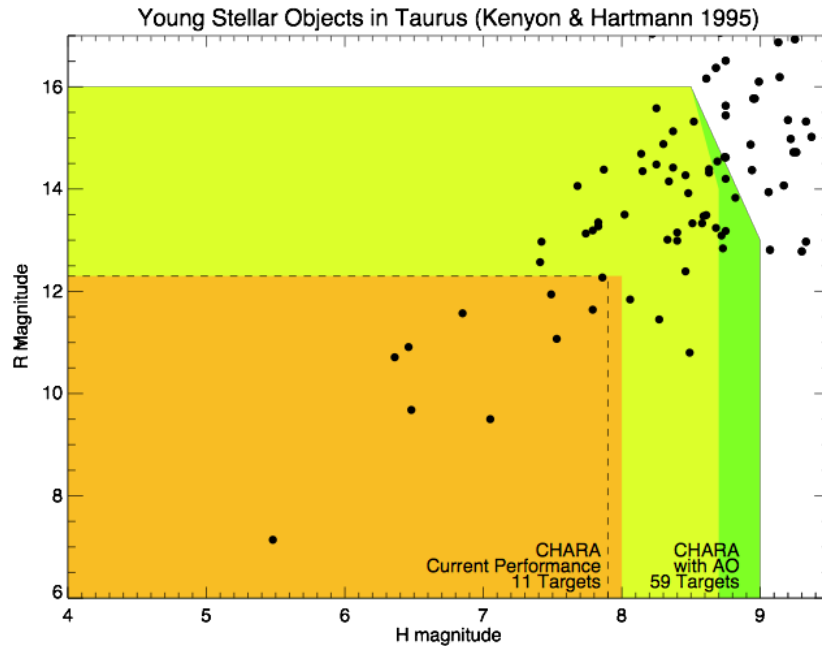In addition to YSOs, a few new classes of objects will be observable with CHARA

Figure 4.1. YSO in Taurus. Currently ~ 11 targets are observable at CHARA, and we expect to observe ~ 59 targets after the full AO upgrade. The figure is reprinted from Che et al. (2013).

for the first time. In particular, the brightest few Active Galactic Nuclei (NGC 4151, NGC 1068, Whirlpool) with K magnitude of ~ 9 will be within the reach of CHARA following the full upgrade. A few brightest microquasars (e.g. SS433, K magnitude 8.2) will also be observable. While the VLTI and Keck Interferometers have had this level of sensitivity for some years, they lacked the >300m baseline that CHARA affords and the high angular resolution is needed for these objects to resolve the rather compact emission in the NIR.

The AO upgrade will also improve the data quality for high-precision science. Most of CHARA targets are bright ones, which will provide enough photons for good AO correction even under poor seeing conditions. This will boost sensitivity by an order of magnitude and allow high quality observations for a higher fraction of the observing season.

4.2 Optical Feed System

The CHARA AO system includes two parts: an Optical Feed System (OFS) and a WaveFront Sensor (WFS). I am mainly responsible for the development of the WFS while the OFS is developed mainly by another team member. The OFS collects light
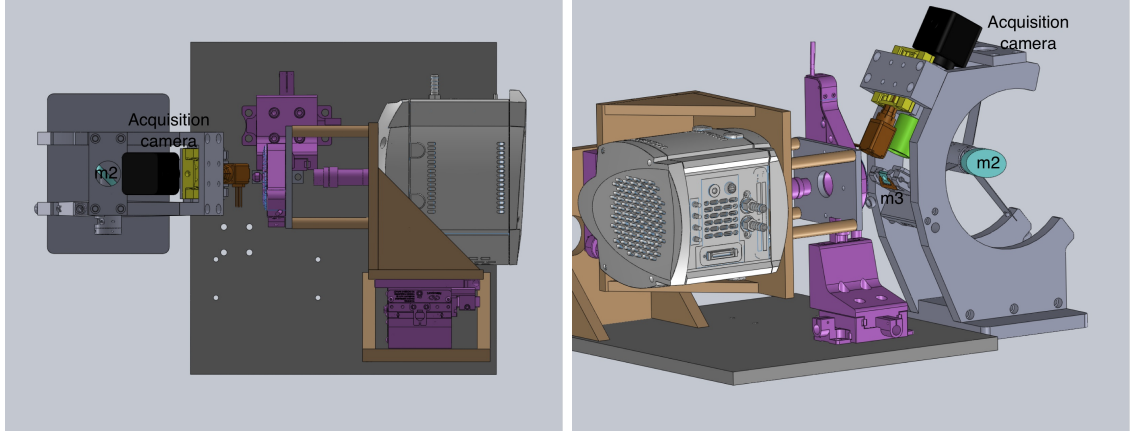
Figure 4.2. Top and side view of how WFS is coupled with one end of the CHARA AO optics. All WFS components are on a separate board. Both panels are reprinted from Che et al. (2013).

from the primary mirror and reflects part or all of the visible light into the WFS depending which beam combiner is used. OFS also includes a light beacon for WFS alignment to mark the reference centroids, and the alignment in the lab downstream. The details of OFS are presented in Che et al. (2013).

4.3   WaveFront Sensor

The beam from Optical Feed system goes through the pinhole of the m3 mirror and enters into the WFS system (Figure 4.2). A Shack-Hartmann style WFS is used because it is simple, stable, compact, and does not involve moving parts.

The WFS system contains a collimator, a lenslet array, a pair of lenses as a re-imaging system, and a camera. The collimator is held on a linear XYZ stage (Newport, 460A-XYZ), and the other parts are mounted on another linear XYZ stage (Newport, 562-XYZ), as shown in the Figure 4.2. The reason for two separate stages is to correct angular and linear deviations of the incoming beam. Figure 4.3 shows how the beam propagates in the WFS.

A fast DM, although not purchased during Phase I AO, is also taken into account for a complete design.
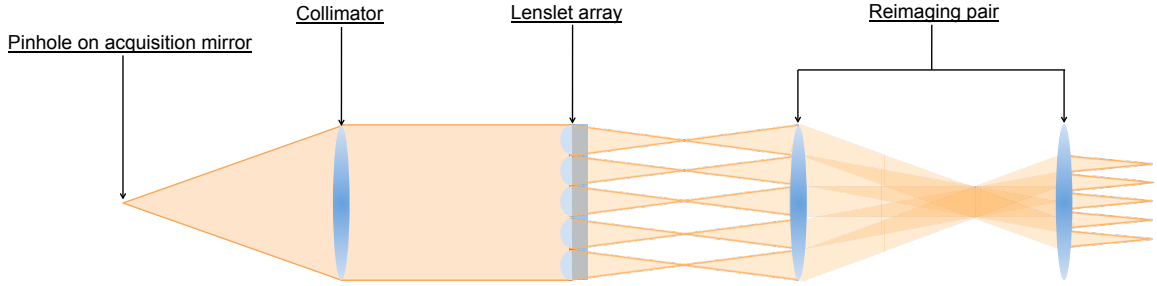
Figure 4.3. Left shows the optics and the camera in WFS. Right (not to scale) shows a schematic drawing how light propagates.
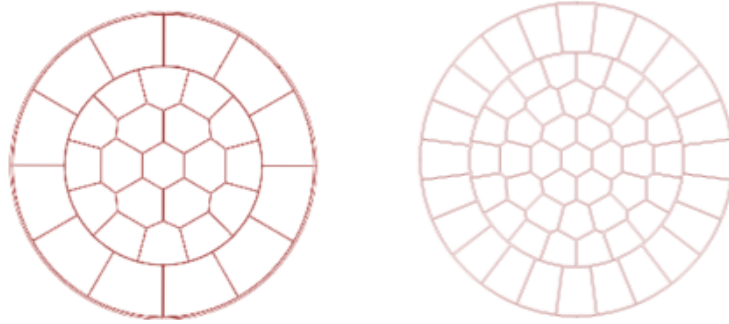

Figure 4.4. Two different actuator geometries of candidate DMs from Cilas. Left has 31 actuators and right 61 actuators. These are the projected geometries of the elliptical DMs. The figure is reprinted from Che et al. (2013).

4.3.1 DM and Lenslet Array

The choices of DM are limited because of the specific requirement to replace M4 in the telescope to maximize sensitivity. The DM has to be large and elliptical, and its 45° projection has to be a circle. And the minimum number of actuators is determined by the seeing condition. Suppose the worst observable seeing condition is $r_0 = 5$ cm at 0.5 micron at CHARA, which is equivalent to 21 cm r_0 in the H band. To match the r_0 in the H band, the minimum numbers of actuators and lenslets across a 1 meter primary pupil are both 5. Two possible different bimorph DMs from Cilas fit these requirements: a 31-actuator (19 inner ones, 5 across the pupil) and a 61-actuator (37 inner ones, 7 across the pupil) device. These two DMs are both pseudo-hexagonal, as shown in Figure 4.4. The geometries of the DMs are used in the simulation.

In order to match geometry of the DMs, an off-the-shelf hexagonal lenslet array from OKO was chosen. The lenslet array has 300 micron pitch, a focal length of 18 mm, and a 100% fill factor. One side of the lenslet array will be coated with an AR coating. The lenslet array is placed at a plane conjugated with the M2 (tip/tilt) mirror so that moving M2 does not shift the pupil on the lenslet array. The DM however is not conjugated to M2. But the beam is slow enough that the pupil on DM is relatively stable. To be quantitative, the pupil on the DM will move in the order of 0.1 mm for every arcsecond of tiptilt motion. This is much less than the distance between the actuators.

We have considered two lenslet configurations: 18 subapertures (5 across the pupil) and 36 subapertures (7 across the pupil). Each subaperture measures two pieces of wavefront information: x and y slopes. So on average a lenslet configuration with n subapertures is able to control a DM with $2n$ actuators. The 18-lenslet configuration roughly matches the 31-actuator DM, and 36-lenslet with 61-actuators. Although the 36-lenslet configuration better samples wavefronts, the 18-lenslet configuration has higher sensitivity. We compare the performance of these two configurations in the simulation in Section 4.4. The geometry and some characteristics of these two lenslet configurations are listed in Table 4.1 and shown in the Figure 4.5.

Another factor to optimize the size of the re-imaged pupil concerns the partially illuminated lenslets along the edge of the pupil. These lenslets distort the stellar images under the diffraction limit and compromise the contained wavefront information. Therefore we only use the lenslets that are illuminated with most of their surface areas, and discard the ones illuminated with a small faction. The size of the pupil on the lenslet array is optimized in a way to maximize the surface areas of useful lenslets and minimize those of discarded lenslets. Table 4.1 summarizes the results of the optimization.

The orientation of the lenslet array must be optimized with respect to the DM actuator positions. We maximize the distances between the centers of the DMs and the centers of lenslet arrays. The lenslet array is held by a rotation stage that can be remotely controlled (Thorlabs, PRM1Z8E). Examples of the optimal orientation are
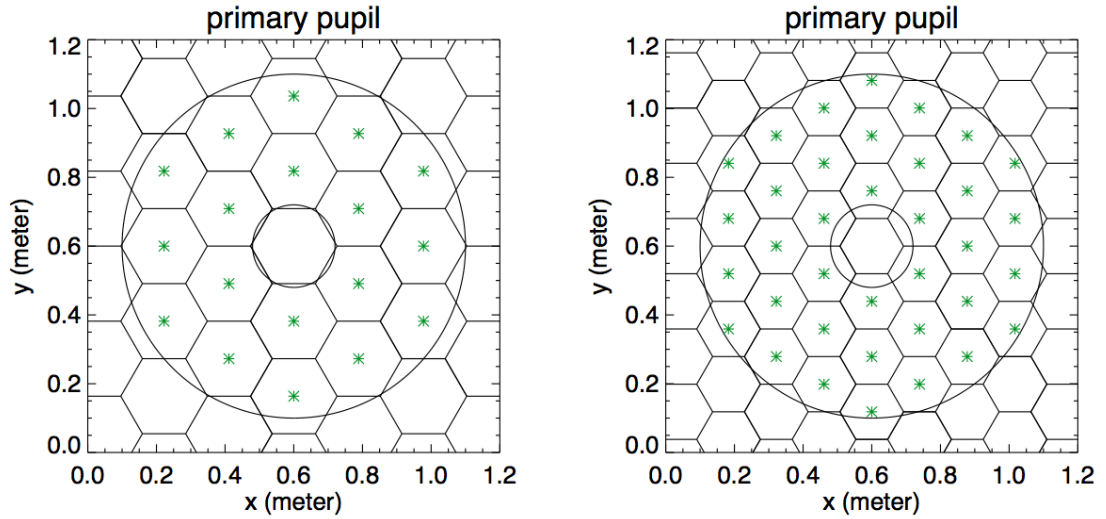
Figure 4.5. The lenslet array from OKO contains 127 micro-lenslets in a hexagonal configuration with 300 micron pitch. The two different scalings of the pupil onto the same lenslet array are shown above, corresponding to pupil size of 1.38 mm (left) and 1.87 mm (right). The large circle is the edge of the primary mirror, and the small circle is the projection of the secondary. The hexagons with green stars inside are the ones that are used to measure the wavefront. Both panels are reprinted from Che et al. (2013).

	18-lenslet	36-lenslet
Number of illuminated lenslets	18	36
Projected pupil size (mm)	1.376	1.869
Total usable surface area ratio	93.6%	97.8%
Minimum illuminated lenslet	81%	61%

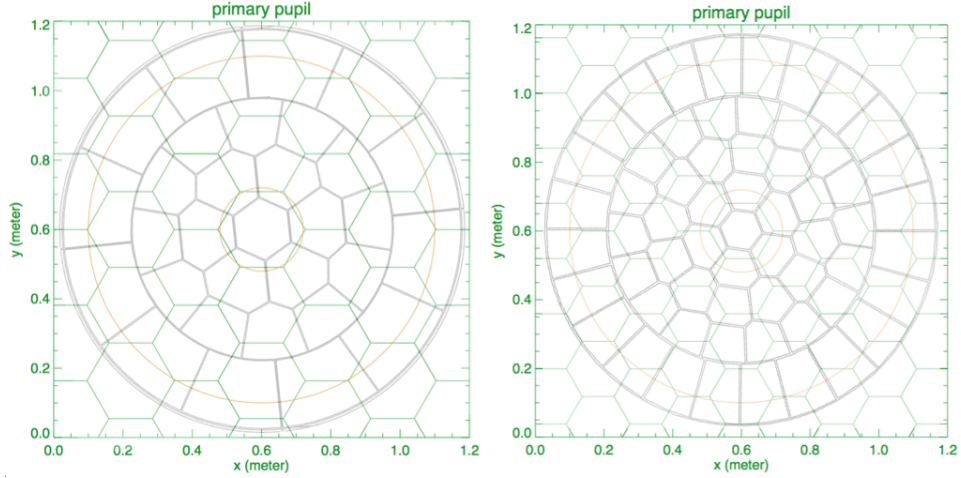**Table 4.1.** The two optimized projection of the pupil onto the hexagonal lenslet array

Figure 4.6. The DM devices (grey) are plotted over the two lenslet configurations (green). Left: 31-actuator device over 18-lenslet array. Right: 61-actuator over 36-lenslet array. The pupil of the telescope (orange) is also overplotted. Both panels are reprinted from Che et al. (2013).

shown in Figure 4.6 where the 18-lenslet array is overlapped with the Cilas 31 DM and the 36- lenslet array is overlapped with Cilas 61 DM.

4.3.2 Collimator

To project a re-imaged pupil with 1.87 mm diameter onto the lenslet array, an off-the-shelf f = 9 mm achromatic doublet (Edmund Optics # 45090) is used. We carried out a ZEMAX calculation including all optics up to the collimator: M1, M2, M3, M4, dichroic, the parabolic focusing mirror and the collimator, and found the peak-to-valley wavefront errors $\sim 1/10$ wave for two example wavelengths 600nm and 900nm as shown in Figure 4.7. This demonstrates this off-the-shelf doublet is good enough for our purpose. For the 1.38 mm re-imaged pupil, a customized doublet will be needed.

4.3.3 Re-imager

While the OKO lenslets has some excellent properties, the physical size is not optimal for imaging the spots onto the camera. The Shack-Hartmann spot size on the camera would be 2.7 pixel/FWHM without a re-imaging pair of lenses. Our simulation shows that a 1.5 pixel/FWHM spot is sufficient to recover wavefront information, and suffers
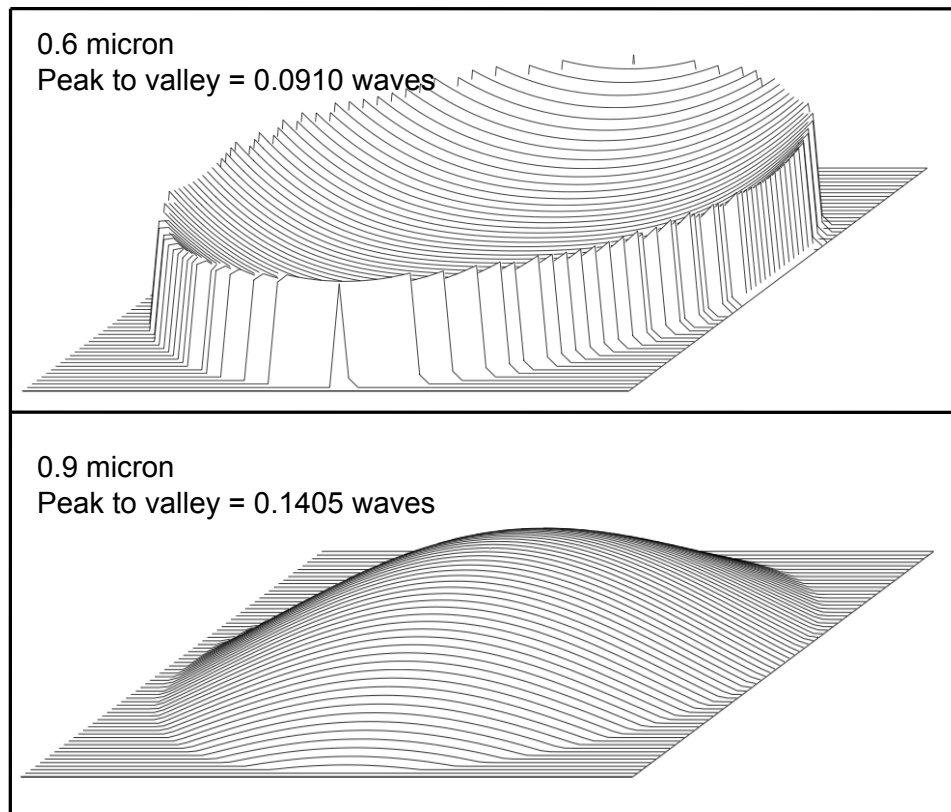
Figure 4.7. The wavefront errors from a telescope to the off-the-shelf collimator based on ZEMAX calculation. Both panels are reprinted from Che et al. (2013).
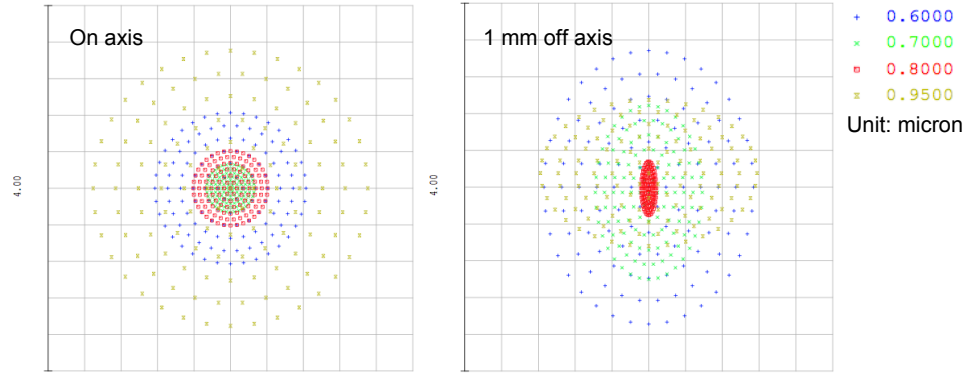
Figure 4.8. The diffraction-limited images produced by the re-imaging optics for wavelength from 600 to 950 nm. Both on-axis and the furthest off-axis spot images are shown. Both panels are reprinted from Che et al. (2013).

less detector noise. To keep the telecentric spots, a pair of re-imaging lenses is used to scale down the spot size. Two off-the-shelf achromatic doublets (Edmund Optics, #49306, #49309)are chosen with focal length of 35 mm and 20 mm. Both have visible anti-reflection coatings to increase the throughput. In this design, the entire pupil is sampled by 67×67 pixels and each subaperture has a field-of-view of 6.7", sufficient for control of bad seeing ($r_0 \sim 5$ cm) even for a feed-forward system.

Figure 4.8 shows the result of ray tracing the re-imaging optics. We calculated the image quality using ZEMAX ray-tracing and found the spot size is well within the $\sim$24 micron diffraction limit, even for the most extreme off-axis lenslet spots.

4.3.4 Camera

The choice of camera for this project is critical since the low-light noise performance sets the limiting magnitude for the AO system. Classical CCDs or the newer CMOS cameras are dominated by read noise with a nominal value of 3-4 e^-/pixel at the high frame rates needed for adaptive optics. An EMCCD is a better choice because it can amplify the signals through an avalanche-gain register readout, essentially operating with no read noise. The EMCCD suffers some drawbacks, such as root 2 higher Poisson noise when using high gain and Clock Induced Charge (CIC) noise that is indistinguishable from signals. In general, an EMCCD does not have an advantage over a classic CCD at high Signal to Noise Ratio (SNR), but is much more sensitive at

low SNR due to negligible read noise. It is worth noting that most EMCCDs do not have an adequate frame rate for adaptive optics on large telescopes but it is sufficient for CHARAs 1m aperture.

Specifically, we have decided on the Andor Ultra iXon 897. This new iXon model has <0.005 e^-/pixel clock induced charge and is capable of 1kHz frame rates for readout areas smaller than 90x90 pixels, which is sufficient for CHARA AO. Initial tests of actual hardware confirmed these specifications using just thermoelectric coolers. We chose the commercial standard high-speed Cameralink interface and carefully selected a low latency, Linux compatible PCI card (from EPIX). Since the main science targets after this upgrade are T-Tauri stars, which have red spectra, a camera with high Quantum Efficiency(QE) at longer wavelengths is preferred. One type of CCD with deep depletion technique fits this criteria well, unfortunately the CCD substrate was not available for EMCCDs such those used by Andor.

4.3.5 WFS Control Software

The control computer for the CHARA AO system is a PC running CentOS 6.3. This installation is compatible across many subsystems at CHARA and leverages experience in device drivers and software infrastructure. The computer hosts a PCI-based Cameralink card by EPIX that has low latency to access the Andor camera data even at highest frame rates.

The AO computer installation has the pre-emptive kernel patch that allows the system to provide real-time support for time-critical functions, such camera readout, centroid analysis, and signal output to DM electronics. This pre-emptive kernel patch has been tested to have <10 μs latency and is in use for several other CHARA subsystems.

4.3.6 Data Flow

The software follows a modular design, whereby multiple threads interact through shared memory to process the camera data at full frame rate with minimum latency. Here is the data flow:

1. A Cameralink/USB thread detects new data from PCI bus. This thread receives raw data from the camera and prepare it to be science ready, including bias subtraction, flat fielding, and software co-adding.

2. A WFS thread calculates the centroids from each new science frame. Next, the wavefront is estimated using Zernike modal analysis. The tip/tilt correction is sent to the tip/tilt mirror with appropriate gain. The rest higher order corrections is sent to a fast DM during Phase II AO.

3. The telemetry spooler is a low priority thread that can utilize time stamps, using the standard CHARA time base, to record wavefront telemetry for future data analysis and correlation with fringe data.

The WFS is modeled on our existing real time systems and follows a socket based client/server model. Both the server and client have been developed and tested.

4.4 Simulation

The simulation package is specifically designed for the CHARA AO project. It was developed independently using IDL language. A few assumptions are made in the simulation.

1. The background of the sky is about 18.5 (mag/arcsec^2), and is ignored because even our faintest targets are still much brighter.

2. No spectral dispersion is included. All photons are assumed to have wavelength of 0.7 micron, which is a compromise of the QE of the detector and relatively red spectra of our main science targets.

3. 4.2e9 photons/s received on the detector of the WFS for an R = 0 magnitude target. This takes into account the transmission loss from the primary mirror to the WFS detector.
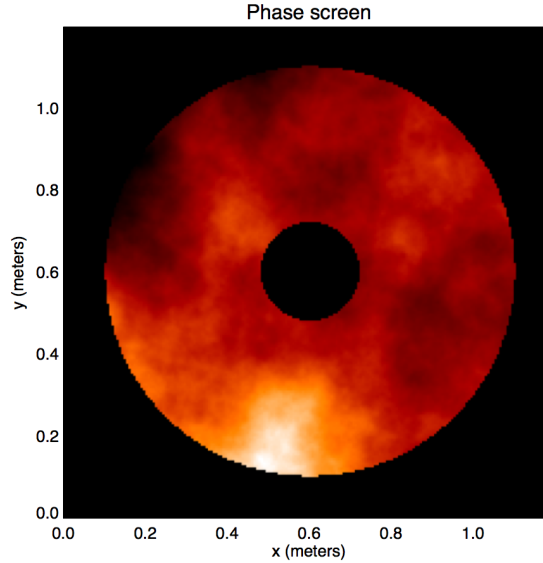
Figure 4.9. A snapshot of the modeled phase screen of the atmosphere above a single telescope. The figure is reprinted from Che et al. (2013).

4.4.1 Wavefront Simulation

The wavefront variation is caused by the atmospheric turbulence. We assume that the turbulence only affects the phases but not the intensities across the pupil and ignore scintillation. In reality, the turbulence could come from multiple layers. But in the simulation, we assume it comes from only two layers with different wind speeds. The turbulence in the simulation follows the Kolmogorov model where the power spectrum of the turbulence follows a power law with the exponent -11/3. A cutoff of the power spectrum is set at the outer scale of 30 meters. In the simulation, two different 30×30 meter big phase screens are created in advance for $r_{0,ref} = 5$ cm seeing conditions at $\lambda = 0.5$ micron, then each is scaled by $(\frac{r_0}{r_{0,ref}})^{5/6}$ to simulate a phase screen at r_0 seeing conditions. r_0 at the two layers could be different. Two little pieces of phase screens are extracted sequentially and respectively out of the two big ones, and added together as the inputs to the WFS to simulate winds blow over the aperture. An example phase screen is shown in Figure 4.9.

4.4.2 Detector Simulation

The parameters of the WFS detector in the simulation use those of Andor iXon Ultra 897, including all detector noises and quantum efficiency.

The dark current rate is 0.001 e^-/pix/sec. As the typical integration time is 1 to 100 milli-seconds the occurrence of the dark current is negligible in the simulation.

The read noise depends on the read-out rate. Assuming a 67×67 pixel array per frame and 1000 frames/s speed, the equivalent read out rate is about 4.5 MHz, which corresponds to $25e^-$ read out noise for this camera. Therefore a Gaussian distribution with a standard deviation of 25 e^- is used to simulate the read noise.

A high Electron Multiplier (EM) gain of the camera amplifies the real signals, but also shortens the lifetime of a detector. Also a high EM gain saturates the detector if the target is bright. So a high EM gain (1000) is only used for low light level, and decreases accordingly if the target gets brighter. The EM gain variation is simulated using an exponential distribution.

Since the real signals are mostly above the read noise background after the EM gain amplification, we can use a threshold to filter out the noise. A high threshold is preferred in terms of rejecting read noise. On the other hand, as the gain has a certain variation, some real photon signals are filtered out because they are below the threshold even amplified by the EM gain. Furthermore the higher the threshold, the higher the probability that the real photon signals are filtered out. So there is an optimal threshold that eliminates most of read noise and keeps most of real signals. In the simulation, we use threshold of 4× the RMS of read noise (typically 100e- for read noise RMS = 25 e^-), which only has a 3e-5 probability of a false signal and causes approximately 10% of the real photons to be rejected.

Another important detector noise is the Clocked Induced Charge (CIC). It mostly happens when moving the charges into the EM gain registers, which is just before the gain amplification. So the CIC noise is also amplified by the EM gain, and there is no way to tell a photon signal from CIC noise. The frequency of occurrence of CIC noise is 0.005/pixel for this camera. We simulate CIC noise using a Bernoulli process. This is the dominant noise at the lowest light levels. A simple study shows that even

when the signal is 4 times the CIC noise on average, there is still 27% chance that the number of electrons from CIC is equal to or greater than that from photons in a frame.

The Quantum Efficiency (QE) of the camera is the most red sensitive on the market for EMCCDs at the time of purchase. The QE is above 90% from 400 - 700 nm, and drops to 40% at 900nm. The QE is only used to calculate the number of photons received. After that we assume all photons have a single wavelength 0.7 micron as mentioned above.

4.4.3 Centroid Estimation

A 2-dimensional Gaussian fit may work better to find the centroid if there are enough photons. But for faint YSOs, we will be starved for photons most of time. Therefore a center of light algorithm is used to estimate the centroids for each subaperture:

$$Centroid = \frac{\sum n_i p_i}{\sum n_i > m},$$ (4.1)

where n_i is the number of photons for pixel i and p_i is the position. We fix the denominator to be m to reduce the estimated centroid offset if the total number of the photons is less than m. A fixed denominator can reduce the noise of centroid estimation when there are too few photons. In our simulation, we find m = 6 is an optimal value. For the Phase I AO upgrade, only a fast tip/tilt correction is implemented, we further weight the centroids of subapertures with their total photon numbers. Lastly, Hanning windows with size of 5×5 pixels (3.1" $\times$ 3.1") are used to filter out the noise that is far from the center of each subaperture.

4.4.4 Wavefront Reconstruction Algorithms

The mean slopes of the wavefront over each subaperture can be estimated from the differences between the computed centroids and reference centroids from a flat wavefront. Then the wavefront of the whole aperture can be reconstructed from the slopes. We explored two methods to reconstruct the wavefront: zonal or modal, and found modal method is consistently better than zonal method in our case. So we only

introduce the modal method.

In the modal method, we use the Zernike modes. The number of modes that are used to recover the wavefront depends on the number of sub-apertures. With too few modes, the reconstructed wavefront misses some high order information measured at the WFS; while with too many modes, the high order modes basically track the noise. We find the number of Zernike modes should be comparable to the number of the lenslets, and use 21 modes for 18-lenslet configuration and 36 modes for 36-lenslet configuration.

The reconstruction is done by solving a series of linear equations forming the matrix

$$A\alpha = \beta \tag{4.2}$$

where α is coefficients of modes and β is the mean slope estimated from each sub-aperture, A is the matrix that convert wavefronts of Zernike modes into slopes. Each row of matrix A can be computed by using one corresponding Zernike mode as an input and calculating the mean slopes of each subaperture. To solve for α, the matrix A needs to be inverted and this is not possible when A is not a square matrix. We therefore use Single Value Decomposition (SVD) to compute the pseudo-inversion of the matrix A. Finally the wavefront can be reconstructed by adding up all the Zernike modes with calculated coefficients.

4.4.5 Application to a Deformable Mirror

The reconstructed wavefront contains two parts: the tip/tilt component and the higher order Zernike components. The tip/tilt correction is passed to the secondary mirror of a CHARA telescope (Phase I AO), and the rest to a fast DM for a full AO correction (Phase II AO). In the simulation, we will show the performance of both. A simple tent-like DM model is used where the centers of segments of the DM can move up and down freely and the other parts of the segments just follow these centers in a linear manner. This DM model is very preliminary mainly because we don't have the proper influence function from the manufacture. Plus the DM will not be purchased until the funding for the second phase AO is allocated. At that time we

may have more options on suitable DMs that are available on the market. Therefore in the simulation we will use this linear interpolation model for the DM. We extract the phases of the reconstructed wavefront at the position of the centers of the DM, and then the full DM surface can be computed by linear interpolation for the rest part of the DM. A 2 ms lag is applied for the time between frame acquisition and DM correction.

The function used to calculate the DM correction is:

$$u_i = a_0 u_{i-1} + k d_i \qquad (4.3)$$

where u_i is actuator vector at time i, a_0 is the leaky integrator factor set to be 0.95, k is the loop gain, and d_i is the newly estimated residual actuator vector. The idea behind the loop gain is that applying the full correction to the DM may drive the servo loop to be unstable in closed loop operation, especially at low SNR. In the simulations, the loop gain value is typically close to 1 for good SNR and reduced to 0.1 for faint targets. The low loop gain value is equivalent to averaging over longer times. An example of wavefront correction is shown in Figure 4.10.

Although the piston term is not taken into account in the simulation, in reality it is important for interferometry. The AO system is insensitive to the atmospheric piston and will not be able to correct for it. In fact in interferometry, AO systems should avoid inducing a relative extra piston between telescopes. One way to reduce the induced piston is to monitor the DM corrections on each telescope and make sure the actuators stay around the mid range of their travel distance. As long as the induced relative piston is not significant compared to the atmospheric piston, the OPLE system will still be able to track the fringes.

4.4.6 Performance Simulation

In order to find the best DM and lenslet configuration for the CHARA Array, we run the simulations for a few different configurations. For instance, more sub-apertures will give better correction for bright targets in bad seeing, but this will compromise
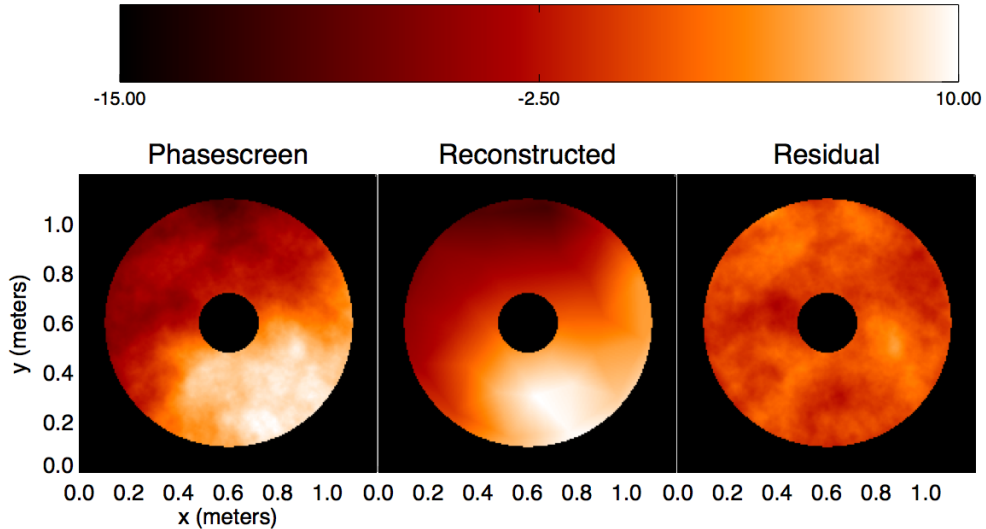
110

Figure 4.10. An example of wavefront reconstruction. The units for the color lookup table is in radian at 0.55micron. The figure is reprinted from Che et al. (2013).

	lenslet configuration	DM configuration
Configuration 1	18-lenslet	31-actuator
Configuration 2	36-lenslet	31-actuator
Configuration 3	36-lenslet	61-actuator

Table 4.2. The three configuration used in the simulations

the faint target tracking limits. Also, a 61-actuator DM version will perform better than a 31- actuator DM, but also costs more. The three configurations considered for detailed study are summarized in Table 4.2. In addition, two different seeing conditions at wavelength 0.5 micron are considered: effective r0 = 12 cm / t0 = 10 ms, and effective r0 = 6 cm / t0 = 2.3 ms. These two cases represent 80th and 20th percentile of summer seeing at Mt. Wilson.

The results are reported in two parameters: the traditional Strehl Ratio, and coupling into a single-mode fiber. Both of them are measured in H band.

4.4.7 Main Results

Figure 4.11 shows the main results of the performance studies. The AO system improves the light throughput significantly for bright targets, but barely for faint ones at R = 16 magnitude. Phase I AO (TT only) can improve the light throughout by a factor of up to 2.5 - 3 when coupling to a single-mode fiber in H band, and drop to half of that at R ∼ 15. Full AO correction can improve by a factor of 4 - 7, and
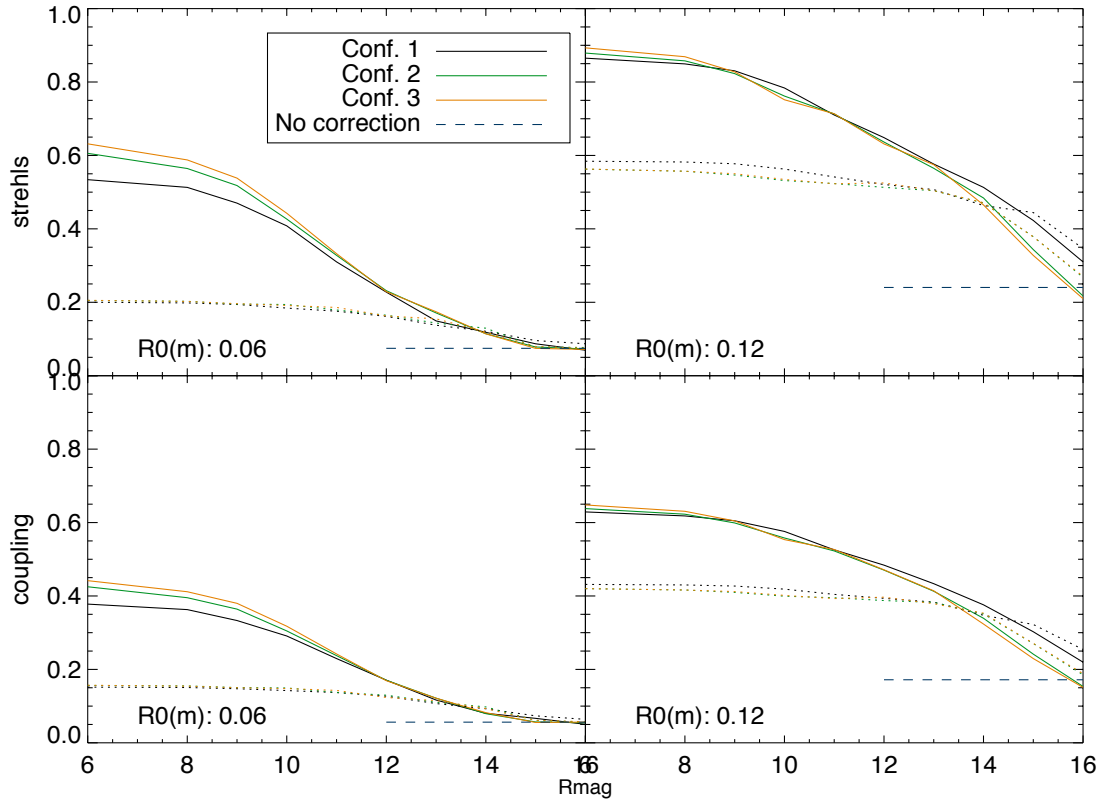
Figure 4.11. Final results of the simulations for a range of seeing conditions (measured at $\lambda = 0.5$ micron) and all three configurations. The solid lines represent full AO correction, and dotted lines tip/tilt correction. The strehls and coupling ratio are both measured in H band. All panels are reprinted from Che et al. (2013).

drops to half at R $\sim$ 12 for bad seeing and 14 for good seeing. The performance of 36-subaperture configuration is better than 18-subaperture configuration above Rmag = 12 mag especially during bad seeing, but slightly worse for very faint objects during good seeing. The improvement in Strehl ratio is marginal when using 61-actuator DM compared to the 31-actuator.

4.5   On-Sky Commissioning Results

We had two WFS commissioning runs in 2013 October and 2014 January to test both the hardware and software of the system.

The WFS was tested on sky and successfully locked stars. The procedure was a little different from the design because the beacon system which was supposed to be used to mark the reference centroids was not well aligned with the telescope. So we

used a bright star that could fill the hole on the acquisition mirror as seen on the acquisition camera. By balancing the light around the edge of the hole, we assumed the star was on the axis of the WFS and recorded the reference centroids on the detector. Since the pattern of the reference centroids only depends on the relative position of a star to the hole on the acquisition mirror, stars on any part of the sky once locked would be forced to stay on the axis of the WFS. This method worked well and will be the approach to mark reference centroids before the beacon system come online.

The sensitivity of the WFS was tested and met the design. The WFS was able to lock a star with Rmag = 11.88 using a bare glass which reflects only 4% of light into WFS. The exposure time and gain of the camera were set to be 0.1s and 1000. To compute the number of photons that was received by the detector, we record images of sky background with the same camera settings. Then assuming photon counting mode, we subtract the number of counts in sky background from that with the star in it to get 580 photons from the star per 0.1s (Figure 4.12). This value roughly agrees with the theoretical value of number of photons that should be received by the system. Therefore if instead of the bare glass, a dichroic that reflects all the visible light is used, the WFS will be able to lock a star with Rmag = 15.5 at least, which meets the design.

Another way of estimating how much the WFS has improved over the current TT system is to compare the number of photons received by the WFS and that received by the current TT system. We took data with both WFS and TT sensor simultaneously while a star was locked, and then counted the number of photons on both systems. The WFS received 33 times more of photons than the TT sensor, which agrees with the prediction.

The image quality using the beacon and a star is also diagnosed. The designed Full Width Half Maximum (FWHM) is 1.5 pixels, however the measured FWHM with the beacon was 2.14 pixel (Figure 4.13). One reason is that when the CCD is in fast read out mode, the images are elongated in x dimension. But this larger FWHM does not seem to impact the functionality of the WFS.
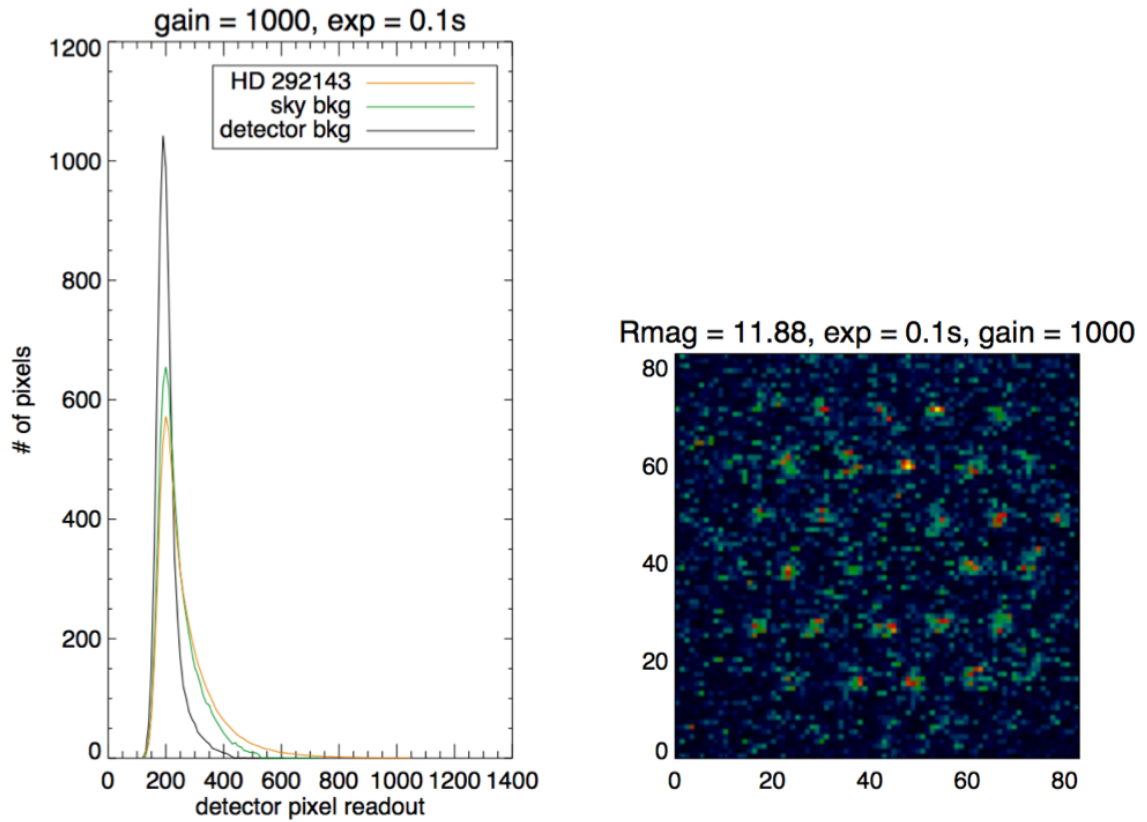
Figure 4.12. On sky sensitivity test of WFS. The target is HD 292143, the Rmag = 11.88 (Simbad). The camera settings are: exposure = 0.1s, gain = 1000. Left: the histogram comparison of ADU counts above certain threshold under three conditions: detector background, sky background and on object. Right: a recorded CCD frame on the target. There are 36 separated areas of positive detections in the image, each corresponding to a stellar image from a lenslet.
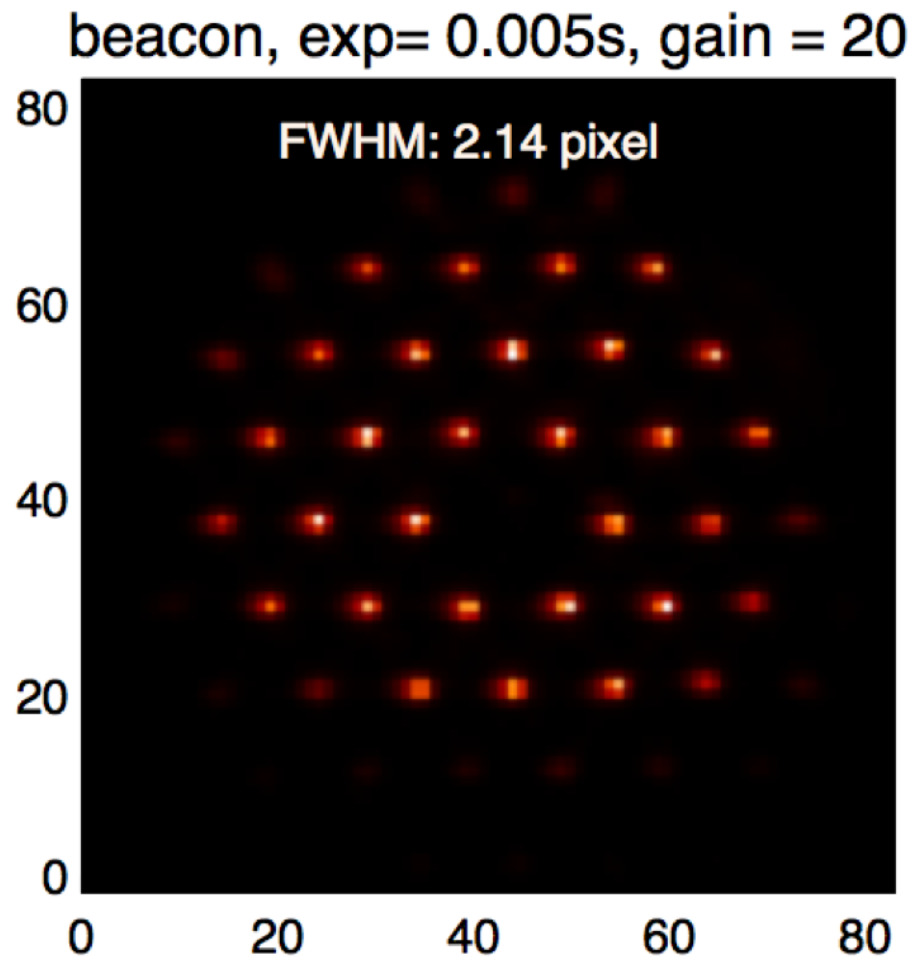
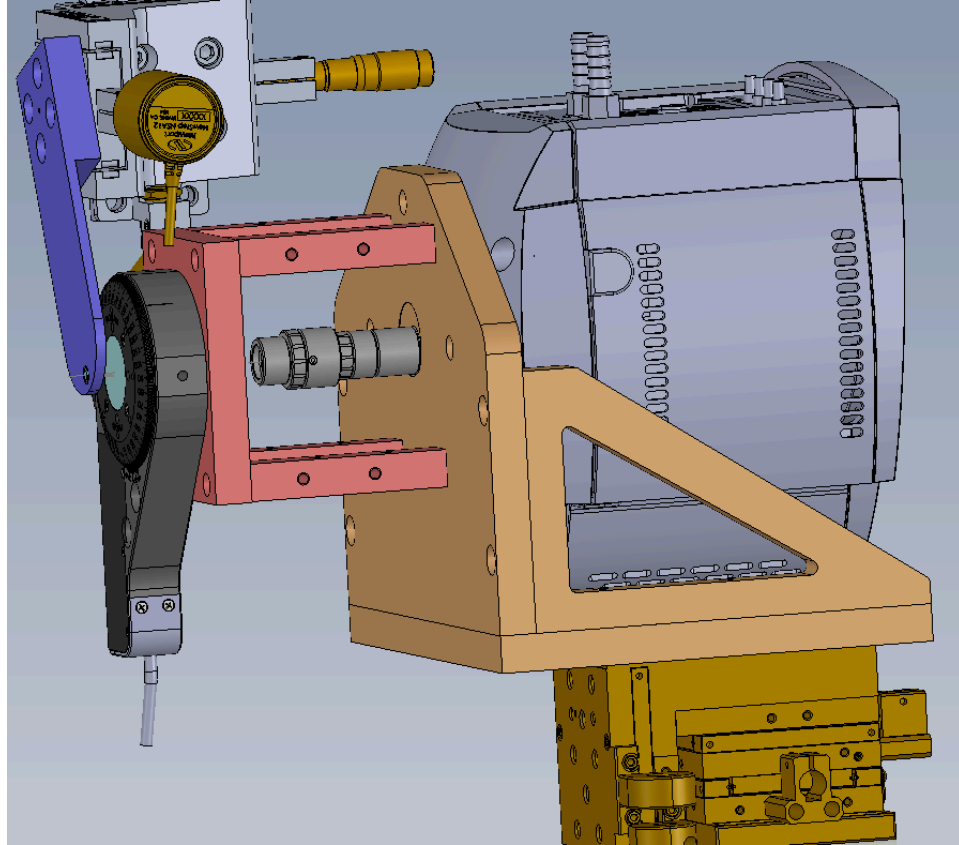**Figure 4.13.** A recorded CCD frame of beacon source.

Figure 4.14. The revised design of WFS. The arm that holds the collimator is shorter and broader to increase the stability.

During the commissioning run, we also discovered issues. One of them is that the mechanical part that holds the collimator is too thin and long, making it less stable. In the next version of the WFS, we have made the mechanical part short and thick (Figure 4.14). Also we modified the design of some plates to lower the position of the center of the weight to make the whole system more stable. The baseplate of the WFS is also changed to include some rotation and shift mechanism so that the whole WFS can be more easily align to the Optical Feed System.

CHAPTER 5

Future Possible Upgrades

CHARA/ MIRC have served as a productive combination of instruments to image and model nearby stellar objects. With the longest baselines of optical interferometry at the CHARA array and unique imaging ability of the 6-beam combiner MIRC, many interesting targets have been studied. This thesis includes examples of studies on two rapidly rotating stars α Leo and β Cas and a Be binary stars δ Sco . The sub-miliarcsecond angular resolution of CHARA/MIRC has resolved not only the stellar surfaces, but also the gaseous circumstellar disks. This allows us to model the geometry and intensity distribution of the objects, and further reveal the physics behind.

However the limited sensitivity has prevented CHARA and MIRC from studying more interesting but fainter objects. Further upgrades on the CHARA array and MIRC are necessary to broaden the target pool and deepen the science implication.

The sensitivity of the CHARA telescopes is limited mainly by the tiptilt system due to low photon efficiency in the optical system. To resolve the issue, the CHARA on-telescope Adaptive Optics (AO) project has been proposed and carried out. Currently the AO project is only funded for Phase I, which includes a fast on-telescope Wavefront Sensor (WFS) to measure the atmospheric aberrations. The secondary mirror on the telescope closes the loop with the WFS to correct for the tiptilt aberrations from the atmosphere. The measurements of the high order atmospheric aberrations will be sent to a small Deformable Mirror (DM) in the Beam Combiner Lab, forming an open loop AO system. Since the correction is made after the aberration is measured, there is no feedback of the performance of the correction.

To further improve the performance and fully exploit the benefits of the AO

system, a large DM will be purchased and installed on telescope to close the loop with the WFS to correct for the high order aberrations during Phase II. The current AO system including the hardware and software has been designed to be ready for the Phase II upgrade. The large DM will replace the M4 mirror (see Figure 4. in Che et al., 2013) which is located right before the WFS. The rest of the optics will remain the same. The control software of WFS is already able to analyze incoming wavefronts and measure high order aberrations, which will be sent to the large DM on the telescope instead of the small DM in the lab during Phase II.

The upgrade will make several science goals possible to the CHARA array and its combiners. The most important one is to image and model the inner disks of many more YSOs in NIR. The sensitivity of the current CHARA telescopes is limited to 12 magnitudes in R band, the Phase I AO upgrade improves 3.5 magnitudes and the Phase II AO will improve additional 1 magnitudes for bright objects. Therefore several times more YSOs will be within the sensitivity limit and allows us to perform a statistics analysis of disk morphology and evolution. Other benefits include that the upgrade will enable a few new types of objects (AGN, microquasars) to be observable with the CHARA array for the first time. The upgrade will also improve the data quality for bright targets by maintaining consistent image qualities under different seeing conditions.

MIRC has been upgraded with Photometric Channels to reduce the uncertainties on V^2 measurements from 10% to 2-3%, and that of closures phases to ~ 1 degree. With the better calibration, MIRC is able to improve the precision of science results, and reveal subtle phenomena that were overwhelmed by noises before the upgrade. For example, MIRC has detected a faint object orbiting around a star that used to be a good calibrator. MIRC has also been expanded from a 4-beam combiner to a 6-beam combiner, which greatly improves the (u,v) coverage of a single snapshot. The better (u,v) coverage allows MIRC to image and model more complicated stellar systems, such as circumstellar disks and spotted stars.

However the sensitivity of MIRC is limited due to the all-in-one feature and the spatially filtering using single model fibers. Right now the H band sensitivity is 6

magnitudes under good seeing condition, allowing only a few of the brightest YSOs to be observable. To take advantage of the CHARA AO upgrade and follow its key science goal of imaging YSOs, MIRC is seeking for an upgrade of replacing its detector. The current PICNIC detector has readnoise of $\sim 15\ e^-$, which is the dominated noise when observing faint objects. The new versions of scientific cameras can suppress readnoise to $\sim 1\ e^-$, which will improve the sensitivity of MIRC by 3 magnitudes. Consequently MIRC will be able to image several new kinds of objects including the hot inner disks of YSOs.

MIRC has exploited the full ability of the CHARA 6 telescopes and demonstrated the unique imaging ability. However, the range of baselines at CHARA is fixed to 30 - 330 meters, which sets the optimal angular sizes of objects that can be studied by MIRC to be ~ 1.5 - 4 milli-arcsecond (mas). Within this size range, the number of interesting objects is limited. For example, only a handful of rapidly rotating stars have angular sizes larger than 1.5 mas , and most of them have already been studied by MIRC. In order to resolve even smaller objects, new telescopes which form longer baselines with the current CHARA telescopes might be installed in the future. The number of objects within the new angular resolution will increase dramatically with the lengths of baselines at the CHARA array.

MIRC operates in near infrared (H and K bands). A visible version of MIRC is being developed at Navy Precision Optical Interferometer (NPOI). The Visible Imaging System for Interferometric Observations at NPOI (VISION) combines beams from 6 telescopes, and uses single-mode fibers to filter out atmospheric turbulence. It is also an image-plane all-in-one combiner. Although VISION operates at the visible band, the angular resolution is worse than MIRC because of its short baselines: the range of the current baselines is up to 79 meters. And the sensitivity of VISION is limited due to its small aperture size 15 cm. Big upgrades such as larger aperture sizes and longer baselines are planned, and promise better performance of VISION in the future.

In summary, this thesis has illustrated that the high angular resolution from optical interferometry can provide unique spatial information, and is essential to study

stellar systems. The upgrades carried out on MIRC have improved the performance of the combiner, allowing better imaging on more complicated objects. The current and future sensitivity upgrades on both CHARA and MIRC will allow a wide range of interesting but fainter objects to be observable, and contribute to new astronomical fields.

APPENDIX A

MIRC Photometric Channels Upgrade

The work of this chapter has been published (Che et al., 2010), much of the content has been extracted from the paper.

A.1 Photometric Channels

A.1.1 Motivation and Overview

MIRC used indirect methods of measuring fluxes from individual telescopes. Although these methods have revealed interesting and profound science about stars, they result in large uncertainties ($\sim 10\%$) in visibility measurements, which allow stellar model parameters to vary in a large range. Consequently the ability of MIRC is limited in exploring deeper and broader area of astrophysics, such as detecting exoplanets. One way to increases the precision of flux measurement is to directly monitor the beams from each telescope in real time. Coudé du Foresto et al. Coudé du Foresto et al. (1997) first proposed the idea of measuring photometric outputs from each beam to fully take advantage of single-mode fiber interferometer. We carried out this idea in our design as Photometric Channels (PCs). With this improvement, the data with improved quality will make a significant difference in model fitting to reveal important but subtle effects. The upgraded MIRC system promises to do more accurate and precise science on stars.

The main idea of PCs is expressed by the schematic drawing in Figure A.1. The beams that come from telescopes are focused into individual single mode fibers. The beams are placed in a line with non-redundant spacing between them. The beams are then collimated by a MIRC microlens array and then reflected by a spherical

mirror to interfere with each other. PCs insert a beamsplitter right after the MIRC microlens array and before the beams interfere with each other. The beamsplitter reflects part of the beams, which get focused by PCs microlens array into multimode fibers. The beams coming out of the other ends of the fibers are reflected by a mirror so that the virtual images of beams are located exactly in the image plane of the detector. The PCs beams and interference beams are then collimated and dispersed by the existing MIRC lens and prisms, and then detected at different quadrants of the same detector. In this way, we measure scientific fringes and fluxes from each telescope simultaneously in real time, hence increasing the precision of visibility and close phase.

PCs can be divided into two parts. The first part is located close to MIRC microlens array, containing beamsplitter, microlens array and one end of the multimode fibers. Their main function is to collect photons from individual beams. The second part is located at the image plane of the detector, including a mirror and the other ends of the fibers. They are designed to inject as much flux as possible into MIRC optics.

A.1.2 Detailed Design

One critical property of beamsplitter is the reflection ratio. We do not want to reflect too much light because it will lower the sensitivity of detecting scientific fringes; neither do we want the other extreme because the photon noise of PCs beams will dominate in visibility calibration. A reasonable balance is that the peak intensities in the fringe and PCs quadrants are similar so that neither will saturate before the other one. A rough estimation of the FWHM of the fringes is 1300 micron, and that of PCs is 50 micron. And since the 4 beams are overlapped in the fringe quadrant while the PCs are separated on different pixels, ideally the peak intensities in the two quadrants will be equal if we set the ratio of transmission over reflection to be 6.5:1. For the future MIRC 6T upgrade, the FWHM of the fringes will increase because we will use a spherical mirror with longer focal length (See Appendix B), but the number of overlapped beams will also increase to 6, so the ratio to keep the peak
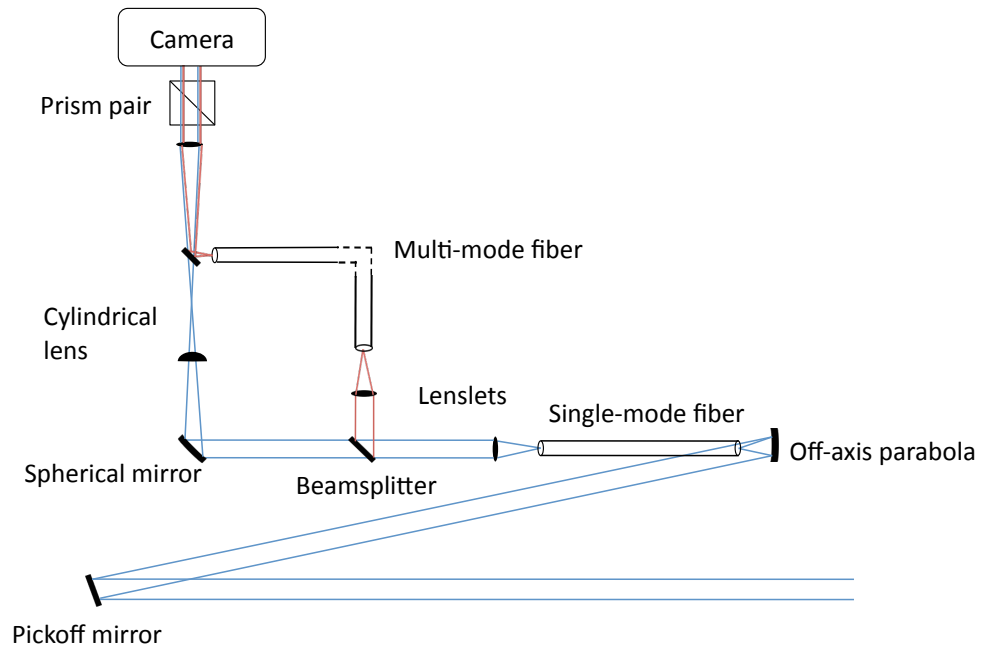
Figure A.1. The schematic drawing shows the path of one beam of Photometric Channels (PCs). The blue and red lines represents the beam path. The blue traces the existing MIRC, and the red PCs . The beam collected by a telescope is focused into a single-mode fiber by an off-axis parabola mirror, and then collimated by the MIRC microlens array. The collimated beam is then reflected by a spherical mirror and interferes with other beams. The cylindrical lens is used to compress the beam in one dimension, which is later dispersed by a prism pair. PCs system places a beamsplitter on the path of the collimated beam to partially reflect the science beam. The reflected beam is focused into a multimode fiber by the PCs microlens array. At the other end of the multimode fiber, the PCs beam is reflected by a mirror, and then goes through the same optics systems as the science beam.

intensities of the two quadrants equal is still close to 6.5:1. However in reality we expect some flux loss of PCs beams for three reasons. Firstly, part of PCs beams will miss the PCs microlens array after coming out of the MIRC microlens array because the size of collimated beams grows as they propagate. Secondly, there will always be some loss focusing beams into fibers. Thirdly, the optics of MIRC is optimized for interference beams, which causes vignetting of PCs beams because of a clearance issue. Because of these concerns, we increase the ratio transmission / reflection ~ 3. Therefore the beamsplitter will have a reflection ratio about 25%.

The location of beamsplitter is also a critical issue. The beam from a single mode fiber is nearly gaussian. Diffraction causes the beams to spread transversely as they propagate, shown in the left panel of Figure A.2. The diameter of the MIRC microlens is $240\mu m$, as is the PCs microlens. As the diameter of the beam expands, when it hits the PCs microlens array, the outer part of the beam will miss the microlens. The loss is shown in the right panel of Figure A.2. One will find that about 50% of the flux will not hit the target microlens when it is only 40 mm away from the MIRC microlens array. This strongly requires us to bring the beamsplitter and PCs microlens array as close to MIRC microlens array as possible.

The PCs microlens array is chosen to have the same pitch (the distance between adjacent microlens) as MIRC microlens array so that all beams can be focused into multimode fibers at the same time. Smaller numerical aperture (NA) or larger f-ratio of the lens array is preferred because it allows more tolerance on aligning the array and multimode fibers. Plus smaller NA injection at one end of the multimode fibers means smaller diverging angle at the other end of the fibers, which assures more fluxes hit the MIRC achromatic doublet. The size of the microlens array is limited for two reasons. First, the array plane and the beamsplitter plane form a 45 degree angle (Figure A.1), in order to put them as close as possible, the width of the array has to be small. And technically only one line of lens will be enough to focus the beams from MIRC. Second, the beams from MIRC form a line with non-redundant spacing, so the distance between the top and bottom beams is much larger than if they were placed next to each other. In addition, we need to reserve extra spacing

for upgrading to a six-beam combiner in the future. So the length of the array has a lower limit of 5.25 mm. Additionally, we need some edges to hold the array.

We bought the PCs microlens array from SUSS with part #13-1502-100-000. It is made of fused Silica with pitch = $250 \mu m$, NA = 0.07. The focal length from the back surface is about 1mm. The original size is 10mm × 10mm × 1.2mm which is too large to be placed close to the beamsplitter. So we cut it in half, which is 10mm × 5mm × 1.2mm. The array is then anti-reflection coated to transmit more light.

Multimode fibers with large core size (diameter = $50\ \mu m$) are adopted so that the image of a star will be much smaller than the cores of fibers, which eases alignment of microlens array and multimode fibers. The wavefront may be distorted going through multimode fibers, but in PCs we only care about the flux. The fibers are secured in a silicon v-groove in a line with pitch = $250\ \mu m$ to match the microlens array. In order to place the fibers 1mm away from the microlens array, we build a v-groove holder with two antenna extending 1mm away from the end of fibers as a reference (see Figure A.3).

We would rather not alter or move any parts of MIRC because it has already been mounted and aligned. As a result, there is very limited room for PCs . We could not find available commercial optics holders or linear and rotation stages to align beamsplitter, microlens array and fibers because of limited room. So in the end we had to design and make several little metal pieces holding them as shown in Figure A.3, and use shims to adjust their relative positions for alignment. In this design, we manage to limit the light path between two microlens arrays to be about 30 mm. To align these components with the MIRC beams, a translating stage is constructed with five degrees of freedom (two rotation and three linear dimensions).

We needed to achieve two goals for the other end of the multimode fibers: placing the ends the fibers exactly in the image plane of the detector and maximizing fluxes entering the MIRC optics system. The first goal can not be achieved directly because of clearance issue. Instead we place a small mirror at the end of fibers to reflect the beams into the MIRC optics so that the virtual images of the four fiber ends are located exactly in the image plane of the detector. The second goal can be obtained
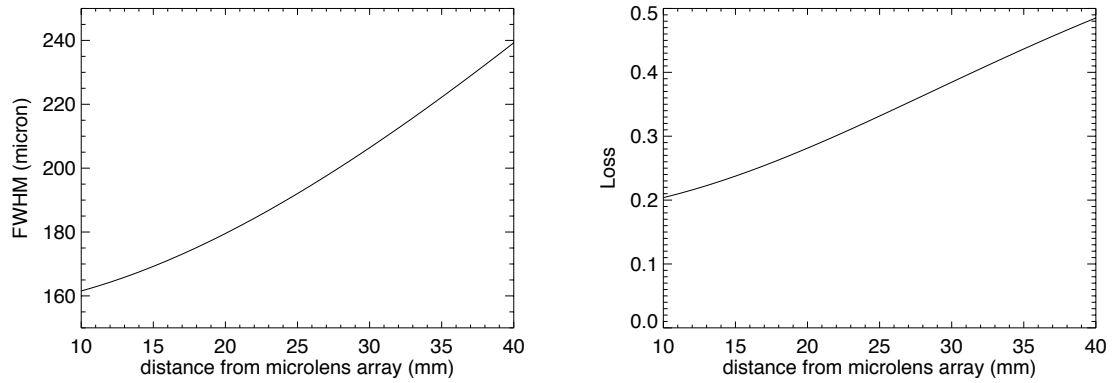
Figure A.2. The left panel shows Full Width Half Maximum (FWHM) of the beam as it propagates away from the MIRC microlens array (the diameter of microlens is $240\mu m$). The right panels shows the loss of flux due to the outer part of the beam missing the PCs microlens array (diameter is also $240\mu m$) Both panels are reprinted from Che et al. (2010).
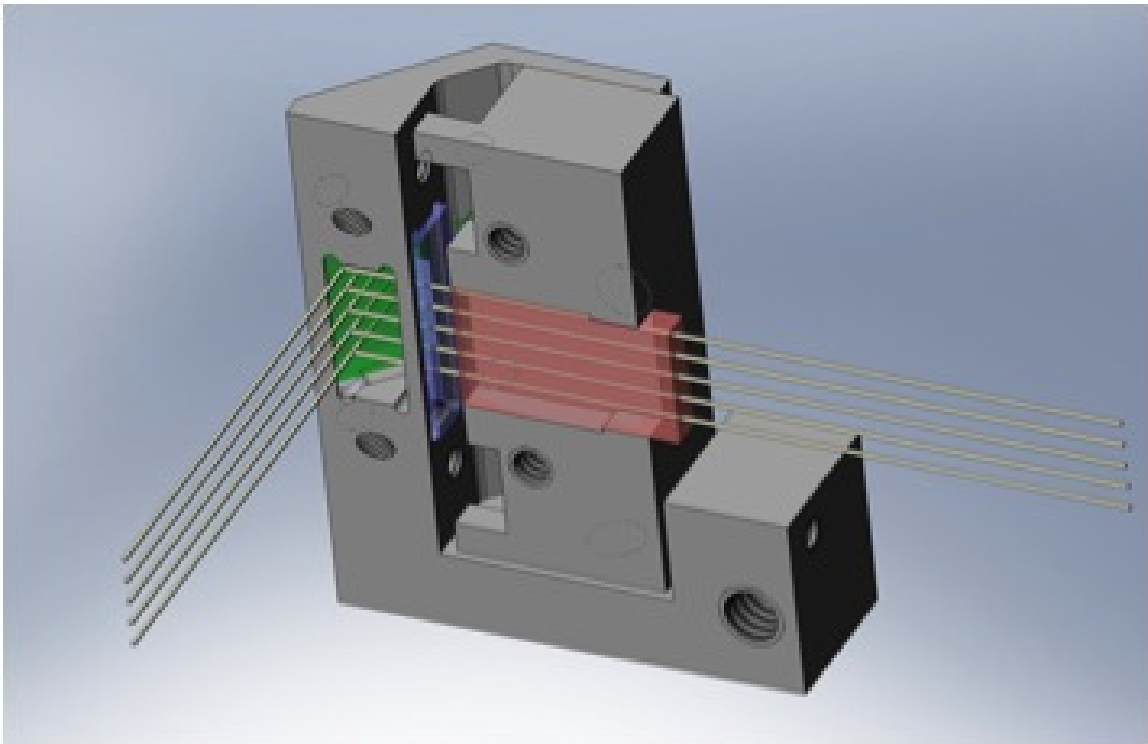

Figure A.3. Solidworks drawing of the essential part of the PCs module we design. The lines represents the beams. The green part is the beamsplitter, reflecting part of the light into PCs ; the blue part is microlens array focusing reflected light into fibers; the red part is the v-groove holding fibers. The piece holding v-groove has two extended antennas at the top and bottom, which serve as a reference to keep the distance of the microlens array and fibers at 1mm. The figure is reprinted from Che et al. (2010).
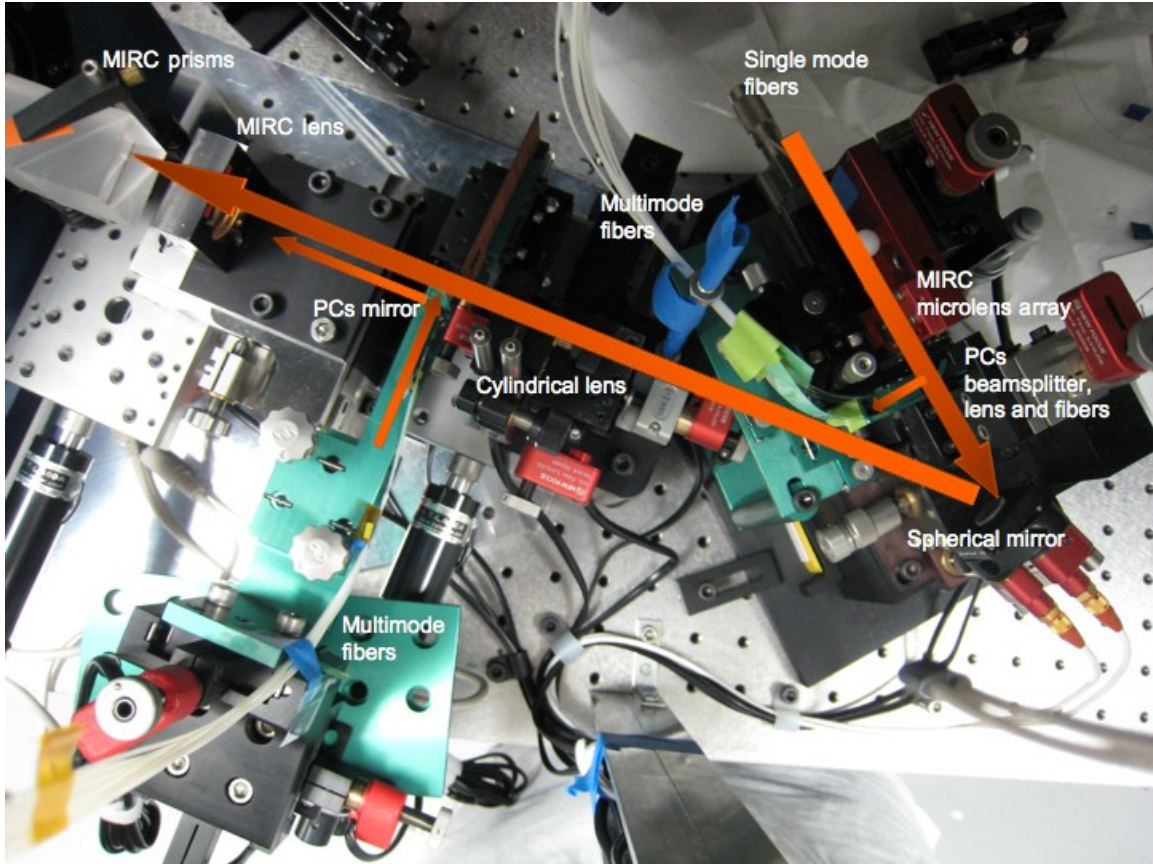
Figure A.4. A top view of PCs which includes all green parts and the components on top of them. The green parts on the right side are the beamsplitter and microlens array (not visible); on left side there is a little mirror and translation stages; the bunch of white lines are multimode fibers. The thick arrows show the MIRC beam flow; and thin arrows show the PCs beam flow. The thin arrow on right hand side is connected to the arrow on left hand side by the multimode fibers. The figure is reprinted from Che et al. (2010).

by using translation stages (linear and rotational) to finely adjust the beam direction while maintaining that the virtual images remain in the image plane. The real image of the whole system is shown in Figure A.4.

A.2   Commissioning Results

The first observation of MIRC with PCs was carried out during August 2010. To see whether PCs helps improve MIRC data quality we compare the visibility data of the same target 37 And (calibrated by 7 And) observed at the same time, as shown in Figure A.5. The four panels show the calibrated visibilities from four different
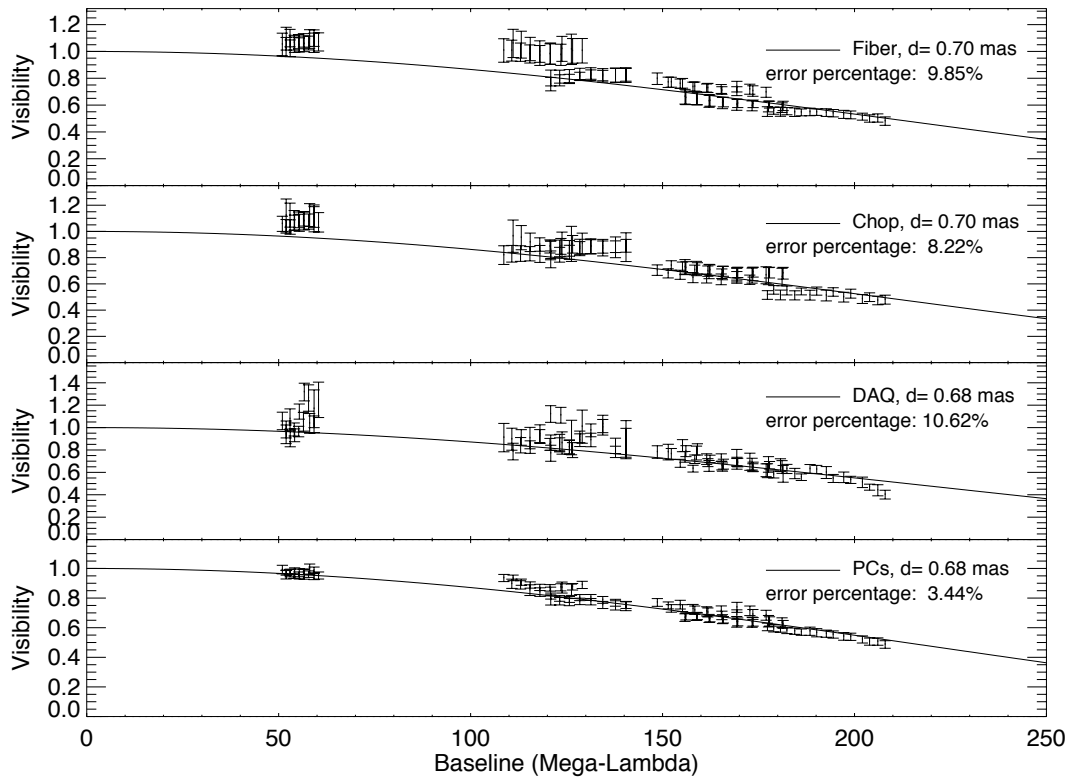
Figure A.5. The figure shows the comparison of calibrated visibilities from four different methods (the bottom one is from Photometric Channels). The data is from CHARA-MIRC observation of 37 And on Aug 24th 2010. The size of 37 And calculated from photometric methods gives range 0.676 - 0.688 Kervella & Fouqué (2008); Barnes et al. (1978). In the figures, the solid lines are the best uniform disk fitting results, and 'd' is the estimated diameter from these methods. The figure is reprinted from Che et al. (2010).

methods, of which the top three are methods we used to use, the bottom one is from PCs . The solid lines are the best fitting results from uniform disk models, 'd' is the estimated diameter from these methods, 'error percentage' is the ratio of standard deviation and fitted data. Visibility calibration with PCs method is more precise, the error percentage of visibilities is reduced to about 1/3 for most of the data. We further find that the diameter of 37 And is from 0.676 - 0.688 Kervella & Fouqué (2008); Barnes et al. (1978). In this case the diameter estimated from Fiber and Chop is a little off, while DAQ method is as good as PCs . Figure A.6 shows the comparison of calibrated visibilities from a science target observed by MIRC on one night. Visibilities calibrated by Photometric Channels have much higher quality than the other method, allowing a more precise study on the target.
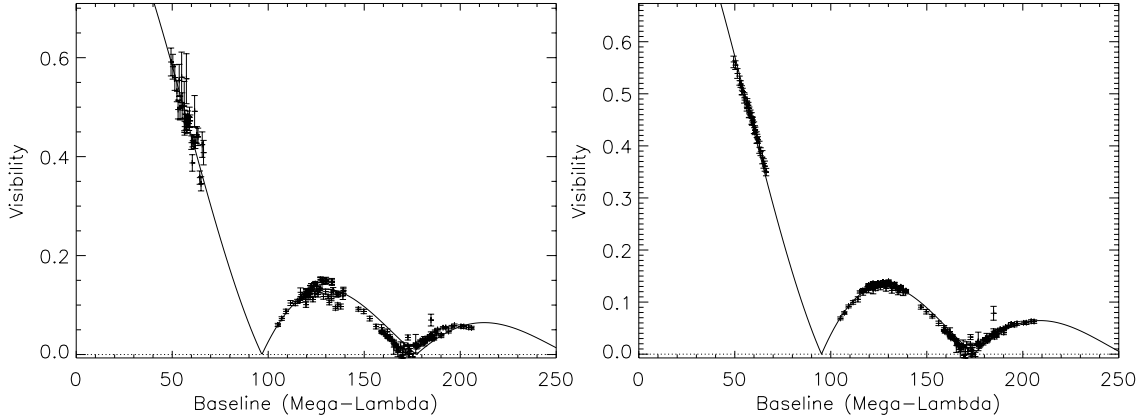
Figure A.6. The figure shows the comparison of calibrated visibilities from a real target. Left panel shows the visibility calibrated by the DAQ method which is one of the previous methods we have been using. The right panel shows the visibility calibrated by Photometric Channels. The figures are reprinted from Che et al. (2010).

A.3 Unresolved Problems and Future Plan

One problem we noticed but haven't totally solved is the polarization effect of the beamsplitter. Light from most stars is unpolarized. However after being reflected by the mirrors at CHARA, the beams are partially polarized when they reach MIRC combiner. The beam splitter we ordered has different reflection ratios for two orthogonal polarizations: one is about 40% and the other is about 10%. If the incoming light of MIRC is polarized and the polarization changes with time because the CHARA mirrors rotates to track targets, then the flux ratio between PCs and MIRC beams will vary with time. Figure A.7 shows the flux ratios of all targets observed during one night. Obviously the ratio is not constant. We tried to explore the cause of the inconstancy and eventually found it was only related to azimuthal angle and elevation. Figure A.7 shows a linear fitting of flux ratio as a function of azimuthal angle and elevation. We point out here that the relation is not necessarily linear, a detailed modeling of CHARA mirrors and the beamsplitter is required to find out the true relation in the future. But for now, we will take a shorter shutter data sequence to calibrate the flux ratio since there is only a trivial change in flux ratio in a short time period for the same object. On the other hand, our data suggests that CHARA beams are about 25% linearly polarized at 1.65 μm, much higher than we expect
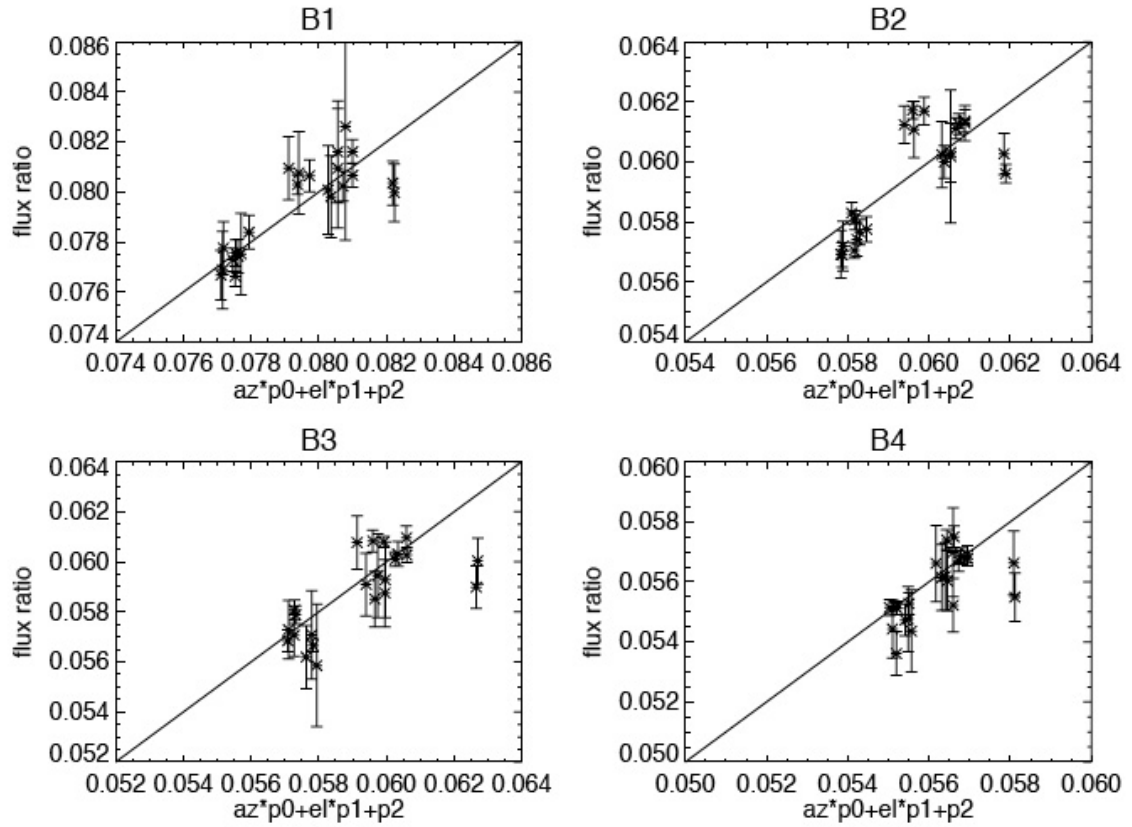
Figure A.7. The figure shows that PCs and MIRC flux ratio is related to azimuthal angle and elevation. Each star stands for one target, all targets are observed in one night. Four panels are for four beams of MIRC. The y axis is the flux ratio between PCs and MIRC, the x axis is the fitting result of the flux ratio as a linear function of azimuthal angle and elevation (the unit is arbitrary). The figures are reprinted from Che et al. (2010).

based on properties of aluminum coatings and the few silver coatings in the beam train. This high birefringence is under investigation.

Another problem with this design is that the beamsplitter, microlens array and multimode fibers are not well aligned. As one can see in Figure A.7, the flux ratio between PCs and MIRC is about 0.06, as opposed to the expected value 1/3. We believe that the reason we are losing too much light on PCs is because our injection into the multimode fibers is not correctly aligned due to the difficulty in holding and aligning the fibers and microlens array precisely with our home-made mount. This problem is solved in the second version of PCs during the MIRC 6T upgrade (See Appendix B).

APPENDIX B

MIRC 6-beam Upgrade

The work of this chapter has been published (Che et al., 2012a), much of the content has been extracted from the paper.

B.1   MIRC SIX-BEAM COMBINER UPGRADE

B.1.1   Motivation

MIRC was first assembled as a four-beam as phase one in 2005, but reserved the capability of expanding to a six-beam combiner. During the 5 years of 4-beam MIRC operation, we found that although MIRC was already a state-of-the-art multiple-beam optical combiner, we still needed to switch the 4 telescope combinations out of 6 telescopes during the observations to optimize the (u,v) coverage. The switch not only took time, also complicated the observation plans. And it was not practical for some kinds of targets. For instance, variable stars with periods of hours require as much (u,v) coverage as possible at one single snapshot.

Also MIRC was designed to perform true interferometric imaging which requires as much (u,v) coverage as possible. Adding two more beams to the MIRC combiner expands the (u,v) coverage by a factor of 2.5, and recovers 3 more times of phase information, which is crucial to imaging.

B.1.2   Design

The extension from a 4-beam combiner to a 6-beam combiner is completed by adding two additional stages "B5" and "B6" (Figure B.1) on the beam paths of the remaining two telescopes. The spaces for the new stages were reserved without disturbing the optics of the existing four beams. The two new beams follow the paths parallel to the

other four beams and are focused into two reserved single-mode fibers from the same v-groove as the other beams. The fibers in v-groove are arranged in a linear non-redundant pattern so that fringes from each pair have a unique spacial frequency that can be picked out later during the data reduction pipeline. We use the same v-groove as the 4-beam MIRC, but pick different fibers as shown in Figure B.2 Beam 1,2 and 3 are the same as before to minimize the work of re-aligning the fibers and optics. The new distances of neighboring pairs are 2-6-5-4-3 separations (one separation is 250 microns).

The 6 beams coming out of the single-mode fibers are collimated by the same micro-lens array used in 4-beam MIRC (Figure B.3). Then the beams are focused to interfere with each other in the image of the detector by a longer focal length spherical mirror to maintain the Nyquist sampling of fringes on the detector due to larger fiber separations. The new spherical mirror has focal length of 375mm. For a similar reason to keep the Point Spread Function (PSF) around 1 pixel at the image plane in one dimension, we replaced the cylindrical lens with the one with longer focal length. The new cylindrical lens is made of CaF2 with focal length of 30mm.

The optics after cylindrical lens are kept the same as before. Since the image plane (where the slit is in Figure B.3) of the detector is at the same position, the new cylindrical lens and the whole stage holding the new spherical mirror ("Focusing Optics" in Figure B.3) had to recede away from the slit in the line of sight from the detector to the slit. This creates more room in between the spherical mirror and cylindrical lens, which is important for the PCs design as will be mentioned below.

B.2 Photometric Channels

The first version of PCs was implemented in 2009 (Che et al., 2010) as described in Appendix A, and it was able to reduce the visibility errors from $\sim 10\%$ to 3.4%. However the subsystem was not optimized because the adjustment of the beamsplitter was too coarse in the design, which caused the angle that the reflected beams shot into the multimode fibers to be slightly off. As the shooting angle is very sensitive to the coupling of the light and the fibers, a large fraction of the light was lost. Another
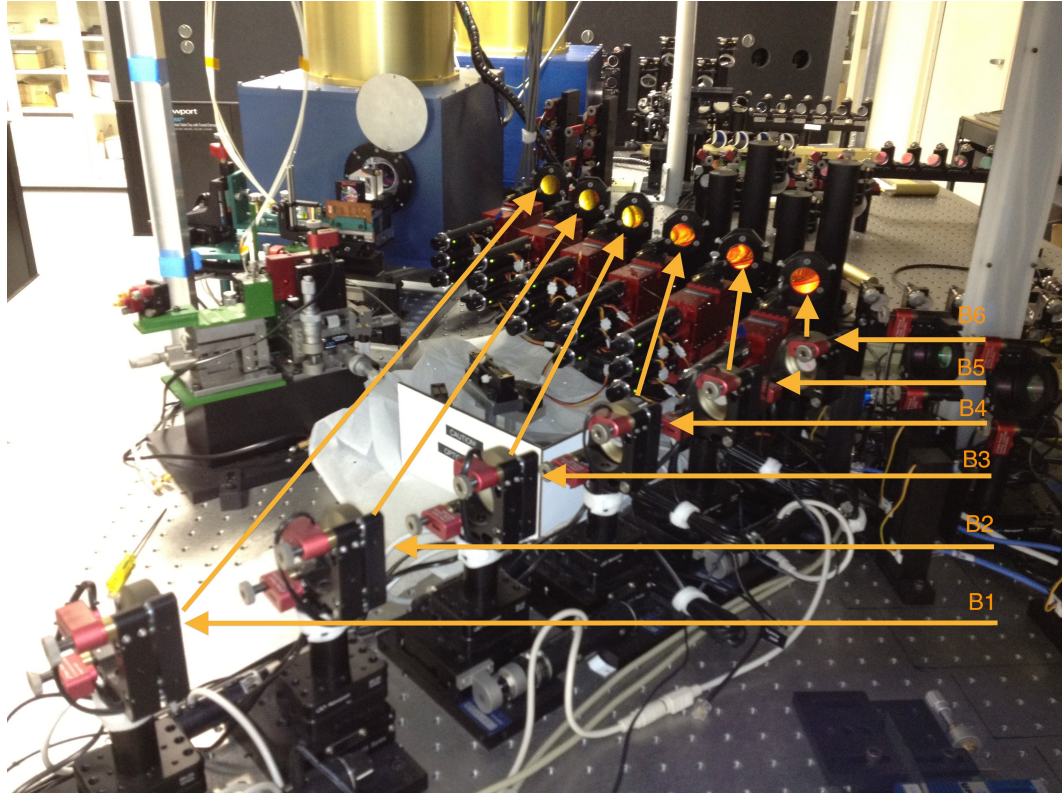
Figure B.1. The yellow lines are the optical paths, light propagates from right to left. The letter "BX" labels the optics for each beam. The figure is reprinted from Che et al. (2012a).
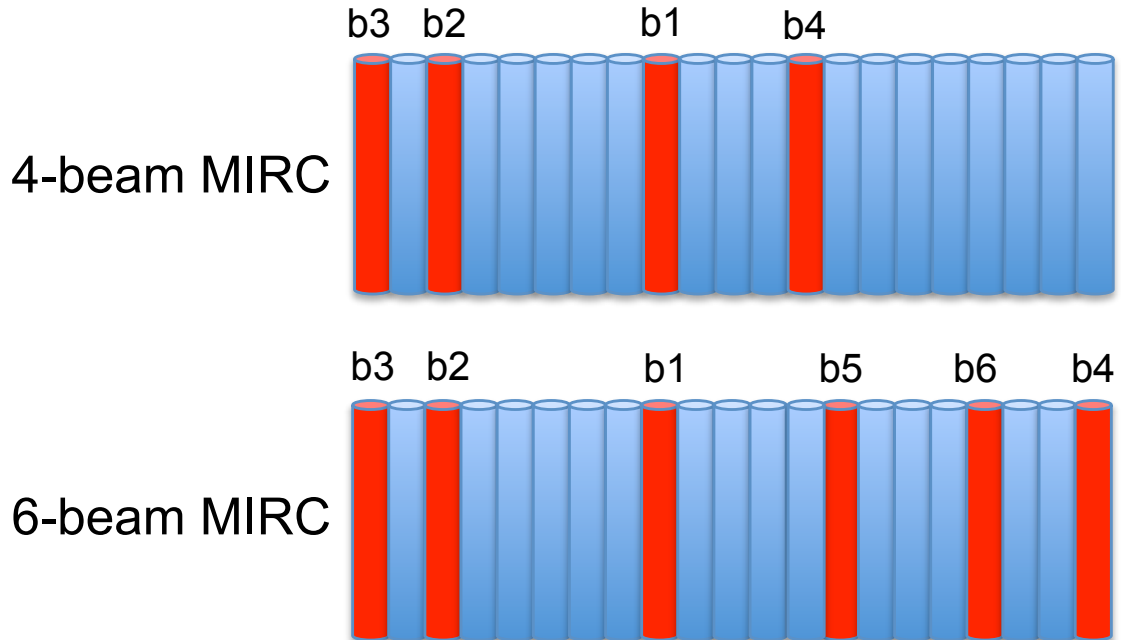

Figure B.2. The same v-groove for 4-beam and 6-beam MIRC. All the fibers have been built in the v-groove since the 4-beam MIRC, we just picked different fibers for the 6-beam MIRC. The figure is reprinted from Che et al. (2012a).
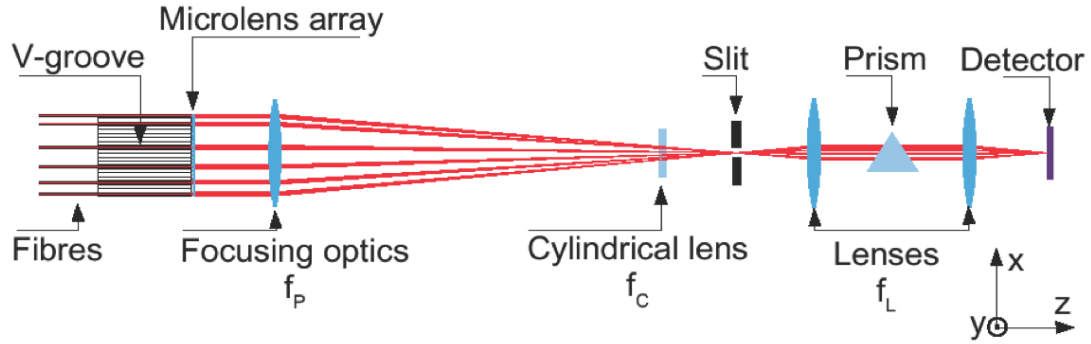
Figure B.3. The schematics of MIRC 6T (Monnier et al., 2008).

defect in the first version is that the alignment stages for the most critical parts were home-made because there were no commercial products that could fit into the limited room for PCs. As a result, the precision of the alignment was limited. And even worse the alignment drifted over time, which required a little adjustment once in a few months.

In the new version of PCs, all the optics are the same as the 1st version. We have improved the stages and mounts that hold the optics for precise alignment, such as adding several more important adjustments including the ones for the beamsplitter. Also the longer focal length of the spherical mirror creates more room for PCs, we use the commercial linear, rotation and tiptilt stages for adjustments which are much more stable than the home-made ones as used in the first version of PCs. The comparison of the new and old PCs are shown in Figure B.4. The back end (within the red oval in Figure B.4) of the two versions of PCs are the same. The only changes are on the front end, represented by the blue oval.

B.3 Results

B.3.1 (u,v) Coverage

One big improvement of the upgraded MIRC is the (u,v) coverage of a single snapshot. Figure B.5 shows a comparison of (u,v) coverage from 3 nights of 4-beam MIRC (left panel) observation and 1 night of 6-beam MIRC (right panel) observation on the same target (ϵAur). The amounts of the (u,v) points are comparable, but the 6-beam MIRC is better in terms of uniformly sampling the (u,v) space.
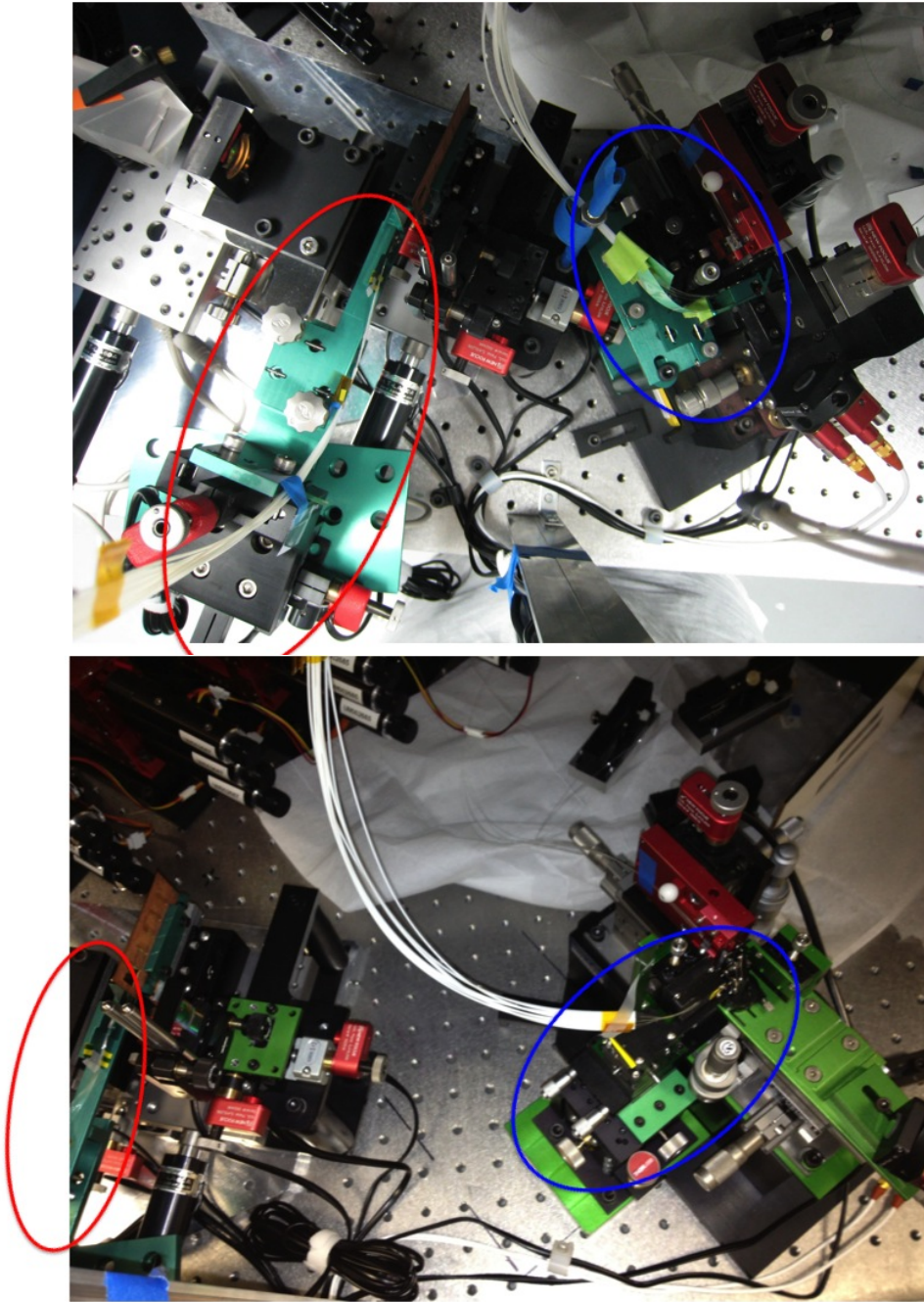
Figure B.4. The comparison of Photometric Channels of 1st (top) and 2nd (bottom) versions. The blue ovals show the front end of the PCs, and the red show the back end. Both panels are reprinted from Che et al. (2012a).
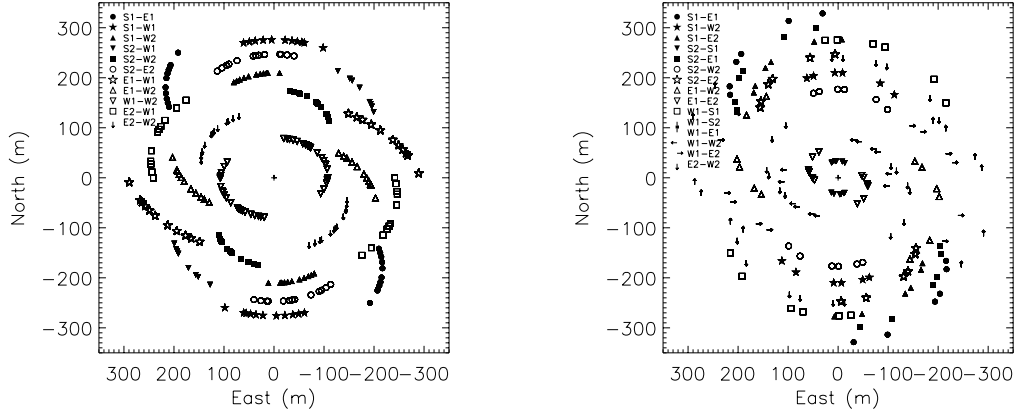
Figure B.5. (u,v) coverage comparison. Left: 3 nights (UT 2009Nov02, 03, 04) of the 4-beam MIRC observation on ϵ Aur Right: 1 night (UT 2011Nov03)of 6-beam MIRC observation on the same target. Both panels are reprinted from Che et al. (2012a).

B.3.2   Flux Ratio of PCs and Fringe light

The new version of the PCs increases the light throughput of the real time fluxes of each telescope. This is critical for interferometric data calibration as we will show below, and also extends MIRC targets to fainter objects because the data calibration is limited by the precision of the flux measurements of each beam for faint objects. We make a comparison of the flux ratios of fringe light over PCs of 7 And with 1st version and ζ And with 2nd version just after they were installed. Table B.3.2 shows the new version of PCs is able to increase the flux by a factor of 2 and more. However due to various reasons that are discussed in Appendix A, this ratio is still quite far from the theoretical limit 3:1 as the beamsplitter reflects 25% of the fringe light into PCs.

	Beam 1	Beam 2	Beam 3	Beam 4	Beam 5	Beam 6
1st version of PCs	13.3	15.6	17.9	18.5	N/A	N/A
2nd version of PCs	7.0	8.3	7.8	7.1	7.7	7.6

Table B.1. Flux ratio fringe/PCs

137

B.3.3   Visibility and Closure phase errors

The upgraded MIRC improves the precision of the visibility and closure phase data because of both the higher throughput of PCs and optimized alignment of each MIRC optics. To estimate the systematic errors, we did model fitting to two relatively simple objects: calibrators and binaries.

Calibrators are small, single and featureless stars. As a good approximation, calibrators are treated as uniform disks so that the visibilities follow Bessel function and the closure phases are zero. HD 210702 is a calibrator with size estimated to be 0.73 ± 0.05 mas from JMMC Bonneau et al. (2006). It is observed by the upgraded MIRC for one data set on UT 2011Jul14, calibrated by o Dra (0.70 ± 0.04 mas Bonneau et al., 2006) and γ Peg (0.41 ± 0.03 mas Barnes et al., 1978). The data is shown in Figure B.6, overplotted with a uniform disk model with the best size estimation to be 0.79 mas. The root mean square of the visibility difference between the data and the model is 0.024. The mean and median of the visibility error percentage are 2.7% and 1.9%, which is lower than 3.4% from the 1st version. The mean and median of the residual closure phases are 1.0 and 0.6 degree.

Binaries are more realistic cases to estimate closure phase errors because they are non-zero. We use a binary model with two uniform disks to fit the well known binary ι Peg that was observed on UT 2011Jul11 with the upgraded MIRC. The data was calibrated by υ Peg (0.99±0.02 mas) and γ Peg (0.41 ± 0.03 mas). The error bars on the model parameters are obtained by bootstrapping the data based on the different wavelength channels in H band. Table B.2 shows the best fitted results, which agree well with Konacki et al. (2010). The model data is overplotted on the observed data in the top panels of Figure B.7, the residuals are shown in the bottom panels.

	distance (mas)	position angle (degree)	flux ratio of the two stars [1]	D_p (mas)	D_s (mas)
This work	7.908± 0.005	171.39 ± 0.06	4.53±0.11	1.018±0.005	0.627±0.024
Konacki et al. (2010)	8.06±0.21	171.56±0.36	5.0±0.5	1.06	0.6

1:the bandwidth smearing effects have not been taken into account here

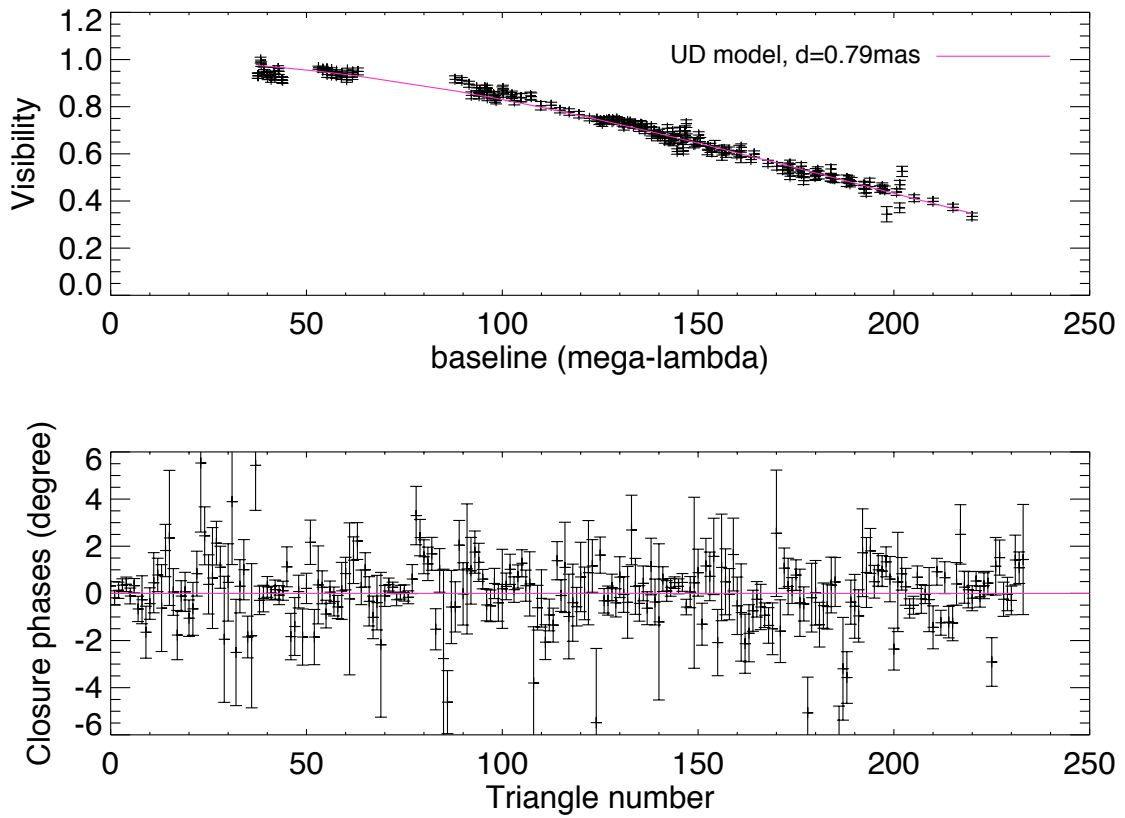**Table B.2.** ι Peg model parameters at MJD = 55753.377

Figure B.6. Observed visibility and closure phases of the calibrator HD 210702 on UT 2011Jul14, overplotted with a uniform disk model represented by purple solid line. The figures are reprinted from Che et al. (2012a).
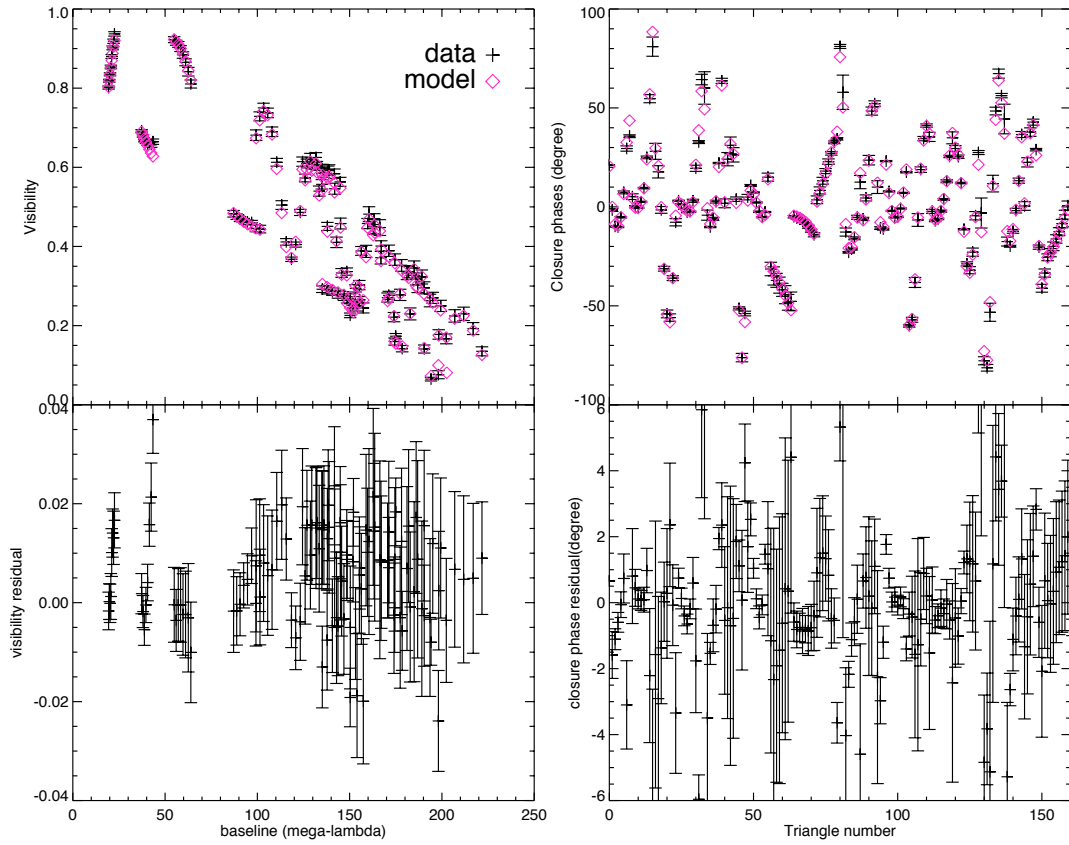
Figure B.7. ι Peg visibility and closure phases observed by the new MIRC on UT 2011Jul11, overplotted with the best fitted binary model (purple diamond). The figures are reprinted from Che et al. (2012a).

As closure phases are sensitive to asymmetries of intensity distribution, the increased precision in the upgraded MIRC really helps to discover weak asymmetries. For instance, 37 And was used as a good calibrator for 4-beam MIRC because it is bright and small. It is observed on UT 2011Jul12 with the 6-beam MIRC, calibrated by υ Peg (0.99±0.02 mas). The new closure phase measurements show that 37 And is a high contrast binary with flux ratio of 66:1 in H band as shown in Table B.3. For such high contrast binary, the visibility data is no longer able to reveal the binary nature because it is overwhelmed by the systematic errors as shown in Figure B.8. However the small oscillations in closure phases (Figure B.9) clearly indicate the existence of a companion. The oscillations are perfectly fitted when we add a faint secondary to the system, proving the oscillations are not systematic errors but real signals from the secondary.

distance (mas)	position angle (degree)	flux ratio of the two stars	D_p (mas)	D_s (mas)
9.110 ± 0.041	230.76 ± 0.22	66 ± 5	0.696 ± 0.011	0.01^2

2:the stellar size is not smaller than 0.01mas

Table B.3. 37 And model parameters at MJD = 55754.499

B.4   Imaging

The 6-beam MIRC has demonstrated powerful imaging abilities in various stellar systems. Here we present an examples in imaging the disk in a Be star ϕ Per.

ϕ Per is a known binary consisting of a Be star (primary) and a hot helium star (secondary). The disk around the primary has been confirmed by emission lines (e.g. Quirrenbach et al., 1997). We observed the system with the 6-beam MIRC for four nights in 2011: Sep03, Sep28, Oct18, Oct19. The binary orbit yields precise parameters that are consistent with the relatively crude Radial Velocity (RV) orbit from Gies et al. (1998), as shown in Figure B.10. We also imaged the primary disk and found it was almost edge-on. And the disk seemed to lie in nearly the same orbital plane as the binary.
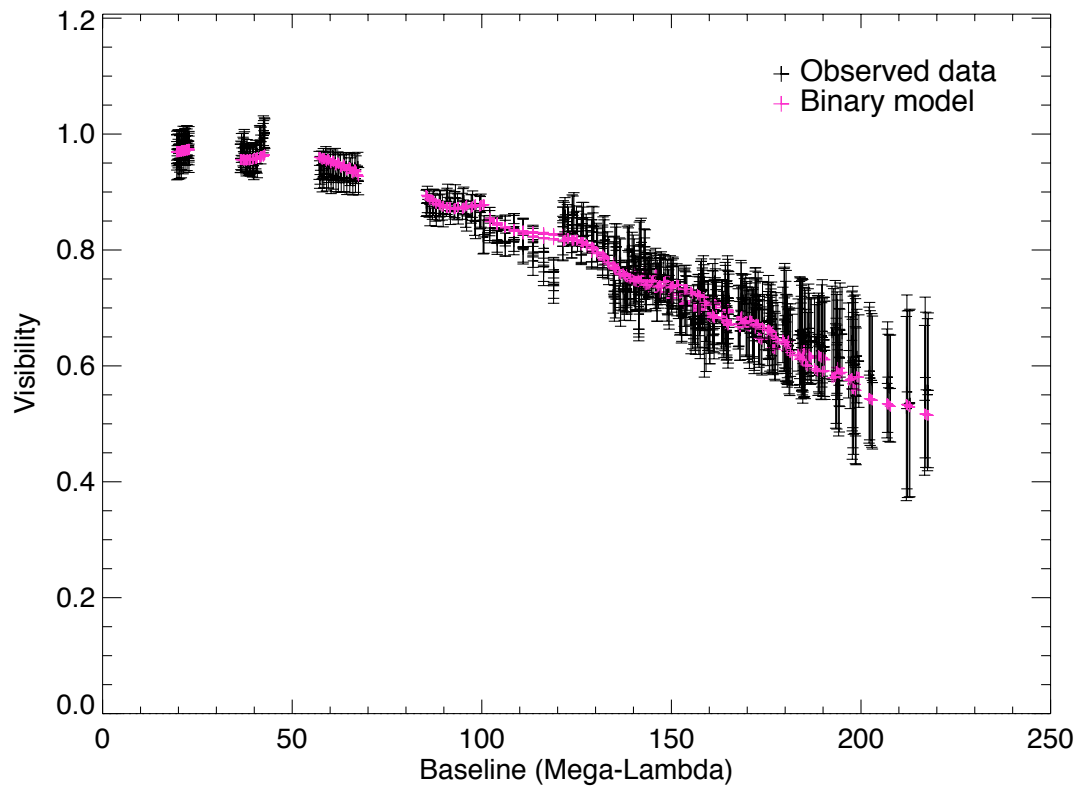
Figure B.8. 37 And visibility observed by the new MIRC on UT 2011Jul12, overplotted with the best fitted binary model (purple). The larger error bars at longer baselines are due to large size of the calibrator υ Peg (0.987±0.020 mas). The figure is reprinted from Che et al. (2012a).
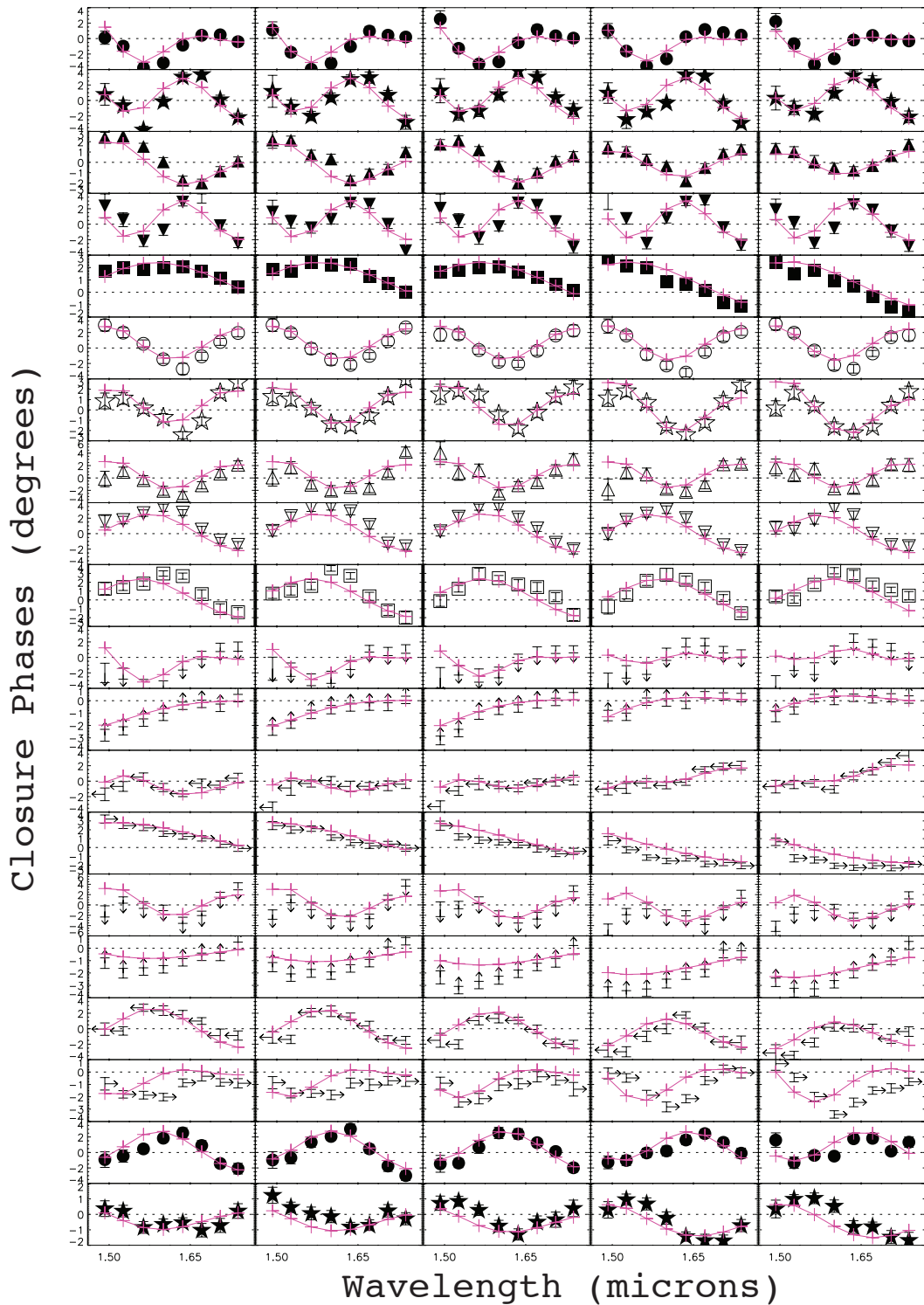
Figure B.9. 37 And closure phases observed by the new MIRC on UT 2011Jul12, overplotted with the best fitted binary model (purple). The figure is reprinted from Che et al. (2012a).
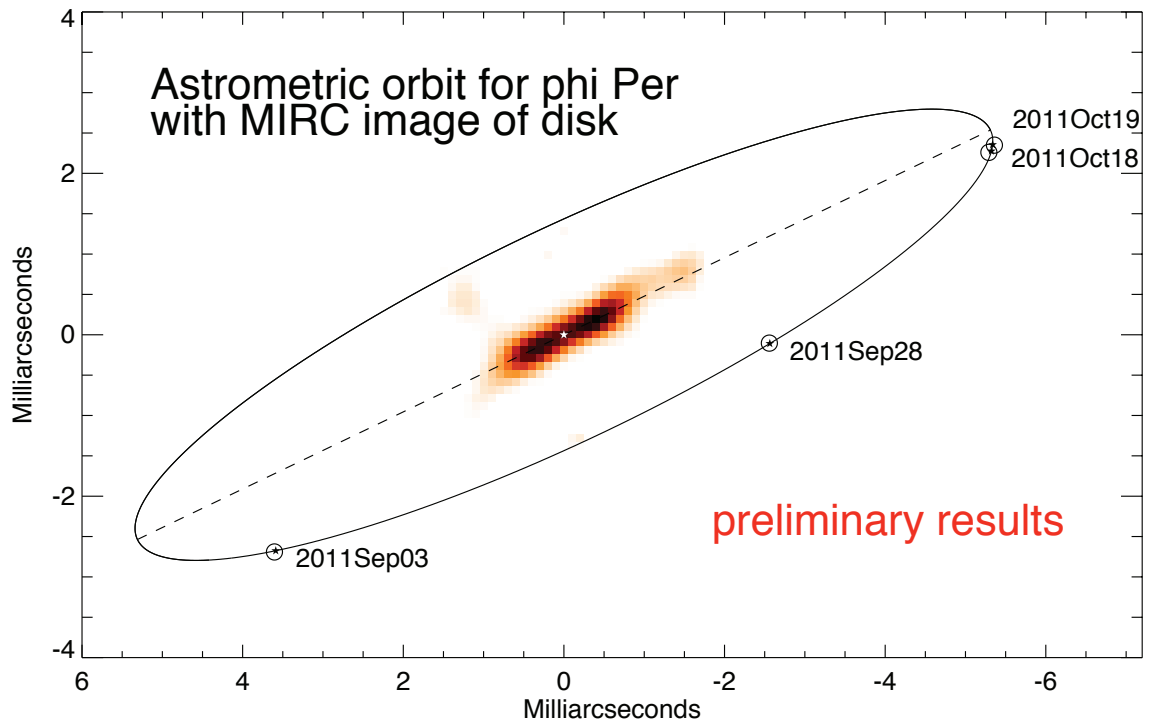
143

Figure B.10. ϕ Per binary orbit and primary disk. The system was observed with the upgraded MIRC on four nights as shown in the figure. The solid ellipse is the binary orbit. The small solid circles are the uncertainties of the secondary positions at each epoch. The black stars in the circles are the best fitted results. The image of the primary disk is reconstructed and presented in the center of the figure. The white star in the center represents where the primary is. The disk imaging is done by MACIM (Ireland et al., 2006). The figure is reprinted from Che et al. (2012a).

BIBLIOGRAPHY

Absil, O., et al. 2013, A&A, 555, A104

Absil, O., Mennesson, B., Le Bouquin, J.-B., Di Folco, E., Kervella, P., & Augereau, J.-C. 2009, ApJ, 704, 150

Abt, H. A., Levato, H., & Grosso, M. 2002, ApJ, 573, 359

Abt, H. A. & Morrell, N. I. 1995, ApJS, 99, 135

Armstrong, J. T., et al. 1998, ApJ, 496, 550

Armstrong, J. T., Nordgren, T. E., Germain, M. E., Hajian, A. R., Hindsley, R. B., Hummel, C. A., Mozurkewich, D., & Thessin, R. N. 2001, AJ, 121, 476

Aufdenberg, J. P., et al. 2006, ApJ, 645, 664

Aumann, H. H., Beichman, C. A., Gillett, F. C., de Jong, T., Houck, J. R., Low, F. J., Neugebauer, G., Walker, R. G., & Wesselius, P. R. 1984, ApJ, 278, L23

Barnes, T. G., Evans, D. S., & Moffett, T. J. 1978, MNRAS, 183, 285

Baron, F., Kloppenborg, B., & Monnier, J. 2012a, in Society of Photo-Optical Instrumentation Engineers (SPIE) Conference Series, Vol. 8445, Society of Photo-Optical Instrumentation Engineers (SPIE) Conference Series

Baron, F., et al. 2014, ApJ, 785, 46

Baron, F., et al. 2012b, ApJ, 752, 20

Baron, F. & Young, J. S. 2008, in Society of Photo-Optical Instrumentation Engineers (SPIE) Conference Series, Vol. 7013, Society of Photo-Optical Instrumentation Engineers (SPIE) Conference Series

Bedding, T. R. 1993, AJ, 106, 768

Bell, K. R. & Lin, D. N. C. 1994, ApJ, 427, 987

Berger, D. H., et al. 2006, ApJ, 644, 475

Bernacca, P. L. & Perinotto, M. 1970, Contributions dell'Osservatorio Astrofisica dell'Universita di Padova in Asiago, 239, 1

Bjorkman, K. S., Miroshnichenko, A. S., McDavid, D., & Pogrosheva, T. M. 2002, ApJ, 573, 812

Boley, P. A., et al. 2013, A&A, 558, A24

Bonneau, D., Clausse, J., Delfosse, X., Mourard, D., Cetre, S., Chelli, A., Cruzalèbes, P., Duvert, G., & Zins, G. 2006, A&A, 456, 789

Boyajian, T. S., et al. 2012, ApJ, 746, 101

Buscher, D. F. 1994, in IAU Symposium, Vol. 158, Very High Angular Resolution Imaging, ed. J. G. Robertson & W. J. Tango, 91

Buscher, D. F., Baldwin, J. E., Warner, P. J., & Haniff, C. A. 1990, MNRAS, 245, 7P

Carciofi, A. C., et al. 2006, ApJ, 652, 1617

Che, X., Monnier, J. D., Kraus, S., Baron, F., Pedretti, E., Thureau, N., & Webster, S. 2012a, in Society of Photo-Optical Instrumentation Engineers (SPIE) Conference Series, Vol. 8445, Society of Photo-Optical Instrumentation Engineers (SPIE) Conference Series

Che, X., et al. 2012b, ApJ, 757, 29

Che, X., Monnier, J. D., & Webster, S. 2010, in Presented at the Society of Photo-Optical Instrumentation Engineers (SPIE) Conference, Vol. 7734, Society of Photo-Optical Instrumentation Engineers (SPIE) Conference Series

Che, X., et al. 2011, ApJ, 732, 68

Che, X., Sturmann, L., Monnier, J. D., Ten Brummelaar, T. A., Sturmann, J., Ridgway, S. T., Ireland, M. J., Turner, N. H., & McAlister, H. A. 2013, Journal of Astronomical Instrumentation, 2, 40007

Chen, L., et al. 2012, A&A, 541, A104

Chesneau, O., et al. 2014, A&A, 563, A71

Chiang, E. I. & Goldreich, P. 1997, ApJ, 490, 368

Chiavassa, A., et al. 2010, A&A, 511, A51

Claret, A. 1998, A&AS, 131, 395

Claret, A. 2000, A&A, 359, 289

Collins, G. W. 1987, in IAU Colloq. 92: Physics of Be Stars, ed. A. Slettebak & T. P. Snow, 3–19

Coudé du Foresto, V., Ridgway, S., & Mariotti, J.-M. 1997, A&AS, 121, 379

Cruzalèbes, P., et al. 2013, MNRAS, 434, 437

Cutri, R. M., et al. 2003, 2MASS All Sky Catalog of point sources., ed. Cutri, R. M., Skrutskie, M. F., van Dyk, S., Beichman, C. A., Carpenter, J. M., Chester, T., Cambresy, L., Evans, T., Fowler, J., Gizis, J., Howard, E., Huchra, J., Jarrett, T., Kopan, E. L., Kirkpatrick, J. D., Light, R. M., Marsh, K. A., McCallon, H., Schneider, S., Stiening, R., Sykes, M., Weinberg, M., Wheaton, W. A., Wheelock, S., & Zacarias, N.

Danziger, I. J. & Faber, S. M. 1972, A&A, 18, 428

Daszyńska, J. & Cugier, H. 2003, Advances in Space Research, 31, 381

Davis, J., Jacob, A. P., Robertson, J. G., Ireland, M. J., North, J. R., Tango, W. J., & Tuthill, P. G. 2009, MNRAS, 394, 1620

Defrère, D., et al. 2011, A&A, 534, A5

Demarque, P., Woo, J., Kim, Y., & Yi, S. K. 2004, ApJS, 155, 667

Domiciano de Souza, A., Kervella, P., Jankov, S., Abe, L., Vakili, F., di Folco, E., & Paresce, F. 2003, A&A, 407, L47

Ducati, J. R. 2002, VizieR Online Data Catalog, 2237, 0

Dullemond, C. P., Dominik, C., & Natta, A. 2001, ApJ, 560, 957

Eggen, O. J. 1967, ARA&A, 5, 105

Eisner, J. A., Chiang, E. I., Lane, B. F., & Akeson, R. L. 2007, ApJ, 657, 347

Eisner, J. A., et al. 2010, ApJ, 718, 774

Ekström, S., et al. 2012, A&A, 537, A146

Espinosa Lara, F. & Rieutord, M. 2011, A&A, 533, A43

Fabregat, J., Reig, P., & Otero, S. 2000, IAU Circ., 7461, 1

Fouqué, P., et al. 2007, A&A, 476, 73

Frémat, Y., Zorec, J., Hubert, A.-M., & Floquet, M. 2005, A&A, 440, 305

Gandet, T. L., Otero, S., Fraser, B., & West, J. D. 2002, Information Bulletin on Variable Stars, 5352, 1

Gies, D. R., Bagnuolo, W. G., Ferrara, E. C., Kaye, A. B., Thaller, M. L., Penny, L. R., & Peters, G. J. 1998, ApJ, 493, 440

Gies, D. R., et al. 2008, ApJ, 682, L117

Glebocki, R. & Gnacinski, P. 2005, VizieR Online Data Catalog, 3244, 0

Glebocki, R. & Stawikowski, A. 2000, Acta Astron., 50, 509

Gray, R. O., Corbally, C. J., Garrison, R. F., McFadden, M. T., & Robinson, P. E. 2003, AJ, 126, 2048

Gray, R. O., Graham, P. W., & Hoyt, S. R. 2001, AJ, 121, 2159

Gull, S. F. & Skilling, J. 1984, in Indirect Imaging. Measurement and Processing for Indirect Imaging, ed. J. A. Roberts, 267

Halonen, R. J., Jones, C. E., Sigut, T. A. A., Zavala, R. T., Tycner, C., Levine, S. E., Luginbuhl, C. B., Vlieg, N., & Vrba, F. J. 2008, PASP, 120, 498

Harmanec, P., Bisikalo, D. V., Boyarchuk, A. A., & Kuznetsov, O. A. 2002, A&A, 396, 937

Hartkopf, W. I., McAlister, H. A., & Mason, B. D. 2001, AJ, 122, 3480

Hartmann, L., Kenyon, S. J., & Calvet, N. 1993, ApJ, 407, 219

Haubois, X., et al. 2009, A&A, 508, 923

Hillenbrand, L. A., Strom, S. E., Vrba, F. J., & Keene, J. 1992, ApJ, 397, 613

Hinz, P. M., Hoffmann, W. F., & Hora, J. L. 2001, ApJ, 561, L131

Högbom, J. A. 1974, A&AS, 15, 417

Holmberg, J., Nordström, B., & Andersen, J. 2007, A&A, 475, 519

Hummel, C. A., Armstrong, J. T., Buscher, D. F., Mozurkewich, D., Quirrenbach, A., & Vivekanand, M. 1995, AJ, 110, 376

Ireland, M. J., Monnier, J. D., & Thureau, N. 2006, in Presented at the Society of Photo-Optical Instrumentation Engineers (SPIE) Conference, Vol. 6268, Society of Photo-Optical Instrumentation Engineers (SPIE) Conference Series

Jennison, R. C. 1958, MNRAS, 118, 276

Johnson, H. L. & Morgan, W. W. 1953, ApJ, 117, 313

Kenyon, S. J. & Hartmann, L. 1987, ApJ, 323, 714

Kenyon, S. J. & Hartmann, L. 1995, ApJS, 101, 117

Kervella, P., Bersier, D., Mourard, D., Nardetto, N., & Coudé du Foresto, V. 2004a, A&A, 423, 327

Kervella, P., Coudé du Foresto, V., Perrin, G., Schöller, M., Traub, W. A., & Lacasse, M. G. 2001, A&A, 367, 876

Kervella, P. & Fouqué, P. 2008, A&A, 491, 855

Kervella, P., Nardetto, N., Bersier, D., Mourard, D., & Coudé du Foresto, V. 2004b, A&A, 416, 941

Kervella, P., Thévenin, F., Di Folco, E., & Ségransan, D. 2004c, A&A, 426, 297

Kharchenko, N. V., Piskunov, A. E., Röser, S., Schilbach, E., Scholz, R., & Zinnecker, H. 2009, A&A, 504, 681

Kitamura, M. & Nakamura, Y. 1988, Ap&SS, 145, 117

Konacki, M., Muterspaugh, M. W., Kulkarni, S. R., & Hełminiak, K. G. 2010, ApJ, 719, 1293

Kraus, S., Calvet, N., Hartmann, L., Hofmann, K.-H., Kreplin, A., Monnier, J. D., & Weigelt, G. 2012a, ArXiv e-prints

Kraus, S., et al. 2012b, ApJ, 744, 19

Kurucz, R. L. 1992, in IAU Symposium, Vol. 149, The Stellar Populations of Galaxies, ed. B. Barbuy & A. Renzini, 225–+

Labeyrie, A., Bonneau, D., Stachnik, R. V., & Gezari, D. Y. 1974, ApJ, 194, L147

Lane, B. F., Creech-Eakman, M. J., & Nordgren, T. E. 2002, ApJ, 573, 330

Lane, B. F., Kuchner, M. J., Boden, A. F., Creech-Eakman, M., & Kulkarni, S. R. 2000, Nature, 407, 485

Lawson, P. R., et al. 2006, in Society of Photo-Optical Instrumentation Engineers (SPIE) Conference Series, Vol. 6268, Society of Photo-Optical Instrumentation Engineers (SPIE) Conference Series

Le Bouquin, J.-B., et al. 2011, A&A, 535, A67

Lee, U., Osaki, Y., & Saio, H. 1991, MNRAS, 250, 432

Liu, W. M., Hinz, P. M., Hoffmann, W. F., Brusa, G., Miller, D., & Kenworthy, M. A. 2005, ApJ, 618, L133

Liu, W. M., Hinz, P. M., Meyer, M. R., Mamajek, E. E., Hoffmann, W. F., Brusa, G., Miller, D., & Kenworthy, M. A. 2007, ApJ, 658, 1164

Lohmann, A. W., Weigelt, G., & Wirnitzer, B. 1983, Applied Optics, 22, 4028

Lovekin, C. C., Deupree, R. G., & Short, C. I. 2006, ApJ, 643, 460

Lucy, L. B. 1967, Zeitschrift fur Astrophysik, 65, 89

MacFadyen, A. I. & Woosley, S. E. 1999, ApJ, 524, 262

Martayan, C., Frémat, Y., Hubert, A.-M., Floquet, M., Zorec, J., & Neiner, C. 2006, A&A, 452, 273

Mason, B. D., Hartkopf, W. I., Gies, D. R., Henry, T. J., & Helsel, J. W. 2009, AJ, 137, 3358

Mason, B. D., Hartkopf, W. I., & Hurowitz, H. M. 2013, AJ, 146, 56

McAlister, H. A. 1985, ARA&A, 23, 59

McAlister, H. A., et al. 2005, ApJ, 628, 439

Meilland, A., et al. 2011, A&A, 532, A80

Meilland, A., Millour, F., Kanaan, S., Stee, P., Petrov, R., Hofmann, K.-H., Natta, A., & Perraut, K. 2012, A&A, 538, A110

Meilland, A., Stee, P., Chesneau, O., & Jones, C. 2009, A&A, 505, 687

Meilland, A., et al. 2007, A&A, 464, 59

Mérand, A. 2008, in EAS Publications Series, Vol. 28, EAS Publications Series, ed. S. Wolf, F. Allard, & P. Stee, 53–59

Mérand, A., Aufdenberg, J. P., Kervella, P., Foresto, V. C. d., ten Brummelaar, T. A., McAlister, H. A., Sturmann, L., Sturmann, J., & Turner, N. H. 2007, ApJ, 664, 1093

Mérand, A., et al. 2005, A&A, 438, L9

Meynet, G. & Maeder, A. 2000, A&A, 361, 101

Millan-Gabet, R. 1999, PhD thesis, Harvard-Smithsonian CfA, 60 Garden St. MS 20, Cambridge MA 02138, USA ¡EMAIL¿rmillan@cfa.harvard.edu¡/EMAIL¿

Millan-Gabet, R., et al. 2010, ApJ, 723, 544

Millan-Gabet, R., Schloerb, F. P., & Traub, W. A. 2001, ApJ, 546, 358

Millan-Gabet, R., et al. 2011, ApJ, 734, 67

Miroshnichenko, A. S., et al. 2003, A&A, 408, 305

Miroshnichenko, A. S., Fabregat, J., Bjorkman, K. S., Knauth, D. C., Morrison, N. D., Tarasov, A. E., Reig, P., Negueruela, I., & Blay, P. 2001, A&A, 377, 485

Monnier, J. D., Berger, J., Millan-Gabet, R., & ten Brummelaar, T. A. 2004, in Presented at the Society of Photo-Optical Instrumentation Engineers (SPIE) Conference, Vol. 5491, Society of Photo-Optical Instrumentation Engineers (SPIE) Conference Series, ed. W. A. Traub, 1370–+

Monnier, J. D., et al. 2012, ApJ, 761, L3

Monnier, J. D. & Millan-Gabet, R. 2002, ApJ, 579, 694

Monnier, J. D., et al. 2006, in Presented at the Society of Photo-Optical Instrumentation Engineers (SPIE) Conference, Vol. 6268, Society of Photo-Optical Instrumentation Engineers (SPIE) Conference Series

Monnier, J. D., Tuthill, P. G., Ireland, M., Cohen, R., Tannirkulam, A., & Perrin, M. D. 2009, ApJ, 700, 491

Monnier, J. D., et al. 2007, Science, 317, 342

Monnier, J. D., et al. 2008, in Presented at the Society of Photo-Optical Instrumentation Engineers (SPIE) Conference, Vol. 7013, Society of Photo-Optical Instrumentation Engineers (SPIE) Conference Series

Morel, M. & Magnenat, P. 1978, A&AS, 34, 477

Mourard, D., Bonneau, D., Koechlin, L., Labeyrie, A., Morand, F., Stee, P., Tallon-Bosc, I., & Vakili, F. 1997, A&A, 317, 789

Mozurkewich, D., et al. 2003, AJ, 126, 2502

Otero, S., Fraser, B., & Lloyd, C. 2001, Information Bulletin on Variable Stars, 5026, 1

Pantazis, G. & Niarchos, P. G. 1998, A&A, 335, 199

Paxton, B. 2004, PASP, 116, 699

Pedretti, E., Monnier, J. D., Brummelaar, T. T., & Thureau, N. D. 2009, New A Rev., 53, 353

Perrin, G., Ridgway, S. T., Coudé du Foresto, V., Mennesson, B., Traub, W. A., & Lacasse, M. G. 2004, A&A, 418, 675

Peterson, D. M., et al. 2006, Nature, 440, 896

Porter, J. M. & Rivinius, T. 2003, PASP, 115, 1153

Quirrenbach, A., Bjorkman, K. S., Bjorkman, J. E., Hummel, C. A., Buscher, D. F., Armstrong, J. T., Mozurkewich, D., Elias, N. M., & Babler, B. L. 1997, ApJ, 479, 477

Rachford, B. L. & Foight, D. R. 2009, ApJ, 698, 786

Ragland, S., et al. 2012, ApJ, 746, 126

Ragland, S., et al. 2006, ApJ, 652, 650

Reiners, A. 2006, A&A, 446, 267

Rhee, J. H., Song, I., Zuckerman, B., & McElwain, M. 2007, ApJ, 660, 1556

Richardson, N. D., Gies, D. R., Morrison, N. D., Schaefer, G., ten Brummelaar, T., Monnier, J. D., & Parks, J. R. 2012, in Astronomical Society of the Pacific Conference Series, Vol. 465, Proceedings of a Scientific Meeting in Honor of Anthony F. J. Moffat, ed. L. Drissen, C. Rubert, N. St-Louis, & A. F. J. Moffat, 160

Richichi, A. & Percheron, I. 2002, A&A, 386, 492

Ridgway, S. T., McAlister, H. A., ten Brummelaar, T., Merand, A., Sturmann, J., Sturmann, L., & Turner, N. 2008, in Society of Photo-Optical Instrumentation Engineers (SPIE) Conference Series, Vol. 7013, Society of Photo-Optical Instrumentation Engineers (SPIE) Conference Series

Roddier, C. & Roddier, F. 1983, ApJ, 270, L23

Rousselet-Perraut, K., et al. 2010, A&A, 516, L1

Sackmann, I. J. 1970, A&A, 8, 76

Sasselov, D. & Karovska, M. 1994, ApJ, 432, 367

Schaefer, G. H., et al. 2010, AJ, 140, 1838

Schröder, C., Reiners, A., & Schmitt, J. H. M. M. 2009, A&A, 493, 1099

Schwarzschild, M. 1975, ApJ, 195, 137

Slettebak, A. 1963, AJ, 68, 292

Stee, P., de Araujo, F. X., Vakili, F., Mourard, D., Arnold, L., Bonneau, D., Morand, F., & Tallon-Bosc, I. 1995, A&A, 300, 219

Stee, P., Vakili, F., Bonneau, D., & Mourard, D. 1998, A&A, 332, 268

Stock, N. D., Su, K. Y. L., Liu, W., Hinz, P. M., Rieke, G. H., Marengo, M., Stapelfeldt, K. R., Hines, D. C., & Trilling, D. E. 2010, ApJ, 724, 1238

Stoeckley, T. R., Carroll, R. W., & Miller, R. D. 1984, MNRAS, 208, 459

Tango, W. J., Davis, J., Jacob, A. P., Mendez, A., North, J. R., O'Byrne, J. W., Seneta, E. B., & Tuthill, P. G. 2009, MNRAS, 396, 842

Tassoul, J. 2000, Stellar Rotation, ed. Tassoul, J.-L.

Telting, J. H., Waters, L. B. F. M., Persi, P., & Dunlop, S. R. 1993, A&A, 270, 355

ten Brummelaar, T. A., et al. 2008, in Society of Photo-Optical Instrumentation Engineers (SPIE) Conference Series, Vol. 7013, Society of Photo-Optical Instrumentation Engineers (SPIE) Conference Series

ten Brummelaar, T. A., et al. 2005, ApJ, 628, 453

ten Brummelaar, T. A., et al. 2012, in Society of Photo-Optical Instrumentation Engineers (SPIE) Conference Series, Vol. 8447, Society of Photo-Optical Instrumentation Engineers (SPIE) Conference Series

Thébault, P. & Beust, H. 2001, A&A, 376, 621

Thiébaut, E. 2008, in Society of Photo-Optical Instrumentation Engineers (SPIE) Conference Series, Vol. 7013, Society of Photo-Optical Instrumentation Engineers (SPIE) Conference Series

Thompson, A. R., Moran, J. M., & Swenson, G. W. 2001, Interferometry and Synthesis in Radio Astronomy, 2nd Edition

Touhami, Y., et al. 2013, ApJ, 768, 128

Townsend, R. H. D., Owocki, S. P., & Howarth, I. D. 2004, MNRAS, 350, 189

Trilling, D. E., et al. 2008, ApJ, 674, 1086

Tuthill, P. G., Haniff, C. A., & Baldwin, J. E. 1997, MNRAS, 285, 529

Tuthill, P. G., Haniff, C. A., & Baldwin, J. E. 1999, MNRAS, 306, 353

Tycner, C., Ames, A., Zavala, R. T., Hummel, C. A., Benson, J. A., & Hutter, D. J. 2011, ApJ, 729, L5

Tycner, C., Hajian, A. R., Mozurkewich, D., Armstrong, J. T., Benson, J. A., Gilbreath, G. C., Hutter, D. J., Pauls, T. A., & Lester, J. B. 2003, AJ, 125, 3378

Vakili, F., et al. 1998, A&A, 335, 261

van Belle, G. T., et al. 2006, ApJ, 637, 494

van Belle, G. T., Ciardi, D. R., Thompson, R. R., Akeson, R. L., & Lada, E. A. 2001, ApJ, 559, 1155

van Belle, G. T. & von Braun, K. 2009, ApJ, 694, 1085

van Leeuwen, F. 2007, A&A, 474, 653

von Zeipel, H. 1924a, MNRAS, 84, 665

von Zeipel, H. 1924b, MNRAS, 84, 684

Waters, L. B. F. M. & Waelkens, C. 1998, ARA&A, 36, 233

Weigelt, G., et al. 2011, A&A, 527, A103

Weigelt, G. P. 1977, Optics Communications, 21, 55

White, T. R., et al. 2013, MNRAS, 433, 1262

Yi, S., Demarque, P., Kim, Y., Lee, Y., Ree, C. H., Lejeune, T., & Barnes, S. 2001, ApJS, 136, 417

Yi, S. K., Kim, Y., & Demarque, P. 2003, ApJS, 144, 259

Young, J. S., et al. 2000, MNRAS, 315, 635

Zhao, M., et al. 2008, ApJ, 684, L95

Zhao, M., et al. 2009, ApJ, 701, 209